

NORTHWESTERN UNIVERSITY

Modelling of Slow-moving Landslide Dynamics Driven by Precipitation: from Stable Creep to  
Catastrophic Runaway Failure

A DISSERTATION

SUBMITTED TO THE GRADUATE SCHOOL  
IN PARTIAL FULFILLMENT OF THE REQUIREMENTS

for the degree

DOCTOR OF PHILOSOPHY

Field of Civil and Environmental Engineering

By

Xiang Li

EVANSTON, ILLINOIS

August 2022

© Copyright by {Xiang Li, 2022}

All Rights Reserved

## ABSTRACT

Slow-moving landslides are common in mountainous area worldwide. Most of them mobilizes slowly over long periods of time, which causes continuous damage to proximal infrastructure and habitats. Most notably, some slow-moving landslides can experience catastrophic acceleration at some point in their life cycle, with potentially fatal consequences. It is therefore important to interpret the dynamics of such class of landslides. Although, there are several factors that can lead to downslope sliding and velocity change, this thesis focuses on the dynamics of slow-moving landslides driven by precipitation. Upon rainfall infiltration, pore-water pressure transients tend to develop within the landslide body, a mechanism often explained through linear and/or nonlinear diffusion models. Consequently, the normal effective stress, which governs the deformation and resistance against downslope movement, will change. On such basis, this thesis proposes to tackle the dynamics of slow-moving landslides from a physics-based standpoint, by placing emphasis on the role of the inelastic deformation behavior of the materials within the basal shear zone of a landslide, as well as on its role in modulating the corresponding coupled hydrological-mechanical processes responsible for the motion of landslides.

Viscoplastic models, which can take rate-dependent strength of earthen material into account, have been widely used to quantify the slow-moving landslide's sliding behaviors. Yet, typically used viscoplastic model assume a lack of pre-failure viscosity, an assumption that contradicts laboratory tests on soil specimens, as well as field measurements based on remote sensing. Starting from this insight, this thesis proposes a new hybrid rheological law aimed at predicting viscous behavior

prior to frictional failure, while ensuring accurate computation of the post-failure sliding dynamics. The hydro-mechanical model resulting from the proposed viscoplastic rheology is eventually assessed on the basis of data from several study sites, showing that the model can be used to describe distinct types of landslide motion spanning from episodic to quasi-continuous sliding.

In addition to time-dependent soil behavior, this thesis has also addressed the link between the landslide dynamics and the volume change of the shear zone material. For this purpose, a fully coupled simulation framework accounting for inelastic deformation and simultaneous excess pore pressure transients within the shear zone has been formulated. Although the proposed approach is applicable to very general constitutive models, its capabilities have been tested with reference to the standard perfectly plastic Mohr Coulomb model, which has been used to interpret landslide dynamics in case of both dilative and contractive frictional shear zone response. Numerical simulations of creeping landslides have been used to validate the ability of proposed methodology to capture movements induced by precipitation. In all the inspected scenarios, a satisfactory match between data and simulations was possible for positive dilation coefficients, which led to spontaneous generation of negative excess pore pressure and self-regulated post-triggering velocity. Conversely, simulations based on vanishing dilation (hence, reflecting the approach of critical state) were shown to produce sharp acceleration and large runout, typical of catastrophic events. These results encouraged further analyses aimed at incorporating more sophisticated constitutive laws able to recover critical state as a function of the rate and magnitude of the landslide movements.

The final stages of this thesis therefore focused on the analysis of transitions from slow-moving landslides to runaway failures. This objective was pursued by linking the newly formulated hydro-mechanical framework with a classic critical state plasticity model (i.e., Modified Cam Clay).

Simulation on model slopes were therefore used to show that the proposed methodology captures runaway acceleration even without abrupt changes of the hydrologic forcing. By analyzing the failure mechanisms, an index reflective of the potential for runaway failure was proposed, which can be used to track the stability of a slow-moving landslide. Notably, the examination of how a slope is weakening upon rainfall based on the magnitude and duration of its creep movement is conducted. The model is finally used to explain the dynamics of landslide movements in a number of study sites. The results show that the proposed framework can be used to disclose whether a moving landslide possesses the signature of a weakening shear zone material and is thus likely to develop runaway failure upon rainfall cycles. It is shown that the proposed index can successfully differentiate stable, episodic landslide events from gradually weakening downslope movements that are gradually converging towards a runaway failure solely on the basis of high-quality parameter calibration of measurements collected during the stable creeping stage.

## ACKNOWLEDGEMENTS

I want to first thank my advisor Dr. Giuseppe Buscarnera, for being an excellent mentor and inspiring me to embrace the fascinating world of Geomechanics. Under his supervising, I gradually grasped the insight of ideal research and the manner to address scientific issues. I am very grateful to all his support in both academia and life. I would also like to thank Dr. Alexander Handwerker, Dr. James Hambleton, and Dr. Daniel Horton for serving my thesis committee. The valuable comments and knowledge they shared throughout the courses, qualifier, prospectus, journal paper editing, and dissertation defense are extremely supportive. I am also grateful to Dr. Richard Finno, who taught great advanced soil mechanics course and introducing me Geomechanics from practical viewpoint.

I would like to thank the amazing people from our research group: Jose Lizarraga, Yida Zhang, Yanni Chen, Dawa Seo, Ritaja Ray, Zhichen Song, Ming Yang, and Benigno Alonzo. It is a great pleasure to work with this group of talented people and sharing the research excitements. In addition, thank my other colleagues: Zhefei Jin, Anastasia Nally, Qinghao Yang, Hyunjin Lee, Yize Pan, Jibril Coulibaly and Andony Landivar. Working with all these awesome people in the same office is an unforgettable experience.

Lastly, I would like to thank my family and friends. Thank my parents Xining Li and Hong Xiang for their love and support. Thank my girlfriend Yuting Zhang for all of her love, help and encouragement. I could not imagine how I can accomplish these works without her support and accompany.

## TABLE OF CONTENTS

ABSTRACT.....	3
ACKNOWLEDGEMENTS.....	6
TABLE OF CONTENTS.....	7
LIST OF FIGURES .....	12
LIST OF TABLES .....	23
1 PHENOMENOLOGY OF SLOW-MOVING LANDSLIDES .....	24
1.1 Global impacts of landslide.....	24
1.2 Slow-moving landslides across the world.....	26
1.2.1 California Coast Ranges .....	27
1.2.2 Selected examples of landslide sites .....	29
1.2.3 Other slow-moving landslides around the world.....	33
1.3 Summary .....	36
2 SLOW-MOVING LANDSLIDES SIMULATION USING VISCOPLASTIC MODEL ....	39
2.1 Rainfall infiltration analyses .....	40
2.2 Material time-dependent properties and viscoplastic models.....	43
2.3 On-site indication of pre-yield viscosity.....	48
2.4 Model testing .....	51
2.4.1 Response under monotonically increased pore-water pressure .....	51

2.4.2 Sensitivity tests for hybrid model mechanical parameters .....	52
2.5 Case study simulation .....	53
2.5.1 Minor Creek landslide.....	54
2.5.2 Hydrological simulation of Boulder Creek and Mud Creek landslide .....	57
2.5.3 Boulder Creek landslide movement.....	58
2.6 Discussion.....	62
2.7 Summary .....	64
3 DYNAMICS OF SLOW-MOVING LANDSLIDE CONTROLLED BY INELASTIC HYDRO-MECHANICAL COUPLINGS.....	66
3.1 Slow-moving landslide hydro-mechanical couplings.....	67
3.2 Coupled flow-deformation framework .....	68
3.2.1 Pore-water pressure diffusion within the sliding block .....	70
3.2.2 Coupled flow-deformation within the shear zone.....	72
3.2.3 Constitutive models .....	74
3.2.4 Nondimensionalization .....	76
3.3 Model performance.....	77
3.3.1 Precipitation induced diffusion and elastic response .....	77
3.3.2 Behaviors under plastic regime.....	79
3.3.3 Coupling effects .....	82
3.4 Case studies.....	84

	9
3.4.1 Parameter optimization method .....	84
3.4.2 Two Towers landslide.....	85
3.4.3 Minor Creek landslide.....	86
3.4.4 Mud Creek landslide .....	88
3.5 Discussion .....	90
3.6 Summary .....	92
<b>4 SIMULATION OF CATASTROPHIC LANDSLIDE DYNAMICS BASED ON CRITICAL STATE PLASTICITY .....</b>	<b>94</b>
4.1 Landslide catastrophic failures .....	96
4.2 Coupled framework incorporating critical state plasticity .....	98
4.2.1 Limitations of landslide dynamics simulations based on perfect plasticity.....	98
4.2.2 Coupled analyses based on the Modified Cam Clay plasticity model.....	102
4.3 Simulation of catastrophic failure.....	106
4.3.1 Failure mechanism.....	106
4.3.2 Self-regulating index.....	107
4.3.3 Simulation of the evolving landslide dynamics in response to successive rainfall cycles .....	109
4.3.4 Comparison with landslide movement measurement .....	111
4.4 Case studies.....	116
4.4.1 Two Towers landslide.....	116

	10
4.4.2 Mud Creek landslide .....	117
4.5 Summary .....	119
5. CONCLUSIONS AND FUTURE WORK .....	121
5.1 Summary .....	121
5.2 Discussion and recommendations for future research .....	123
APPENDIX. REGIONAL-SCALE SIMULATION OF FLOWSLIDE TRIGGERING IN STRATIFIED DEPOSITS .....	127
A.1 Flowslide triggered in stratified deposits .....	128
A.2 Model implementation .....	129
A.2.1 Hydraulic model.....	129
A.2.2 Mechanical model.....	130
A.2.3 Vectorized Finite Element Framework.....	131
A.3 Case study .....	132
A.3.1 Selected sites .....	132
A.3.2 Mechanical parameters .....	134
A.3.3 Hydraulic parameters .....	134
A.4 Assessment of model performance .....	135
A.4.1 Categorization of failure mechanisms.....	135
A.4.2 Spatial performance .....	139
A.4.3 Temporal performance .....	140

	11
A.4.4 Failure depth .....	142
A.5 Model application in other sites .....	143
A.6 Discussion .....	146
A.7 Summary .....	149
References .....	151

## LIST OF FIGURES

- Figure 1.1 Number of non-seismically triggered global fatal landslide events from 2004~2016 (Frounde and Petley, 2018)..... 24
- Figure 1.2 California Coast area and Franciscan Complex lithologic unit 1 draped over a hillshade of topography. Case study landslides in this work are labeled and plotted. .... 28
- Figure 1.3 Slow-moving landslides located at Eel River catchment, Northern California, and their downslope velocity with the precipitation rate. a) Location of the landslides, their names are abbreviated as: Db1 = Dobbyn Creek 1, Db2 = Dobbyn Creek 2, Lf = Lauffer Road, Kw1 = Kekawaka Creek 1, Kw2 = Kekawaka Creek 2, kw3 = Kekawaka Creek 3, Cc = Chamise Creek, Bc = Boulder Creek, Lr = Lundblade Ranch, Sy = Simmerly Road. b) Downslope velocity time history and the local precipitation rate (Handwerger et al., 2013). ..... 29
- Figure 1.4 Map of Minor Creek landslide and ground-based monitors. a) view of the landslide, b) monitored pore pressure at sliding surface, downslope displacement, and cumulative rainfall for Minor Creek landslide (Iverson & Major, 1987)..... 30
- Figure 1.5 Map and ground-based monitors of Two Towers landslide. a) simplified map and location of the Two Towers landslide, b) monitored displacement, cumulative rainfall and landslide displacement (Schulz, et al., 2018)..... 31
- Figure 1.6 Remote sensing velocity and cumulative rainfall monitored from rain gages for Mud Creek and Boulder Creek landslide. a) monitored velocity for Mud Creek and Boulder Creek landslide, b) rainfall data from nearest rainfall station, c & d) monitored displacement for Boulder Creek and Mud Creek (Handwerger et al., 2019). ..... 32

Figure 1.7 The map and monitors of Vallcebre landslide. a) map of the landslide, b) monitored ground water level depth and landslide velocity (Ferrari et al., 2011). .....	33
Figure 1.8 The map of Brattas landslide with the cumulative rainfall and observed displacement. a) landslide map, b) observed displacement (Oberender and Puzrin, 2016) .....	34
Figure 1.9 The map and monitored displacement of Tessina landslide. a) morphodynamic zonation of the Tessina landslide, b) air-photo of the detaching and upper accumulation zone with the benchmarks identified, c) displacement time history for four representative monitoring points (Petley et al., 2004). .....	35
Figure 1.10 Photo of Vajont landslide. ....	36
Figure 2.1 Schematic of infinite slope model used for simulations in this chapter. ....	40
Figure 2.2 Schematic representation of model discretization for an infiltration problem. a) Mesh structure and problem domain, b) Initial hydrostatic profile, c) boundary conditions (Li et al., 2019). ....	41
Figure 2.3 Model simulation of water pressure profile under precipitation for 5 and 30 hours (analytical resolution from Wu et al., 2016, simulation parameters reported in Song et al., 2020). ....	42
Figure 2.4 Schematic of soil creep test. a) Stress-strain relationship; b & c) stress and strain temporal evolvement.....	44
Figure 2.5 laboratory tests indicate soil time-dependent behavior under elastic regime. a) loading history of the triaxial drained test, b) axial strain corresponding to several loading process, which is marked by its stress level (from di Prisco and Imposimato). ....	46
Figure 2.6 Factorized viscous shear strain rate (by $1/\mu$ , parameter that scales the magnitude) versus yield function value for different expressions of viscous nucleus. a) Dashed-dotted	

blue, dashed red, and black lines show model predictions for the exponential, hybrid, and Bingham-like models with  $a = 1$ . b) Blue, dashed red, and black lines show model predictions with  $a = 1$  for the hybrid and Bingham-like and  $a = 0.23$  for the exponential law. These simulations show that changing the power-law rheology term can lead to the same strain rate at the maximum yield function. .... 48

Figure 2.7 Pre- and post-yield motion analyses of the Boulder Creek landslide, northern California.

Right top image is the average downslope InSAR velocity map of the Boulder Creek landslide plotted on top of a hillshade. Main plot shows the ratio of shear stress divided by the effective normal stress vs. average velocity. The data are binned by pixels with the same slope angle. Horizontal red line shows the stress ratio corresponding to  $13^\circ$  friction angle, which is the minimum friction angle reported by Keefer and Johnson, 1978. InSAR data are from Handwerger et al. (2019) and DEM is from TanDEM-X. TanDEM-X data used is under copyright by the DLR. .... 49

Figure 2.8 Pre- and post-yield motion analyses of the Mud Creek landslide, central California.

Right top image is the average downslope InSAR velocity map of the Mud Creek landslide zone plotted on top of a hillshade (USGS 3DEP). California State Highway 1 (CA1) is shown. The main plot shows the ratio of shear stress divided by the effective normal stress vs. average InSAR velocity. The data are binned by pixels with same slope angle. Horizontal red line corresponds to a stress ratio corresponding to  $13^\circ$  friction angle, which is the minimum friction angle reported by Keefer and Johnson, 1978. .... 50

Figure 2.9 Comparisons of the three viscoplastic models. Shear strain is computed from rheological laws in response of monotonic increased and cyclic pore-water pressure. a)

Factorized viscoplastic shear strain calculated by each rheological law. b) Pore-water

pressure monotonic variation and corresponding effective normal stress. c). Factorized viscoplastic shear strain calculated by different value of  $\alpha$ . d) Cyclic pore water pressure variation, corresponding effective normal stress change. For this synthetic landslide experiments the model parameters were chosen to resemble those reported for typical landslide settings in the California Coast Ranges (Schultz et al., 2018), thus setting  $h = 6$  m,  $\theta = 15^\circ$ ,  $\gamma_{sat} = 22$  kN/m<sup>3</sup>,  $\phi = 21^\circ$ . ..... 52

Figure 2.10 Pore-water pressure, rainfall, and displacement of Minor Creek landslide during 1982 ~1985. a) Monitored and simulated pore-water pressure variation at the sliding surface and the precipitation rate; b) monitored and simulated landslide movement and cumulative rainfall, model parameters shown in Table 2. Monitored data are digitized from Iverson and Major (1987). ..... 55

Figure 2.11 Calibration of Boulder Creek and Mud Creek hydraulic parameters. a) Simulation of Minor Creek compared with 40 m depth. b) Simulation of Minor Creek with 20 m depth. .... 57

Figure 2.12 Pore-water pressure change, rainfall, and displacement of Boulder Creek landslide during 2015 ~2017. a). Pore-water pressure variation at sliding surface and the precipitation rate; b). monitored and simulated landslide movement time history in addition with the cumulative rainfall, model parameters shown in Table 2. .... 59

Figure 2.13 Pore-water pressure change, rainfall, and displacement of Mud Creek landslide during 2014 ~2017. a) Simulated pore pressure variation at sliding surface and the precipitation rate. b) Simulated landslide movement time history and measured cumulative rainfall. The left boundary of the shaded rectangle represents the occurrence of catastrophic acceleration.

Our model is not able to capture runaway instability and predicts a return to slow motion (black line inside gray shaded region). ..... 61

Figure 3.1 Schematic of slow-moving landslide slope profile and precipitation induced stress change. a) slope components, b) material stress path induced by rainfall infiltration..... 69

Figure 3.2 Schematic of infinite slope model used for coupled hydro-mechanical analyses. The governing equations for each diffusion process inside the landslide material and the basal shear zone are also illustrated. .... 70

Figure 3.3 Simulation of pore-water pressure transients caused by precipitation. a) Simulated pore-water pressure change at top of shear zone caused by a constant rainfall. b) Computational results of bottom shear zone pore-water pressure change, corresponding to different value of ***Tlce***; c & d) schematics of pore-water pressure distribution with higher and lower ***Tlce***, where higher ***Tlce*** results from shear zone permeability (***kb***)  $5.5 \times 10^{-7}$  m/s, and lower ***Tlce*** indicate ***kb*** =  $5.5 \times 10^{-12}$  m/s. Stiffness parameters are taken as: oedometric modulus ***Eoed*** = 5 MPa, and shear modulus ***G*** = 2 MPa. .... 78

Figure 3.4 Schematics of hydrological response generated by plastic normal strain. a) Stress change caused by hydrological forcing in plastic regime with nil normal plastic deformation. b) Dilative material generated self-regulating behavior. c) Contractive material induced self-feeding mechanisms. .... 80

Figure 3.5 Simulation of the hydro-mechanical response of an infinite slope subjected to imposed pore-water pressure change at the top of its shear zone. a) top shear zone pore-water pressure changes in one year, with the bottom response under both elastic and plastic regime. b) Downslope displacement, c & d) pore-water pressure profile when material is under elastic & plastic regime. e & f) Schematic of hydrological response in elastic and

plastic regime. Synthetic slope tested here is assumed to be 7 m deep, inclination  $15^\circ$ , dilation angle  $\psi = 2^\circ$ . ..... 81

Figure 3.6 Slope hydro-mechanical response corresponding to different dilative potential. a) pore-water pressure at the top and bottom of shear zone. b) Simulated displacement with different dilation angle, c) simulated velocity vs. displacement, d) the relationship of sliding velocity and dilation angle, with the condition for liquefaction. .... 82

Figure 3.7 Inverse analyses obtained OBJ values corresponding to friction angle and permeability when  $\psi=2^\circ$ , optimized parameter is indicated by the red polygon. .... 85

Figure 3.8 Simulation of Two Towers landslide and relevant monitoring. a) Monitored pore-water pressure change at top of shear zone, optimized pore-water pressure distribution at the bottom of shear zone, and cumulative rainfall, b) computational displacement from optimization compared to the monitored value. .... 86

Figure 3.9 Simulated and monitored hydrological and mechanical behaviors at the Minor Creek landslide site. a) monitored and simulated pore-water pressure at top of the shear zone, simulated pore-water pressure at the base of the shear zone, and cumulative rainfall. b) Monitored and simulated displacement. .... 87

Figure 3.10 Simulated and monitored hydrological and mechanical behaviors at the Mud Creek landslide site. a) Simulated pore-water pressure distribution at top and bottom of the shear zone and cumulative rainfall. b) Monitored and simulated displacement by the end of stable sliding. The left boundary of the shaded rectangle represents the occurrence of catastrophic failure. .... 89

Figure 4.1 Synthetic landslide response of pore-water pressure change applied on top of the shear zone by using the Mohr-Coulomb perfectly plastic model. a) Applied pore-water pressure.

b) Pore-water pressure change within the basal shear zone. c) Induced normal strain. d) Generated landslide displacement; a shaded polygon indicates that the material has achieved a plastic deformation regime. For this synthetic landslide experiments the model parameters were chosen to resemble one of the study sites, Mud Creek landslide (Warrick et al., 2019; Handwerger et al., 2019), thus setting  $h = 20$  m,  $\theta = 32^\circ$ ,  $\gamma_{sat} = 21$  kN/m<sup>3</sup>,  $E_{oed} = 5$  Mpa,  $G = 2$  Mpa,  $\phi = 36.1^\circ$ ,  $\psi = 1^\circ$ , and  $ksb = 1 \times 10^{-8}$  m/s. .... 99

Figure 4.2 Schematic of typical stress strain relations representing soil behavior during shear experiments compared against predictions of a perfect plastic model. a) shear stress vs. shear strain for strain-hardening response (e.g., loose sand under drained loading or normally consolidated clay). b) normal strain vs. shear strain. c) shear stress vs. shear strain for strain-softening response (e.g., dense sand or over-consolidated clay). d) normal strain vs. shear strain. .... 100

Figure 4.3 Schematic of stress, strain response under shearing corresponding to the MCC model. In this schematic the multi-axial stress state is neglected. a) Graphical representation of yield surface and corresponding elastic domain. b) Stress path under strain-controlled shearing and initial yield surface for both soft clay (over-consolidated) and hard clay (normal consolidated). c) relation between shear stress and shear strain. d) relation between shear strain and normal strain. .... 103

Figure 4.4 Synthetic landslide response of pore-water pressure change applied on top of the shear zone by using Modified Cam Clay model. a) Stress path upon applied hydrological forcing in elastic and plastic domain sequentially. b) Basal shear zone hydrological response in pore-water pressure change. c) induced normal strain. d) Landslide displacement, the inset shows the zoomed in displacement at the initiation of runaway failure. Shaded polygon

- indicate material enter plastic regime; the yellow polygon marks the entering of critical state. Total time is 20 days, for this synthetic landslide experiments the model parameters were the same as illustrated by Figure 4.1 caption, except  $B_p = 30$  and  $m = 0.7$ , (this  $m$  value leads to the similar yield stress ratio. .... 105
- Figure 4.5 Schematic of stress path, yield surface evolution, and deformation response due to hydrological forcing. a-c) variation of stress status and yield surface triggered by wetting signal displayed in Fig 4.1a at different stages (A, B, and C). d) Normal strain change, e) basal pore-water pressure, f) landslide displacement. .... 107
- Figure 4.6 Formulation of self-regulating index. a) schematic of rainfall infiltration induced hydrological forcing in elastic domain and corresponding  $\eta p$ . b) The yield surface and  $\eta p$  evolvement under wetting. c) Tracking of self-regulating index during the simulation illustrated in Fig. 4.5. .... 108
- Figure 4.7 Simulated landslide response after five sequential synthetic rainfall events. a) rainfall events applied at the landslide surface and induced pore-water pressure at the top of the shear zone. b) Basal shear zone pore-water pressure changes for each material deformation scenario (S indicates stable, W indicates weak, M indicates medium). c) Computed self-regulating index, d) generated displacement. Each water cycle's total duration is 30 days, for this synthetic landslide experiments the model parameters were chosen to resemble the Two Towers landslide study site (Schulz et al., 2018), thus setting  $h = 7$  m,  $\theta = 15^\circ$ ,  $\gamma_{sat} = 21$  kN/m<sup>3</sup>,  $m = 0.34$ ,  $k_{ss} = 5 \times 10^{-8}$  m/s, and The hardening parameter  $B_p$  for material S, M, and W equals to 1E6, 14, and 7 respectively. .... 110
- Figure 4.8 Ground-based monitored water level and displacement of the Minor Creek landslide from 1982 to 1985. shaded bands indicate the periods during which the water level was

above a triggering threshold, thus inducing landslide mobilization (Figure from Iverson and Major, 1987)..... 112

Figure 4.9 Landslide response to three wetting pulse that with same magnitude but different shape of pore-water pressure distribution. a) Applied pore-water pressure changes on top of shear zone. b) Basal pore-water pressure changes. c) Self-regulating index evolvment under wetting. d) Wetting induced slope displacement. Shaded polygon indicates material under plastic domain. Each water cycle is 30 days long. The previous synthetic landslide (Fig. 4.7) is tested here with material W and S. .... 113

Figure 4.10 Velocity of the Mud Creek landslide and Paul Slide and corresponding cumulative precipitation data from 2015 to 2017. a) InSAR observed velocity change (data after Handwerger et al., 2019). b) cumulative precipitation recorded from a weather station located 20 km and 50 km from Mud Creek and Paul Slide. Dash-dot line represents the obvious acceleration of each case at each year, dash line A is a reference line showing that the acceleration of Paul slide corresponding to the cumulative rainfall. .... 114

Figure 4.11 Landslide response to five consecutive wetting pulses induced by monotonically increased constant rainfall. a) Applied rainfall condition on the top of ground surface and induced pore-water pressure changes on top of shear zone. b) Basal pore-water pressure changes. c) Self-regulating index changes under wetting. d) Wetting induced slope displacement. The shaded band indicates the time lag between two plastic stage activations. Each water cycle is 30 days long. The previous synthetic landslide (Fig. 4.7) is tested here with material M and S..... 115

Figure 4.12 Simulated displacement and computed self-regulating index for Two Towers landslide. a) Monitored cumulative rainfall and basal pore-water pressure. b) Simulated and

monitored displacement. c) simulated self-regulating index in addition to the failure scenario, $A=1$ . Data after Schulz et al., 2018.....	117
Figure 4.13 Simulated pore-water pressure, displacement and self-regulating index of Mud Creek landslide. a) monitored cumulative rainfall and simulated basal pore-water pressure. b) Simulated and monitored displacement. c) simulated self-regulating index in addition to the failure scenario, $A=1$ . The displacement data is obtained by Handwerter et al., 2019 through InSAR analysis.....	118
Figure A.1 Schematic representation of model workflow. $m$ = number of cells, $j$ = number of cell classes with the same FE mesh, $t_f$ = failure time, $z_f$ = failure depth, $s$ = suction, $FS_s$ = factor of safety of slips failure; $FS_w$ = factor of safety of flowslides.....	132
Figure A.2 Stratigraphic conditions for multiple sites across a portion of the Pizzo d'Alvano massif affected by shallow landslides and failure source area (based on Crosta & Dal Negro, 2003; Cascini & Sorbino, 2003). .....	133
Figure A.3 Calibration of hydraulic parameters. a) water retention curve (data after Crosta & Dal Negro 2003), b) hydraulic conductivity function (data after Pirone et al. 2015).....	135
Figure A.4 Landslide transportation and deposition zones (Crosta and Dal Negro 2003). .....	136
Figure A.5 Reported and computed relative frequency of slope failure mechanisms. ....	138
Figure A.6 Spatial distribution of simulated failure mechanisms through layered and homogeneous models. a) Model based on layered slopes, b) Model based on homogeneous slopes. ..	138
Figure A.7 Predicted landslide triggering mechanisms in the Sarno site (source areas reported by Frattini et al, 2004).....	140

Figure A.8 Sarno landslide failure time. a) Reported from Cascini et al. 2011, b) calculated in this work .....	141
Figure A.9 Computed failure time history. a) Obtained from stratified model, b) from homogeneous model .....	142
Figure A.10 Computed and site-investigated failure depth. a) reported by Crosta & Dal Negro 2003, b) calculated from the stratified model, c) calculated from the homogenous model.....	143
Figure A.11 Results of model spatial performance for four selected municipalities across the Pizzo d'Alvano massif .....	144
Figure A.12 Predicted failure triggering mechanisms at different sites. a) Lavorate, b) Siano, c) Quindici, d) Bracigliano.....	145
Figure A.13 Bracigliano failure distribution calculated by Siano stratification profile. ....	147
Figure A.14 Source area and landscape slope angle distribution for each site. a) five studied municipalities, b) Sarno, c) Quindici, d) Siano, e) Bracigliano, f) Lavorate. ....	148

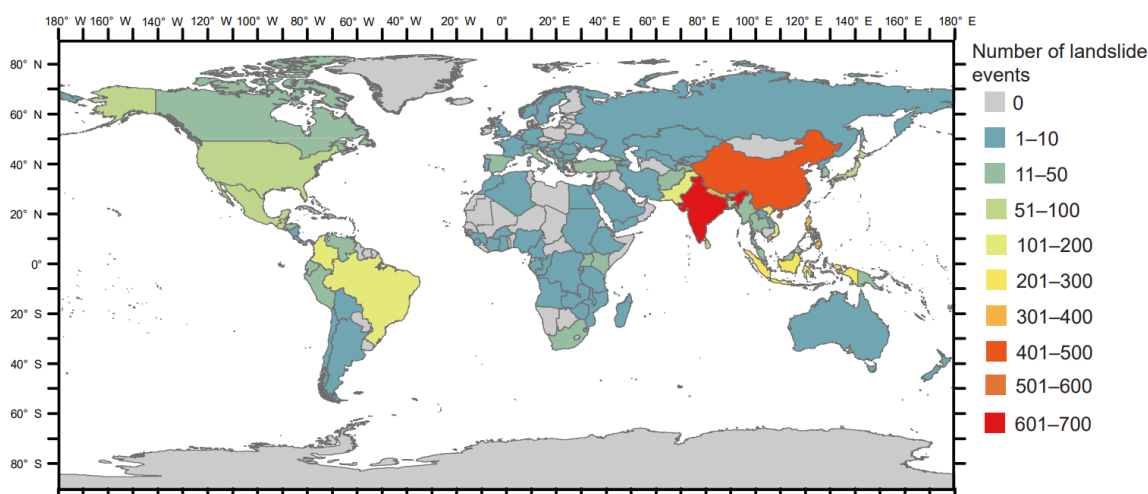
## LIST OF TABLES

Table 2.1 parameters calibration guidance .....	54
Table 2.2 model parameters for case studies .....	61
Table 4.1 Parameters for each case study .....	118
Table A.1 Description of mechanical parameters and calibrated values.....	134
Table A.2 Comparison of performance metrics from models with homogeneous and layered slopes. The simulations based on homogeneous slopes assume constant saturated permeability throughout the domain, with value equal to that Ash A. For the stratified model, the Table indicates only the value of saturated permeability, $k_s$ , of Ash A. The value of $k_s$ for the other layers is defined in accordance with the hydraulic parameter calibration illustrated in Fig A3. ....	139

## 1 PHENOMENOLOGY OF SLOW-MOVING LANDSLIDES

### 1.1 Global impacts of landslide

The global impact of landslides is immense. According to the World Health Organization (WHO), landslides influenced around 4.8 million people and led to more than 18000 fatalities from 1998 to 2017. In the United States alone, ground failures lead to over \$ 1B financial losses each year. Notably, as shown in Fig. 1.1, non-seismically triggered fatal landslide events are widely spread worldwide, from 2004 to 2016 (Frounde and Petley, 2018). Still the actual social and financial impacts from landslides are likely to be underestimated, in that it is sometimes difficult to isolate their consequences from those of the other natural hazards involved in the mobilization of ground failures (e.g., floods, earthquakes, and tsunamis (Petley, 2012)).



**Figure 1.1** Number of non-seismically triggered global fatal landslide events from 2004~2016 (Frounde and Petley, 2018).

To mitigate the damaging consequences from landslides, it is of great significance to understand the mechanisms that govern their occurrence and evolution and identify suitable remedies, such as early warning systems or technical interventions (Dai et al., 2002). There are several factors that

can trigger landslide hazards such as precipitation, earthquakes (Rodriguez, et al, 1999), hurricanes (Bucknam et al., 2001), volcanic eruptions (Hurlimann et al., 2000), and snow-melting (Cardinali et al., 2000). In addition, landslide hazards encompass different time scales (Hung, 2007), from sudden failures occurring within few minutes to continuous creeping movements that can last for years or even decades (Cascini et al., 2010; Handwerger et al., 2015).

The focus of this research is on the mechanics underlying the manifestation of creeping landslides, i.e., slowly moving volumes of soil and rock enabled by weak zones within natural hillslopes. Creeping landslides are widely observed in mountainous area worldwide (Keefer & Johnson, 1983; Baum & Reid, 1995; Oberender & Puzrin, 2016; Lacroix, et al., 2020). Some of them can remain active for decades or centuries (Mackey et al, 2009) with a velocity within 1 m/year and experience rate changing when local hydraulic condition varied (Iverson & Major, 1987; Handwerger et al., 2013; Bennett et al., 2016; Hilley et al., 2004). They can influence both social and economic activities, thus cause great damage to structures and infrastructure networks (Nappo, et al., 2019). Most notably, it is normally observed that catastrophic runaway failure of slope is often anticipated by much slower creep movements (Voight, 1978). It thus indicated that some of the slow-moving landslides can accelerate catastrophically (Petley et al., 2002). These features are essential to address one of the most demanding challenges of landslide forecasting, i.e., the prediction of the catastrophic acceleration of active landslides.

The mobilization of slow-moving landslides is governed by environmental factors as precipitation (Handwerger et al., 2013; Bennett et al., 2016; Hilley et al., 2004; Cascini et al., 2010; Finnegan et al., 2021). Notably, the role of the volumetric deformation on the sliding behavior has been extensively explored through field and laboratory measurements (Schulz, et al., 2018; Agliardi et al, 2020). It thus indicates the significance of coupled effects between rainfall infiltration, earthen

material volume change, and the pore-water pressure transients in remodulating the dynamics of slow-moving landslides.

To address these challenges, new opportunities are arising from advances in remote sensing. Current technology allows for the detection of ground movements at spatiotemporal resolutions that were unthinkable just a decade ago (Aryal et al., 2012). Remote sensing has therefore reached a stage where its further development for hazard forecasting requires a better understanding of the landslide mechanisms. Currently, modeling approaches to address creeping landslide behaviors governed by hydraulic conditions are still limited to simplified idealizations of the interaction between earthen material deformation and flow process. Meanwhile, numerical methods able to evaluate the fate of creeping landslides by accounting for all their underlying hydrologic and deformational processes are not yet established. Advanced Geomechanical models are thus called for which can incorporate the fully coupled flow-deformation behavior of earthen material. Such methodologies provide opportunity to bridge the gap between the rich datasets collected from advanced remote sensing technologies and landslide hazard mitigation and forecasting.

### *1.2 Slow-moving landslides across the world*

The aim of this thesis is to develop physically based models to interpret the velocity change of creeping landslides and predict catastrophic acceleration. To provide a contextual framework, a brief description of several case-studies around the world is provided, thus delineating the general properties of creeping landslides. California as a site where the infrastructure suffered the damage from landslide widely and existed abundant data of landslide movement both from ground measurements and remote sensing, is selected as the case study area. Most of the studied cases in this work located in California Coast Ranges.

### 1.2.1 California Coast Ranges

The California Coast Ranges (Fig. 1.2) are an ideal natural laboratory to analyze landslide behaviors. Landslides are widespread there due to active tectonics, mechanically weak rocks, and high seasonal precipitation. Thousands of landslides have been identified, including slow-moving landslides, rapid debris slides and flows, and landslides that have transitioned from slow motion to catastrophic failure (Keefer & Johnson, 1983; Kelsey et al., 1995; Hapke & Green, 2006; Mackey & Roering, 2011; Handwerger et al., 2015). Many of the landslides occur within the Jurassic-Cretaceous Franciscan Mélange (KJf, Fig. 1.2), an uplifted accretionary prism complex that consists of a clay-rich granular matrix with tectonically sheared siltstone, sandstone, meta-sandstone, shale, serpentinite, and blueschist (Jennings, 1977). In general, the KJf is clay-rich (illite, chlorite, and smectite), with low shear strength (friction angle  $\sim 20^\circ$ ), and low hydraulic diffusivity ( $\sim 10^{-6} \text{ m}^2/\text{s}$ ).

Another key trend of the creeping landslides of this region is their kinematics, which is often reported as closely linked to changes in precipitation, in a form that leads to acceleration during the wet season and deceleration during dry periods (Hilley et al., 2004; Handwerger et al., 2013; Bennet et al., 2016; Finnegan et al., 2021). Movement of ten landslides (Fig 1.3a) have been explored through InSAR analyses (Handwerger et al., 2013) and compared with local precipitation (Fig. 1.3b). It showed that, the downslope velocity of those landslides tended to decrease during May to October each year, when no intense rainfall occurred. However, during the wet season when abundant precipitation took place, their velocity increased. Notably, downslope movement of creeping landslides performed in a delayed form governed by the precipitation; there is a clear time-lag (around 40 days) between the initiation of intense rainfall and landslide acceleration.

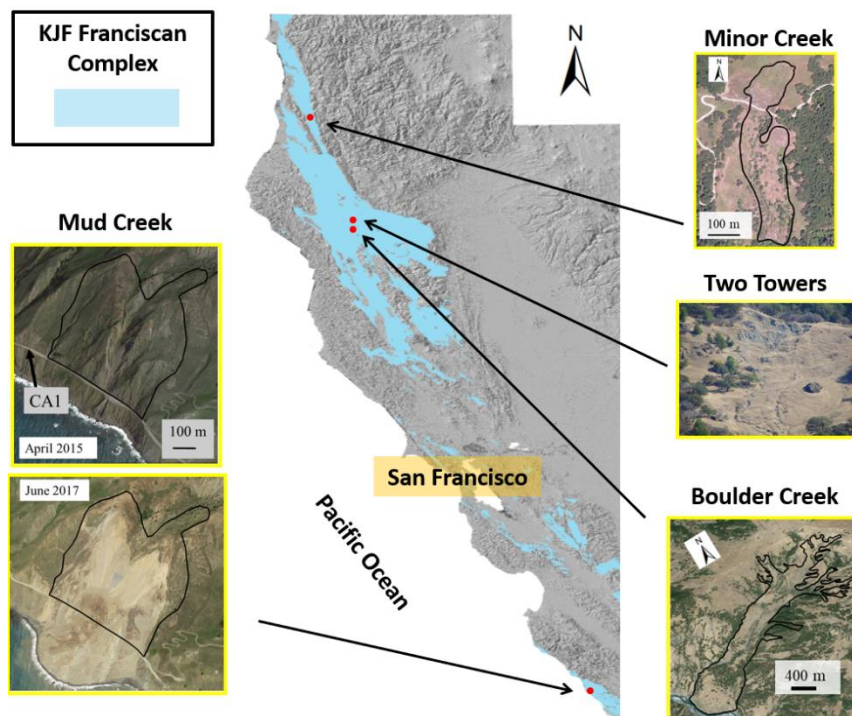


**Figure 1.2 California Coast area and Franciscan Complex lithologic unit 1 draped over a hillshade of topography. Case study landslides in this work are labeled and plotted.**

Moreover, many of the landslides on the California Coast Ranges have moved slowly (within 1 m/year) for decades or even centuries and cause massive amounts of erosion (Hapke & Green, 2006). However, these landslides have the potential to transition to catastrophic failure (Petley et al., 2002; Handwerger et al., 2019).

In this thesis, four landslide sites (Minor Creek, Boulder Creek, Two Towers, and Mud Creek; Fig. 1.2) have been selected as specific examples to develop and test a comprehensive geomechanical framework to explain the temporal dynamics of landslides in this area and predict their future trends. Among them, Mud Creek landslide was observed to fail catastrophically on May 20, 2017 after displaying creep for extended periods of time. The catastrophic acceleration of this landslide to highway CA1, resulting in road closure between May 2017 and July 2018. Details of each case will be discussed in the following subsection.

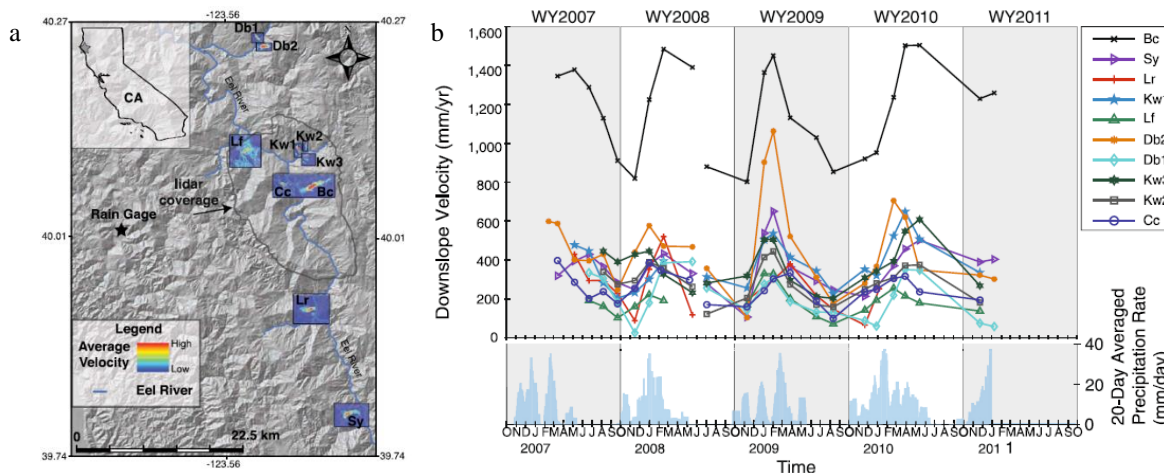


**Figure 1.3** Slow-moving landslides located at Eel River catchment, Northern California, and their downslope velocity with the precipitation rate. a) Location of the landslides, their names are abbreviated as: Db1 = Dobbyn Creek 1. Db2 = Dobbyn Creek 2, Lf = Laufer Road, Kw1 = Kekawaka Creek 1, Kw2 = Kekawaka Creek 2, kw3 = Kekawaka Creek 3, Cc = Chamise Creek, Bc = Boulder Creek, Lr = Lundblade Ranch, Sy = Simmerly Road. b) Downslope velocity time history and the local precipitation rate (Handwerger et al., 2013).

### 1.2.2 Selected examples of landslide sites

Minor Creek landslide (Fig. 1.4a) is a compound, complex, slow-moving landslide, covering about 10 hectares in Redwood Creek drainage basin, northern CA Coast Ranges. Iverson & Major (1987) provided three years of detailed rainfall, ground water and movement data (all ground-based) of this landslide from August 1982 to September 1985 (Fig. 1.4b). The average slope angle is  $15^\circ$ ; the thickness of the landslide along its longitudinal axis is about 6 m (Iverson, 1985).

The precipitation (Fig. 1.4b) was monitored through a rain gage located in site of the landslide. In California Coast Range, more than 80 percent of precipitation took place from October to May; the California water year, is thus defined to study hydraulic factors which starts from October 1 ends on September 30. Fig. 1.4b shows that the pore pressure starts to increase from October and kept as a relatively high value until May, the end of wet season. Then it decreased to around the original value by the end of dry season (September). It indicated that the landslide movement is

governed by hydraulic conditions, in that increasing pore pressure leads to a reduction of the mean effective stress (Terzaghi, 1925) and hence to loss of stability. Fig. 1.4b illustrates that the Minor Creek landslide tends to be active when local monitored pore pressure is higher than a threshold around 26 kPa. Although the maximum pore-water pressure values during observation are similar, 1983~1984 pore pressure preserved at values higher than the mobilized threshold longer than the other years. Thus, displacement triggered in that water year (around 1 m) is much higher than the other two water years.

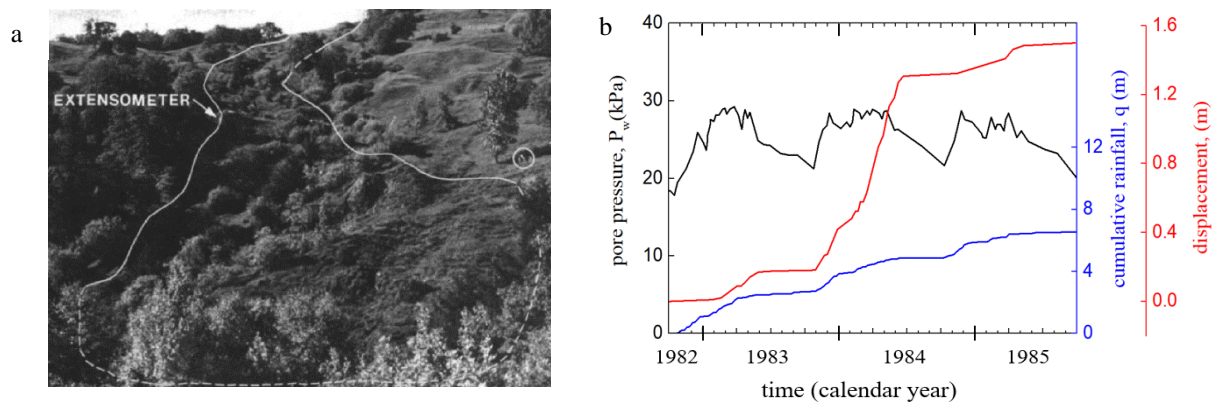


**Figure 1.4** Map of Minor Creek landslide and ground-based monitors. a) view of the landslide, b) monitored pore pressure at sliding surface, downslope displacement, and cumulative rainfall for Minor Creek landslide (Iverson & Major, 1987).

Another case of interests is Two Towers landslide (Fig. 1.5a), which is around 250 m long and averages about 40 m wide and 7 m deep with an average inclination around  $15^\circ$ . The groundwater head and landslide movement have been monitored from November 2014 to July 2017 by Schulz et al (2018). For this case, rainfall was measured using a tipping-bucket gauge. Groundwater head was observed using vibrating-wire piezometers placed within boreholes. Landslide movement was investigated using a biaxial tilt sensor installed with within polyvinyl chloride-cased boreholes. In addition, some other data were also monitored such as: vertical displacement, temperature, etc.

Fig. 1.5b illustrated that the monitored pore pressure distributed seasonally following the rainfall in a form that increase when rainfall occurs frequently and decrease on the contrary. For the Two Towers landslide, swelling of clay soils is believed to have contributed to a delay between the movements and the monitored pore pressure (Schulz et al., 2018). Fig. 1.5b shows that sliding movement occurred more than two months after the pore pressure approaching the peak value.

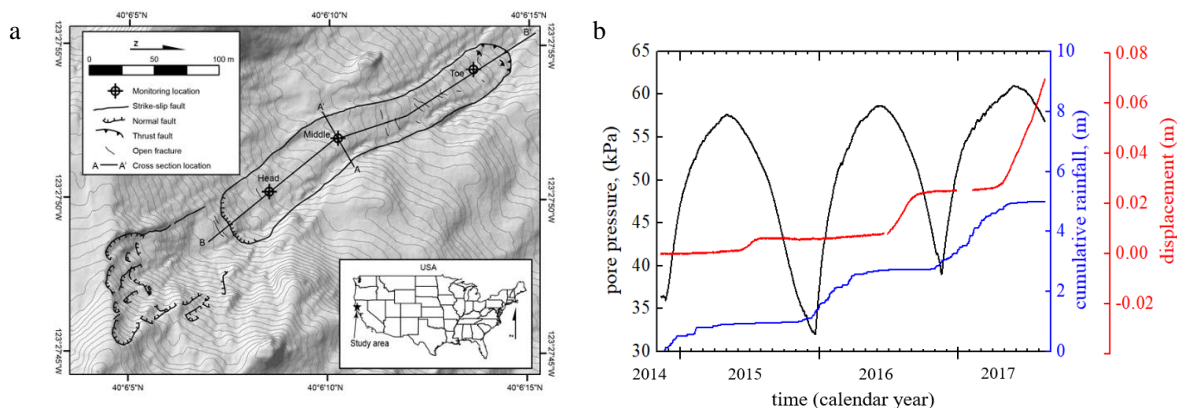


**Figure 1.5** Map and ground-based monitors of Two Towers landslide. a) simplified map and location of the Two Towers landslide, b) monitored displacement, cumulative rainfall and landslide displacement (Schulz, et al., 2018).

Boulder Creek Landslide (Fig. 1.2), northern California Coast Ranges, has displayed stable sliding for decades (Handwerger et al., 2019). The movement of Boulder Creek landslide from January 2016 to October 2017 (Fig. 1.6a) had been provided by Handwerger et al. (2019) through interferometric processing of synthetic aperture radar (InSAR) images acquired by the Copernicus Sentinel-1 A/B satellites. The precipitation data was acquired by NOAA and provided by the California Climate Data Archive.

In addition, movement for Mud Creek landslide between February 28, 2015, and May 12, 2017, had been provided by Handwerger et al., (2019) (Fig. 1.6b) through InSAR images. Mud Creek landslide has performed stable sliding movement for more than 8 years; however suddenly failed

catastrophically on a dry day (May 20, 2017) following a prolonged period of heavy rainfall. This sudden acceleration destroyed California State Highway 1 (CA1), resulting in road closure between May 2017 and July 2018 and cost an estimated \$54 million in road repairs (Caltrans report, 2018).

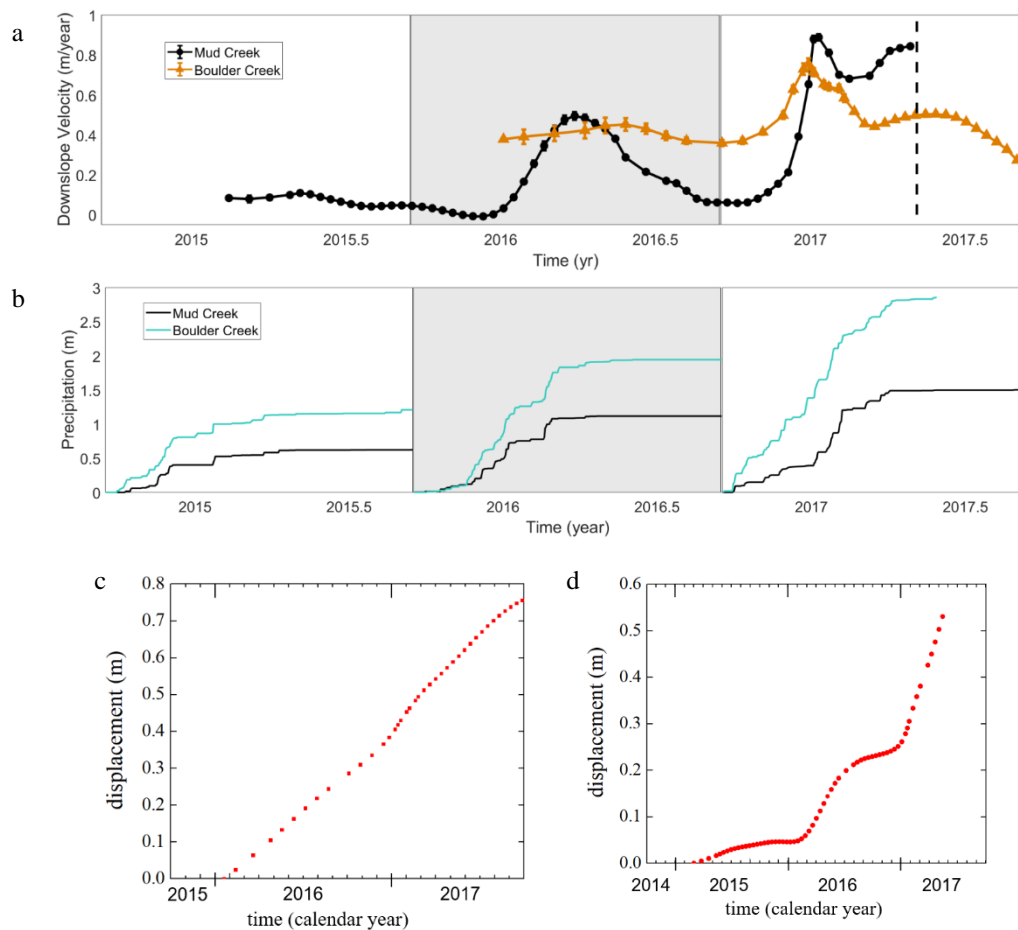


**Figure 1.6 Remote sensing velocity and cumulative rainfall monitored from rain gages for Mud Creek and Boulder Creek landslide. a) monitored velocity for Mud Creek and Boulder Creek landslide, b) rainfall data from nearest rainfall station, c & d) monitored displacement for Boulder Creek and Mud Creek (Handwerger et al., 2019).**

Fig. 1.6a shows that both landslides accelerate during wet seasons. However, their movement displayed distinct trends (Fig. 1.6 c & d). Specifically, the velocity of the Boulder Creek landslide tends to fluctuate in a narrow range, leading to a quasi-linear time series of displacements. As for

Mud Creek, its displacement before the catastrophic failure displayed episodic step-like features, typically following intense rainfall events.

These four landslides are selected as reference cases for this thesis, in that they exemplify different classes of creeping landslide movement, thus offering the opportunity to test the applicability of geomechanical models for creeping landslides. Most notably, the catastrophically acceleration of Mud Creek provide us the opportunity to predict failure through capturing slow-moving landslides pre-failed dynamics.

### 1.2.3 Other slow-moving landslides around the world

As mentioned previously, creeping landslides are widely observed in mountainous areas worldwide. In order to grasp the general behaviors of this type of landslides, some of other well-studied cases will be briefly discussed here.

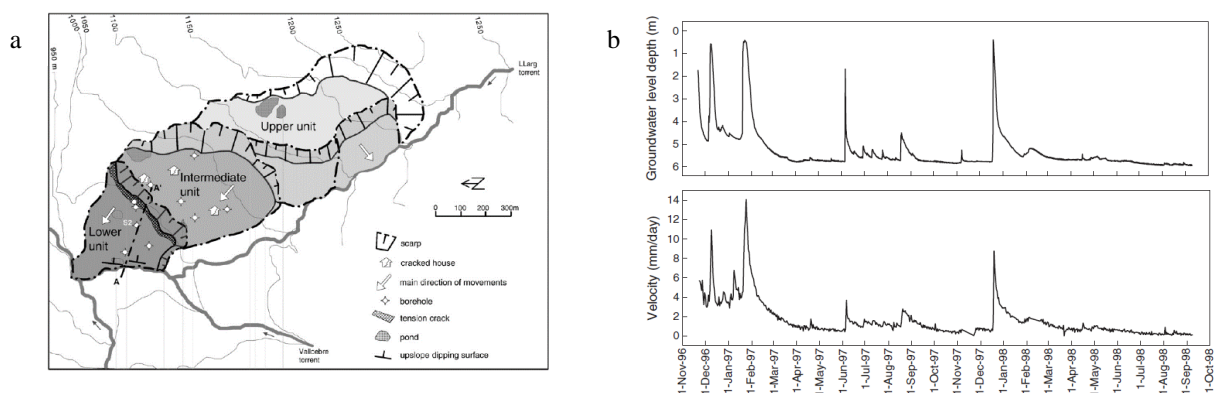


**Figure 1.7** The map and monitors of Vallcebre landslide. a) map of the landslide, b) monitored ground water level depth and landslide velocity (Ferrari et al., 2011).

The Vallcebre landslide located in the upper Llobregat river basin, 140 km north of Barcelona, Spain. The mobilized material consists of a set of shale, gypsum and claystone layers. The dimensions of this creeping landslide are 1200 m long and 600 m wide (Corominas et al., 2005). Three main units of decreasing thickness towards the toe compose the landslide, resulting in a

stair-shape profile (Ferrari et al., 2011). During July 1996, March 1997, and April 1998, sixteen boreholes were drilled in the landslide in order to obtain sample material, test hydraulic response and displacement. Fig. 1.7b indicates that the mobilization of this landslide is consistent with the obvious increase of groundwater level. This landslide has been studied widely to interpret the mechanics govern the velocity change (Corominas et al., 2005; Ferrari et al., 2011; Conte et al., 2014; Cascini et al., 2014). Corresponding research showed the close connection for this case between the rainfall events and landslide activation.

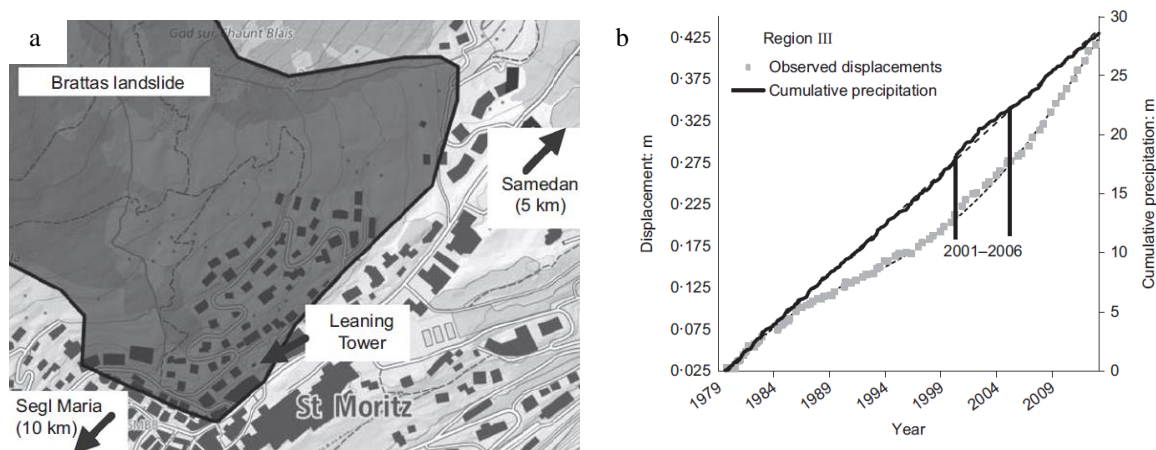


**Figure 1.8** The map of Brattas landslide with the cumulative rainfall and observed displacement. a) landslide map, b) observed displacement (Oberender and Puzrin, 2016)

The Brattas landslide is a slow-moving landslide located in St Moritz, Switzerland. The active ground movement monitored for almost a century has been reported as the primary cause of damages to nearby buildings and infrastructure and is constrained at the bottom by a rock outcrop (Oberender & Puzrin, 2016). The leaning Tower of St Moritz is one of the most striking pieces of evidence of this landslide (Puzrin & Sterba, 2006). The sliding layer is 600-700 m long and 17-23 m thick and consists of silty soil matrix with boulder inclusions. The downslope movement of this landslide has been observed by Puzrin et al (2006; 2011; 2016). Fig. 1.8 b indicated that, during

2001 and 2006, when rainfall was more intense compared with the normal observation, the landslide was accelerating discernably.

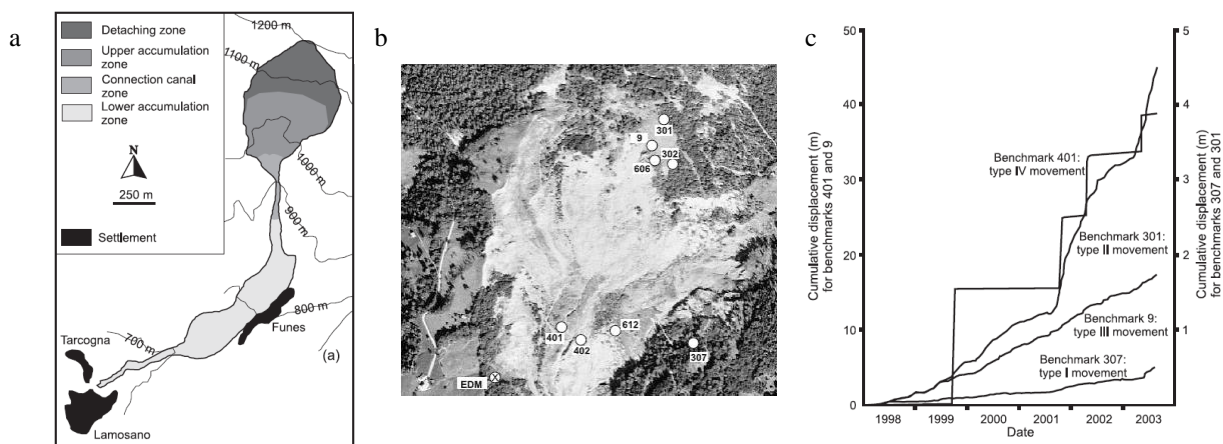


**Figure 1.9** The map and monitored displacement of Tessina landslide. a) morphodynamic zonation of the Tessina landslide, b) air-photo of the detaching and upper accumulation zone with the benchmarks identified, c) displacement time history for four representative monitoring points (Petley et al., 2004).

The Tessina landslide (Fig. 1.9a) is a seasonally active slope located on the southern slopes of Mt. Teverone, Italy. It consists of a complex system that has developed in Tertiary Flysch deposits (Petley et al., 2005). This landslide initiated in 1960; it has threatened two villages and has thus been the subject of detailed monitoring (Fig. 1.9c). The landslide extends from an elevation of 1200 m at the crown to 610 m at the toe of the mudflow. Its total track length is approximately 3 km from the crown to the toe, and its maximum width is about 500 m, with a maximum depth about 50 m in the rear scar area (Petley et al., 2005). Mantovani et al. (2000) divided the landslide into four main morphodynamic zones (Fig. 1.9a) as detaching, upper accumulation, connection canal, and lower accumulation zones. The connection canal zone and the lower accumulation zone are both monitored (Fig. 1.9b) using an automatic alarm system (Mantovani et al., 2000). Four distinct types of movements have been observed for this case (Fig. 1.9c). Observation and studies show great accordance of the landslide creeping movement to local pore pressure change.

The Vajont landslide (Fig. 1.10, Southern Alps, Italy) as another case of creeping landslide, best known for its dramatic failure (October 9, 1963). Such landslide led to the mobilization of  $2.7 \times 10^8 \text{ m}^3$  rocks that collapsed in an artificial lake and caused a giant wave that overtopped the adjacent dam and killed 1917 people by impacting a nearby village (Veveakis et al., 2007). This landslide was initiated after 2-3 years of continuous creep prior to the catastrophic failure (Selli & Trevisan, 1964; Carloni & Mazzanti, 1964; Ciabatti, 1964). Several studies focused on the final collapse exploration have been conducted (Anderson, 1980; Voight & Faust, 1982; Hendron & Patton), most of them emphasizing the crucial role that the feedbacks between landslide movement and pore water pressure within the sliding zone had in the generation of the extreme velocity that the mobilized soil mass attained (Veveakis et al., 2007).



**Figure 1.10** Photo of Vajont landslide.

### *1.3 Summary*

This chapter discussed several cases of creeping landslides, with emphasis to recent observations from the California Coast Ranges. For all the examined cases, movement were measured from in-situ equipment and/or remote sensing techniques. It has been shown that creeping landslides are common in mountainous areas and can affect economic activities, transportation infrastructure, and human life, with remarkable potential losses in case of catastrophic events. Such

considerations motivate the focus of this research, i.e., the development of mechanics-based methodologies to interpret changes in creeping landslide behaviors and predict their future trends.

The main features that creeping landslide possess are:

- i. They move continuously or episodically for long periods of time, from years to centuries with velocities within or around 1 m/year. Under specific conditions, some of them can experience catastrophic acceleration thus leads to high mobility failures with velocity around 1m/s.
- ii. This class of landslides usually involve a narrow shear zone with thickness ranging from a few centimeters to a few meters where most deformation occurs.
- iii. Their activity is governed by precipitation, with movements often taking place with a time lag from the rainfall event that causes it (i.e., delayed deformation). During wet seasons, when rainfall occurs frequently, they tend to accelerate; by contrast, when obvious rainfall events are absent, such as during dry seasons, they tend to decelerate.
- iv. The volume change or deformation in normal direction impact the landslide dynamics. It regulates the changes of velocity for stable sliding, as well as the occurrence of catastrophic acceleration.

Starting from these considerations, this thesis aims to implement physically based models to study creeping landslides that can take the above features into account in a unified modelling framework.

The goal would be to simulate slow, episodic movements of creeping landslides measured from ground-based monitor or remote sensing, calibrate the model parameters governing changes in landslide velocity, and capture the transition from stable pre-failure conditions to catastrophic runoff. By guaranteeing these capabilities, the thesis aims to bridge fluctuations in hydrological

forcing to corresponding instability conditions, including the possibility to assess when the loss of stability may lead to catastrophic failure.

## 2 SLOW-MOVING LANDSLIDES SIMULATION USING VISCOPLASTIC MODEL

Slow-moving landslides are widely observed in mountainous areas worldwide as described in chapter 1. Simulating the mechanisms that control changes in landslide movement, such as rainfall-induced changes in pore-water pressure, is therefore necessary to anticipate potential damaging effects on proximal infrastructure, habitat, and life. Motivated by this, a numerical method solving the water mass balance equation (Richards 1931), which governs pore-water pressure transients under infiltration is firstly illustrated in this chapter. The pore-water pressure changes lead to stress variation and corresponding deformation inside the active shear zone according to Terzaghi's effective stress principle. On such basis, a new viscoplastic constitutive law designed to capture different temporal trends in slow-moving landslides is presented. Typical viscoplastic models assume lack of pre-failure inelasticity and material viscosity prior to yielding. Nevertheless, laboratory tests indicate that viscous behavior can be observed when earthen material is still under elastic regime. A hybrid rheological law is proposed in this chapter aiming at capturing the pre-yield viscosity meanwhile assuring the simulation accuracy after the yield surface is surpassed. In the rest of this chapter, the proposed model is applied to artificial simple hydraulic loadings and three cases of interests, in order to validate its performance in capturing distinct modes of creeping landslide behaviors. (This chapter is prepared based on Li et al. (submitted), 2022).

## 2.1 Rainfall infiltration analyses

In this chapter, the simulations of slow-moving landslides are conducted on the basis of infinite slope model. Studied slopes consist of three components (Fig. 2.1): (1) a thick, rigid landslide body, (2) a thin deforming shear zone, and (3) undeforming stable material (e.g., bedrock) below the moving mass. The shear zone, varied from few centimeters to several tens of centimeters (Corominas et al., 2000; Leroueil, 2001; Puzrin & Schmid, 2011; Schulz et al., 2018), are the narrow bands where deformation and displacement concentrates. Here, the computation is focused on the hydraulic loading and mechanical performance inside the shear zone.

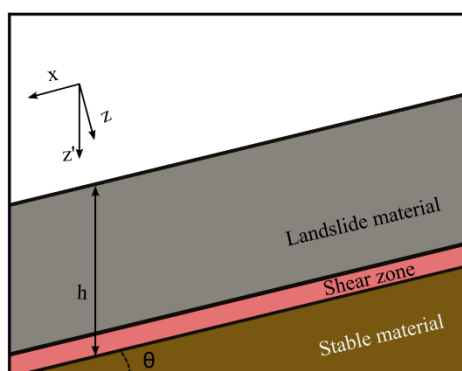


**Figure 2.1 Schematic of infinite slope model used for simulations in this chapter.**

Slow-moving landslides are commonly driven by pore-water pressure transients that can result from infiltrating precipitation. When infiltration occurs, the pore-water pressures rise and cause a decrease in the normal stress applied on the landslide material (Terzaghi, 1925). Consequently, the resistance to downslope sliding is diminished and this can trigger the activation or acceleration of the landslide. It is thus significant to solve the water pressure transients in order to interpret landslide dynamics. With this motivation, hydrologic models have been developed and applied to explain observed landslide velocity variations (Iverson and Major, 1987; Van Asch et al., 1996; Baum, 2000; Cohen-Waeber et al., 2018). On such basis, unsaturated effects from the local vadose

zone in landslides have also been shown to control the onset of landslide motion each year (Finnegan et al., 2021).

General infiltration process can be solved by water mass balance equation (Richards, 1931), a second order PDE. To conduct the analysis in linear form, nonlinear effects due to lack of full saturation are ignored (Yeh & Ward, 1980). This implies that the role of the two nonlinear functions typically used to reflect soil-water interactions above the water table (i.e., Water Retention Curve and Hydraulic Conductivity Function) is encapsulated into two constant parameters, namely the storage coefficient,  $S_s$ , and the saturated permeability,  $k_s$ . This simplification boils down to a linear diffusion equation widely used for simple pore-water pressure diffusion simulations (e.g., Iverson 1987; Cohen-Waeber et al., 2018; Berti & Simoni 2010) as

$$S_s \frac{dh}{dt} = \frac{\partial}{\partial z} \left( k_s \frac{\partial h}{\partial z} \right), \quad (2.1)$$

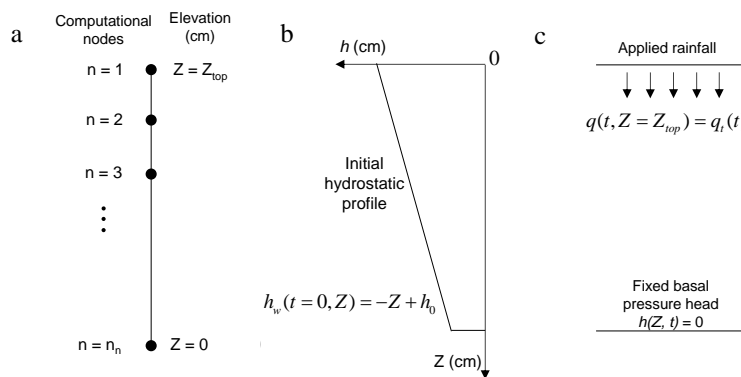


**Figure 2.2** Schematic representation of model discretization for an infiltration problem. a) Mesh structure and problem domain, b) Initial hydrostatic profile, c) boundary conditions (Li et al., 2019).

where  $z$  is the normal distance from the ground surface,  $h$  is water pressure head (pore-water pressure  $p_w$  divided by the water unit weight). This 2nd order PDE is solved here through a Finite Element algorithm implemented by Lizárraga and Buscarnera (2018), which enables a straightforward incorporation of permeability contrasts.

Through element discretization, defining the initial and boundary conditions (illustrated in Fig. 2.2), pore-water pressure transients induced by a given periods of rainfall infiltration can be computed. Fig 2.3 shows an example that by assigning the given flux at ground surface and setting the bottom as drained boundary (related parameters reported in Song et al., 2020), pore-water pressure transients solved by Wu et al (2016) can be ideally captured. This example validates that the pore-water pressure transients upon rainfall infiltration can be computed satisfactorily by proposed hydrological method.

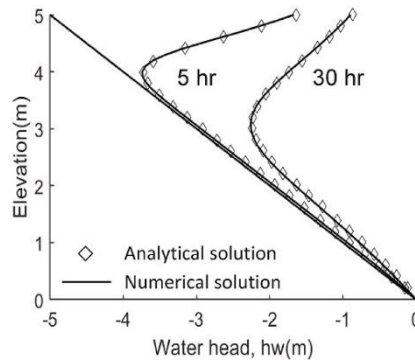


**Figure 2.3 Model simulation of water pressure profile under precipitation for 5 and 30 hours (analytical resolution from Wu et al., 2016, simulation parameters reported in Song et al., 2020).**

In order to operate simulations using the hydrological model, boundary conditions and permeability of each slope component (Fig. 2.1) are needed. Nereson et al. (2018) examined the differences in permeability within the Oak Ridge landslide, central California. The results indicated that the shear zone permeability is around two orders of magnitude lower than the overlying landslide material, while the stable material below the landslide shear zone has a permeability around two times higher than the landslide material. Based on this finding, saturated permeability of the three components (Fig. 2.1) in the model can be set as: shear zone saturated permeability,  $k_s^t = 0.01 k_s^s$  (shear zone permeability) =  $0.005 k_s^b$  (stable material permeability).

The top boundary condition is set from precipitation rate. A constant pore-water pressure boundary

condition three meters below the sliding surface is also set allocated in the stable material, which served as the external bottom boundary of our finite element analysis.

The hydrologic model is then linked to slope dynamics model through the effective normal stress. The simulated rainfall-induced changes in pore-water pressure cause changes in the effective normal stress, defined as  $\sigma' = \sigma - p_w$ , where  $\sigma$  is the total normal stress at the considered depth. The strain resulting from the changes in effective stress is computed through constitutive models outlined in section 2.2.

## *2.2 Material time-dependent properties and viscoplastic models*

Abundant constitutive models can be used to compute soil behaviors (Puzrin, 2013), from simple perfect plasticity frictional laws such as Mohr-Coulomb to more advanced models which involved more than ten parameters. In this chapter, the models are selected in efforts to depicting the landslide dynamics relevant properties of slow-moving landslide materials with less model parameters (physically-based). Here the widely observed time-dependent properties of earthen material, which encouraged the selection of constitutive models in this chapter, is firstly examined.

Earthen material normally exhibits time-dependent behaviors such as creep (Augustesen et al., 2004). As schematically illustrated in Fig. 2.4a & 2.4b, if a monotonically increased loading (stress,  $\sigma$ ) is applied on a soil sample until status A, then held constantly to status B. It can often be observed that in this scenario, strain can be triggered without changing the stress from A to B (Fig. 2.4c). In addition, the strength of earthen material obtained under different loading rates are normally distinct, in other words, rate-dependent properties (Gorman et al., 1978; Janbu et al., 1981; Mizoguchi et al., 2007; Rice et al., 2001) existed in earthen material. Aims at capturing these

time-dependent properties, viscoplastic models have been widely used (Mitchell et al., 1968; Liingaard et al., 2004; Marinelli et al., 2018).

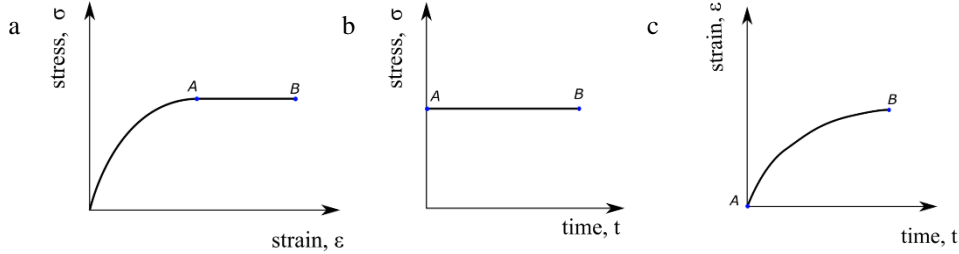


**Figure 2.4 Schematic of soil creep test. a) Stress-strain relationship; b & c) stress and strain temporal evolution.**

Focused on the case study sites, a recent study of the Two Towers landslide, northern California (study area of this paper) indicated that the shearing resistance is invariant under the range of sliding rates exhibited in the field (Schulz et al., 2018). Yet, the ring shear tests used to characterize the Two Towers landslide material showed the friction angle varies between  $\sim 21^\circ$  and  $\sim 24^\circ$  with shear rates from 0.01 to 1 mm/s. Such changes, although small, indicate some degree of rate-dependent behavior, which can be characterized with viscoplasticity (e.g., Mitchell et al., 1968). Regardless of the quantitative impact of viscous effects, use of rate-dependent strength models has computational benefits, in that it ensures stable computations in the presence of failure mechanisms (Perzyna, 1963; Needleman, 1988). Here, the inelastic nature of the model captures both shear strain (in sliding direction) and normal strain (in the direction perpendicular to the slope) through a viscoplastic flow rule (Perzyna, 1963; 1966)

$$\frac{d\gamma^p}{dt} = \phi(f) \frac{\partial g}{\partial \tau}; \quad \frac{d\epsilon^p}{dt} = \phi(f) \frac{\partial g}{\partial \sigma'}. \quad (2.2)$$

where  $\gamma^p, \epsilon^p$  are the plastic shear and normal strain,  $\tau$  and  $\sigma'$  are shear stress and effective normal stress.  $t$  is time,  $f$  is the yield function, and  $\phi(f)$  is the viscous nucleus that controls the magnitude

of the plastic strain rate. Meanwhile, the direction of the viscoplastic strain rate is defined by the stress gradient of plastic potential  $g$  (equals to  $f$  for an associated flow rule here). The Mohr-Coulomb yield criterion has been used in the formulation of the constitutive model:

$$f = \tau - \eta_y \sigma, \quad (2.3)$$

where  $\eta_y$  is the stress ratio at yield.  $\eta_y = \tan \varphi$ ,  $\varphi$  is soil friction angle at yield. With the application of this constitutive model, the viscous nucleus,  $\phi(f)$  (Eq. 2.2), as a core element of a viscoplastic rheology can be addressed. Here, viscoplasticity is implemented by following the overstress approach proposed by Perzyna (1966). Such framework can be regarded as a generalization of Bingham rheology (Bingham, 1917) for stress states and yielding criteria. As such, this framework has been widely adopted to interpret results of soil laboratory tests (Liingaard et al., 2004) and simulate landslide movement (Angeli et al., 1996; Oberender & Puzrin, 2016; Hu & Bürgmann, 2020). Standard expressions of the viscous nucleus rely on power law functions (Van Asch et al, 2007; Marinelli et al., 2018), as follows

$$\phi(f) = \begin{cases} \mu f^\alpha, & f \geq 0 \\ 0, & f < 0 \end{cases}, \quad (2.4)$$

where  $\mu$  and  $\alpha$  are model parameters. The expression above converges to a Bingham-like rheology for  $\alpha = 1$ . In addition, the use of McCauley brackets (i.e.,  $\phi(f) = 0$  for  $f < 0$ ) implies lack of strain rate prior to yielding, thus indicating a bilinear trend characterized by deformation rates only if the yield criterion is surpassed ( $f > 0$ ). However, evidence from soil laboratory tests suggest that this approach can be excessively restrictive for earthen materials, which exhibit time-

dependency much earlier than shear failure and even under over-consolidated states (Di Prisco & Imposimato, 1996; Augustesen et al., 2004).

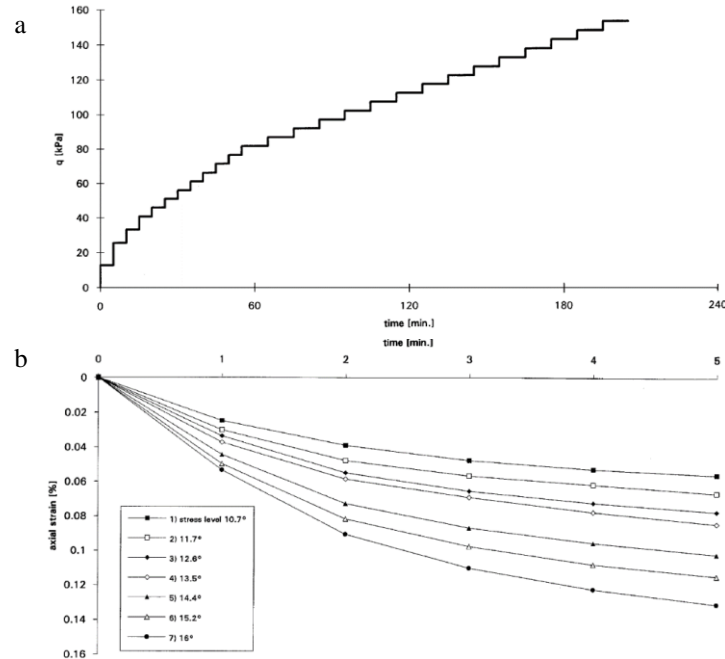


**Figure 2.5 laboratory tests indicate soil time-dependent behavior under elastic regime. a) loading history of the triaxial drained test, b) axial strain corresponding to several loading process, which is marked by its stress level (from di Prisco and Imposimato).**

Fig. 2.5 shows a stress controlled drained triaxial test conducted by Di Prisco & Imposimato, (1996). During the test, step-like instantaneous loading was applied in every five minutes (Fig. 2.5a). In response, the deformation was triggered in a time-dependent form from very early stage. To be specific, Fig 2.5b shows that under each stress status displayed by stress level (or in other work termed as mobilized friction angle, i.e., the arctan value of stress ratio  $\tau/\sigma'$ ), although the loading was conducted instantaneously, induced deformation grown gradually under reduced rate. This time-dependent behavior is observed even under relatively small stress ratios, at when the soil was still under elastic regime. To better accounts these effects, exponential forms have been proposed by di Prisco and Imposimato (1996) for sand:

$$\phi(f) = \mu e^{\alpha f}. \quad (2.5)$$

Although Eq. 2.5 allows non-zero pre-yielding viscous deformation, by letting them gradually decay as the stress state moves away from the failure envelope, its exponential form tends to produce excessive plastic strain rate once the yield surface is surpassed. An illustrative example is provided in Fig. 2.6a for a viscous nucleus characterized by  $\alpha=1$ . The strain rate is factorized by  $\mu$ , i.e., the parameter which scales its magnitude. The example shows that even a small excess of the yield threshold (only 3 kPa in our example corresponding to a water level increase of 0.3 m), the exponential law predicts a shear strain rate that is more than double the rate predicted by the Bingham-like model. To address this issue, a hybrid law blending the benefits of both the bilinear and the exponential forms is proposed as follows:

$$\phi(f) = \mu \ln(1 + e^{\alpha f}). \quad (2.6)$$

Such a model can capture both pre-yield viscoplastic strain and post-yield strain rates comparable to those of widely used Bingham-like models. This effect could not have been achieved by modulating the parameters of the exponential rheology in Eq. 2.5 alone, because setting an ideal strain rate at large overstress values ( $f=10$  kPa in Fig. 2.6b) leads to overestimation of the strain rates in the pre-yielding regime (strain developed when  $f$  is 10 kPa).

By contrast, the proposed hybrid law enables a Bingham-like rheology to be recovered at large overstress values, while capturing slow growth (but non-zero) viscoplastic strain rates in the pre-yield regime. Thus, it can be regarded as a more versatile platform to describe the rheology of earthen materials.

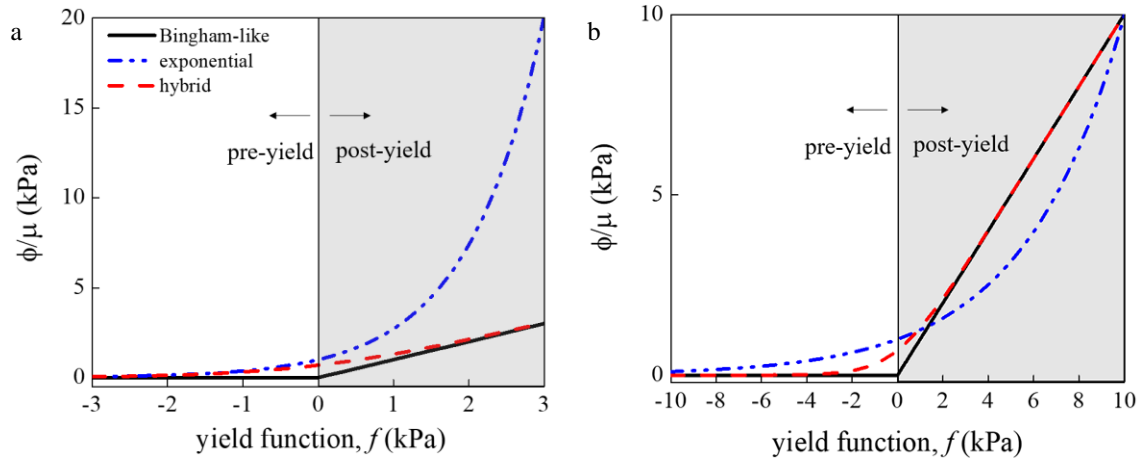


**Figure 2.6** Factorized viscous shear strain rate (by  $1/\mu$ , parameter that scales the magnitude) versus yield function value for different expressions of viscous nucleus. a) Dashed-dotted blue, dashed red, and black lines show model predictions for the exponential, hybrid, and Bingham-like models with  $a = 1$ . b) Blue, dashed red, and black lines show model predictions with  $a = 1$  for the hybrid and Bingham-like and  $a = 0.23$  for the exponential law. These simulations show that changing the power-law rheology term can lead to the same strain rate at the maximum yield function.

### 2.3 On-site indication of pre-yield viscosity

As mentioned above, laboratory measurements have shown that earthen materials exhibit viscous properties even while in the elastic domain (Di prisco and Imposimato, 1996; Sekiguchi, 1984). To test whether landslides exhibit pre-yield viscosity at the field scale, the relationships between measured landslide velocity and slope angle for the Boulder Creek and Mud Creek landslides in California are measured. The goal of this analysis is to link the landslide mobility to material stress status, aiming at investigating if viscous creeping occurs before material is driven to plastic domain (when the yield surface is surpassed).

The Boulder Creek landslide has a mean slope angle of  $15^\circ$  and has been exhibiting quasi-steady motion for decades or longer (Handwerger et al., 2013; 2019). The Mud Creek landslide is notably steeper with a mean slope angle of  $32^\circ$  and exhibited episodic motion for a minimum of 8 years before it collapsed catastrophically.

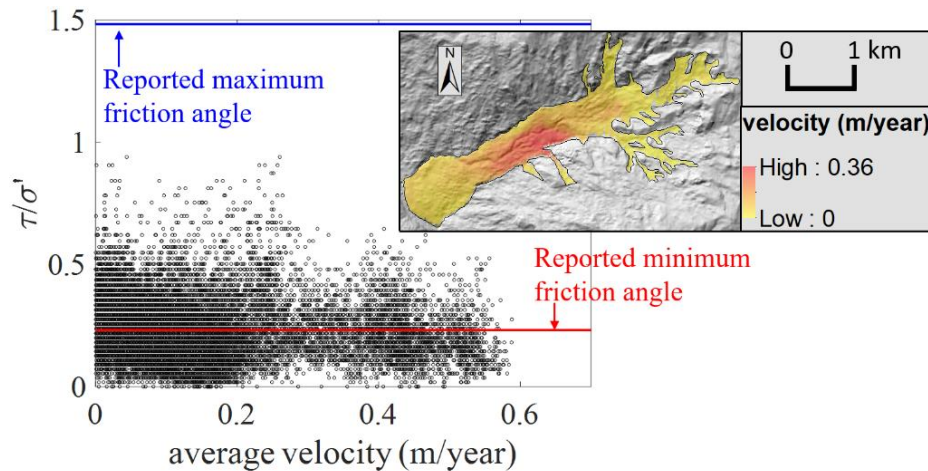


**Figure 2.7** Pre- and post-yield motion analyses of the Boulder Creek landslide, northern California. Right top image is the average downslope InSAR velocity map of the Boulder Creek landslide plotted on top of a hillshade. Main plot shows the ratio of shear stress divided by the effective normal stress vs. average velocity. The data are binned by pixels with the same slope angle. Horizontal red line shows the stress ratio corresponding to  $13^\circ$  friction angle, which is the minimum friction angle reported by Keefer and Johnson, 1978. Blue line shows the stress ratio of  $56^\circ$  friction angle, which is the maximum value reported by Roadifer, et al., 2009. InSAR data are from Handwerger et al. (2019) and DEM is from TanDEM-X. TanDEM-X data used is under copyright by the DLR.

The average landslide velocity was measured with satellite InSAR data in addition with the stress ratio calculated using a digital elevation model (DEM, the DEM for Boulder Creek and Mud Creek are from TanDEM-X, resolution 12 m). The slope angle determines the magnitude of self-loading components along both normal and tangential directions ( $z$  and  $x$  displayed in Fig. 2.1), which effects the ratio between shear and normal stress (stress ratio). For simplicity, it is assumed that the landslide thickness is constant and is 20 m for Mud Creek and 40 m for Boulder Creek (Handwerger et al., 2019). From classical slope stability analysis (Duncan, 1996), the relation between current stress ratio and the value at yield can indicate if the slope is predicted to be stable or unstable (the smaller the stress ratio, the further it departs from the material yield status).

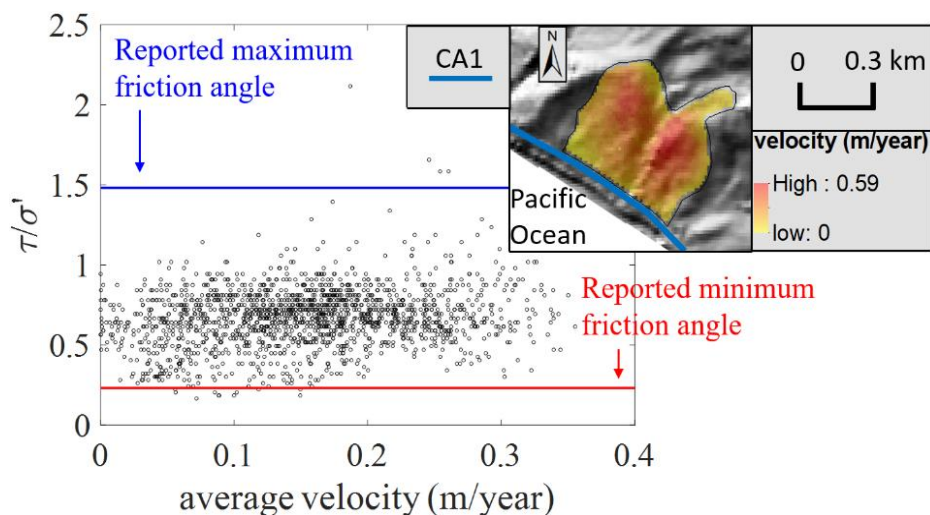


**Figure 2.8** Pre- and post-yield motion analyses of the Mud Creek landslide, central California. Right top image is the average downslope InSAR velocity map of the Mud Creek landslide zone plotted on top of a hillshade (DEM is from TanDEM-X. TanDEM-X data used is under copyright by the DLR). California State Highway 1 (CA1) is shown. The main plot shows the ratio of shear stress divided by the effective normal stress vs. average InSAR velocity. The data are binned by pixels with same slope angle. Horizontal red line corresponds to a stress ratio corresponding to  $13^\circ$  friction angle, which is the minimum friction angle reported by Keefer and Johnson, 1978. Blue line shows the stress ratio of  $56^\circ$  friction angle, which is the maximum value reported by Roadifer, et al., 2009.

Fig. 2.7 shows a comparison between the stress ratio and velocity for the Boulder Creek landslide.

To be noticed, for even low stress ratios, there are abundant landslide pixels that display non-negligible movement. Similarly, the relation between average InSAR surface velocity and stress ratio for Mud Creek landslide can be compared (Fig. 2.8). Due to the significantly steeper slope angle, Mud Creek has a much higher stress ratio overall, but also showed non-negligible movement at low stress ratios. Geotechnical investigations (Keefer and Johnson, 1983; Schulz et al., 2018; Nereson, 2018) recorded that for landslide materials hosted in the Franciscan Mélange, the rock type common to both landslides, the minimum friction angle is around  $13^\circ$  (stress ratio depicted in Fig. 2.8) and the maximum friction angle is around  $56^\circ$  (Roadifer et al., 2009). The findings indicate creeping deformation occurs at stress ratios well below the frictional limit and implies the landslides exhibit a viscous material rheology in the pre-yield regime.

## 2.4 Model testing

### 2.4.1 Response under monotonically increased pore-water pressure

In the previous section, factorized viscoplastic strain rates corresponding to different viscous nucleus expressions were compared. Here, to further illustrate each model's performance in response to more realistic pore-water pressure variations in landslides, all rheological laws are tested with a simulated  $p_w$  increase of 20 kPa over 180 days (i.e., 2 m water level rise) directly applied in the landslide sliding surface (Fig. 2.9b, other parameters are illustrated in the caption). These simulations were selected to approximate the pore-water pressure changes experienced by the active landslides in the California Coast Ranges (Iverson and Major, 1987; Schulz et al., 2018; Finnegan et al., 2021). The same value of viscous parameter  $\alpha = 1$  is used for all the simulations. Since the parameter  $\mu$  controls the magnitude of the plastic shear strain ( $\gamma^p$ ), here the factorized viscoplastic shear strain ( $\gamma^p/\mu$ ) is used as a basis for the model comparisons (Fig. 2.9a).

Fig. 2.9b shows the effective normal stress variation caused by this synthetic hydraulic event. The yield surface is approached after about 130 days when the effective normal stress crosses the yield surface. The model results show that the normalized shear strain computed from Bingham-like model occurs after 130 days while the exponential law predicts an earlier initiation of the movement after 60 days and a predicted movement three times larger than those obtained with a Bingham law (Fig. 2.9a).

The proposed new hybrid law predicts that shear strain develops after about 80 days, i.e., 50 days before the yield surface is approached, while providing predicted total movements at the end of the simulated pore-water pressure growth period similar to those obtained from the Bingham-like model (Fig. 2.9a). This result confirms once again the ability of the proposed hybrid rheology to

provide a compromise between Bingham-like models widely tested for the active stage of landslide motion and exponential formulations tailored for pre-yielding sliding behavior. Hereafter, parametric analyses are conducted to explore more broadly the effect of the model parameters.

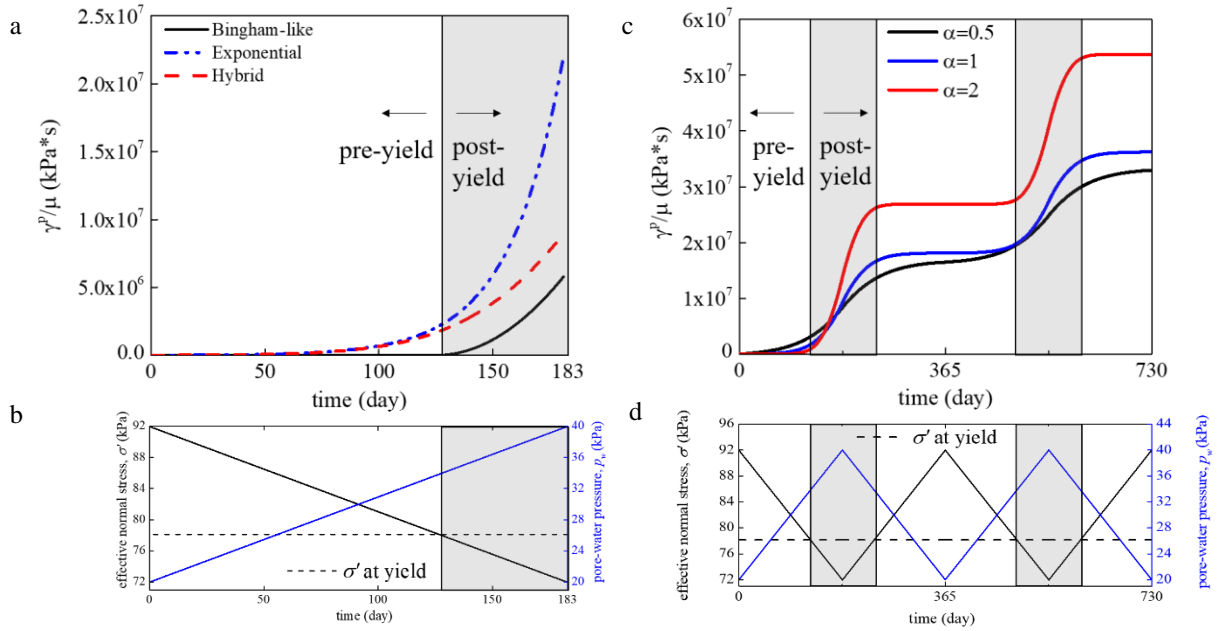


**Figure 2.9 Comparisons of the three viscoplastic models. Shear strain is computed from rheological laws in response of monotonic increased and cyclic pore-water pressure. a) Factorized viscoplastic shear strain calculated by each rheological law. b) Pore-water pressure monotonic variation and corresponding effective normal stress. c). Factorized viscoplastic shear strain calculated by different value of  $\alpha$ . d) Cyclic pore water pressure variation, corresponding effective normal stress change. For this synthetic landslide experiments the model parameters were chosen to resemble those reported for typical landslide settings in the California Coast Ranges (Schultz et al., 2018), thus setting  $h = 6$  m,  $\theta = 15^\circ$ ,  $\gamma_{sat} = 22$  kN/m<sup>3</sup>,  $\phi = 21^\circ$ .**

#### 2.4.2 Sensitivity tests for hybrid model mechanical parameters

The parameters of the proposed hybrid mechanical model are  $\phi$ ,  $\mu$  and  $\alpha$ . Among them,  $\phi$  determines the pore-water pressure limit enabling episodic slips (i.e., the landslide mobilization time), while  $\mu$  governs the magnitude of the displacement.  $\alpha$  influences the sensitivity of the sliding behavior against pore-water pressure variance; as an outcome, it affects the temporal history of the sliding response in both magnitude and rate (Fig. 2.9c).

Fig. 2.9d shows another simulated pore-water pressure change and the predicted landslide response. Here a triangular pulse of pore-water pressure of 20 kPa amplitude is applied (2 m of water level change) to approximate cyclic seasonal rainfall effects. Results show that when  $\alpha = 0.5$  (at 130 days), the sliding behavior prior to the stress path approaching the yield surface (50 days in advance) is discernible, while the displacement at the peak of pore-water pressure (around 180 days) is relatively small compared to the other simulations. By contrast, when  $\alpha = 2$ , pre-yielding effects are suppressed, and the response involves sharp episodic slips occurring only upon violation of the yield criterion. Thus, a higher  $\alpha$  leads to marked velocity changes between periods with higher and lower pore-water pressure, which represent the wet and dry seasons commonly experienced by real landslides (e.g., Corominas et al., 2000; Iverson and Major, 1987;). In other words, the history of the rates of landslide movement is governed by  $\alpha$ . In the next section we will calibrate these model parameters to data from three landslides in California.

### *2.5 Case study simulation*

In this chapter, Minor Creek landslide (displays episodic slips), Boulder Creek landslide (experiences quasi-continuous slip), and Mud Creek landslide (exhibits combination of episodic slips and quasi-continuous slip before failure catastrophically) have been selected as cases of study to test the model performance in capturing distinct types of landslide movements. The approach to calibrate proposed model is summarized in Table 2.1. Minor Creek was monitored between 1982-1985 using ground-based tools including piezometers for measuring pore-water pressure, and extensometers for monitoring displacement (Iverson and Major, 1987). Mud Creek landslide and Boulder Creek landslide have no ground-based data available and instead their displacement was measured between 2015 and 2017 through satellite-based InSAR techniques (Handwerger et al.,

2019). Although the Mud Creek landslide is known to have displayed stable sliding for more than 8 years, it failed catastrophically on a dry day (May 20, 2017) following a prolonged period of heavy rainfall. This sudden acceleration heavily damaged the California State Highway 1 (CA1), resulting in road closure between May 2017 and July 2018 and an estimated cost of \$54 million in repairs (Caltrans report, 2018). These landslides exhibit substantially different trends of movement over time, thus being good candidates to test the model versatility. Details of each case and correspondent model performance are discussed in the following sub-sections.

**Table 2.1 parameters calibration guidance**

Model parameter	Description	Calibration from	Calibration guidance
$k_s^t$	Saturated permeability	Pore-water pressure	Increase the value if the simulated pore pressure lags behind the measured data
$S_s$	Storage coefficient	Pore-water pressure	Increase if the simulated pore pressure amplitude is smaller than the measured data
$\varphi$	Friction angle	Movement	Decrease if the simulated sliding initiates later than observation or no sliding can be computed
$\alpha$	Rational of pre- and post-yield viscosity	Movement	Decrease if the movement difference in dry and wet season is larger than the measured data
$\mu$	Magnitude of viscosity	Movement	Increase if the simulated sliding magnitude is smaller than the measured data

### 2.5.1 Minor Creek landslide

Minor Creek landslide (Fig. 1.2), a compound, complex, slow-moving landslide, covers about 10 hectares in Redwood Creek drainage basin, northern California Coast Ranges. Iverson and Major (1987) provided three years detailed rainfall, groundwater and movement data (Fig. 2.10a and 2.10b) of this landslide from August 1982 to September 1985. The measured rainfall and pore-

water pressure are digitized based on the results shown in Fig. 10 of Iverson (2005). The average slope angle is  $15^\circ$ ; the thickness of the landslide along its longitudinal axis is 6 m; thickness of the shear zone is around 1 m (Iverson, 1985).

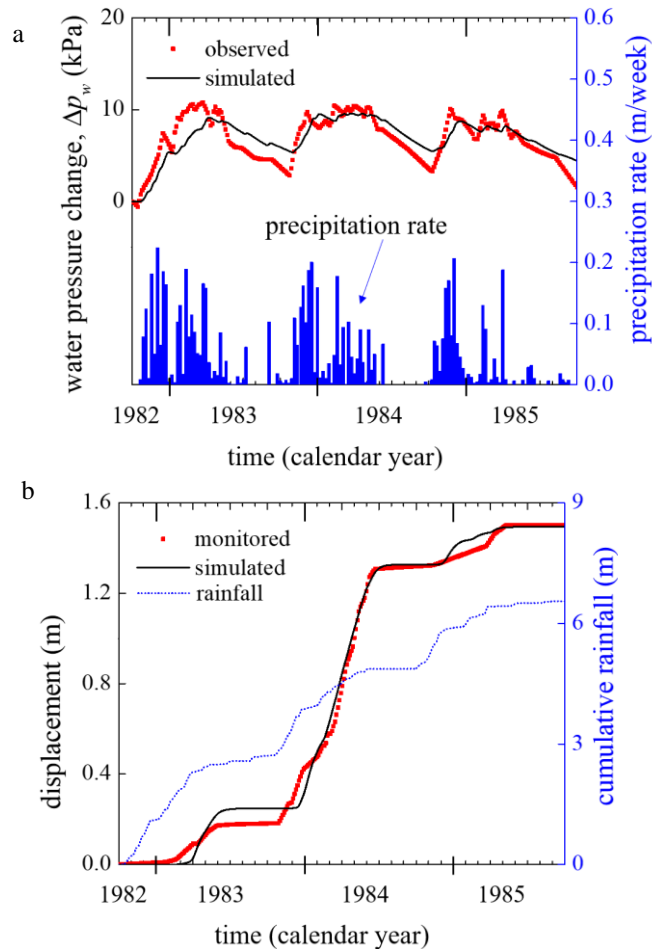


**Figure 2.10 Pore-water pressure, rainfall, and displacement of Minor Creek landslide during 1982 ~1985. a) Monitored and simulated pore-water pressure variation at the sliding surface and the precipitation rate; b) monitored and simulated landslide movement and cumulative rainfall, model parameters shown in Table 2. Monitored data are digitized from Iverson and Major (1987).**

The precipitation was monitored with a rain gage located at the site of the landslide, which is set as the top boundary condition of the hydraulic simulation in order to compute the rainfall induced pore-water pressure. The initial water pressure is set based on the shear zone pore-water pressure (Fig. 2.10a) assuming hydro-static conditions. The lower boundary condition is set as a constant

pore-water pressure three meters below the sliding surface as discussed above to reflect the observed hydrological condition that pore-pressure below barely changed. We calibrated our model parameters using trial and error following the calibration processes illustrated in Table 2.1. We found that our simulated pore-water pressure variation is consistent with the monitoring data (Fig. 2.10a) with the hydraulic parameters in Table 2.2.

The episodic slip movements of this landslide site (Fig. 2.10b) are driven by pore-water pressure changes during the wet and dry seasons. The pore-water pressure rises rapidly after onset of the wet season, remains relatively high during the wet season, and decreases slowly throughout the dry season. The landslide behaves in a way that is barely active during the dry season and moved evidently during the wet season (Fig 2.10b). Such step-like episodic displacements suggest a high value of parameter  $\alpha$ . Our best-fit model parameters are  $\alpha = 8$ ,  $\mu = 2.1 \times 10^{-8} \text{ (kPa*s)}^{-1}$ , and friction angle ( $\varphi$ ) =  $18.9^\circ$ . Fig. 2.10b illustrates that the landslide movement of Minor Creek landslide can be simulated satisfactorily by the proposed model.

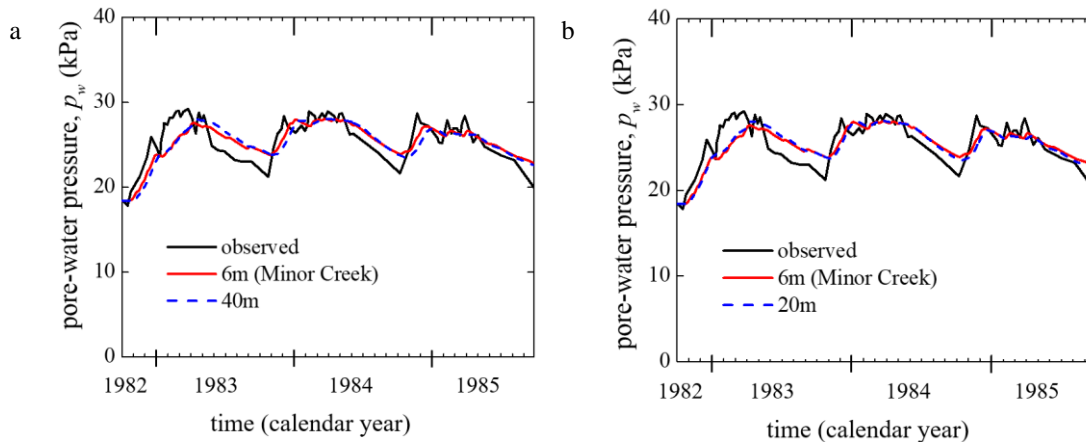
Importantly, the model captures the relatively large displacement displayed by Minor Creek during the year of 1984 and the smaller displacements in the other years. This large displacement was caused by a pore-water pressure change that approaches its highest value ( $\sim 10 \text{ kPa}$ ) for more than half of the year (Fig. 2.10a). The longer period with higher pore-water pressure leads to the apparent active landslide movement (around 1 m/year, still categorized as slow landslide by Hungr (2014)). The model results also show that there are some mismatches between our pore-water pressure and displacement simulations and the monitoring data, such as, predicting lower pore-water pressures during the wet season of water year 1983, and simulating higher pore-water pressures at each dry season compared with the monitors. The overall agreement between the

computed results and the field data corroborates the model's ability to describe both hydraulic and mechanical behavior in monitored landslides.

### 2.5.2 Hydrological simulation of Boulder Creek and Mud Creek landslide

Since there is no ground-based monitoring of pore-water pressure changes for Boulder Creek and Minor Creek landslides, the hydraulic responses are modeled based on observations from the Minor Creek site. To do this, the assumption is taken that the sliding surface of three studied cases each experiences the similar hydrological changes driven by rainfall, in that all three case studies located in Franciscan Mélange.

To calibrate the model parameters for Boulder Creek and Mud Creek, the observed data from Minor Creek are used. The modeled landslide thickness are adjusted for Minor Creek to back-calculate the hydraulic parameters required to match the observations assuming a 20 m thick (Mud Creek) and 40 m thick (Boulder Creek) landslide.



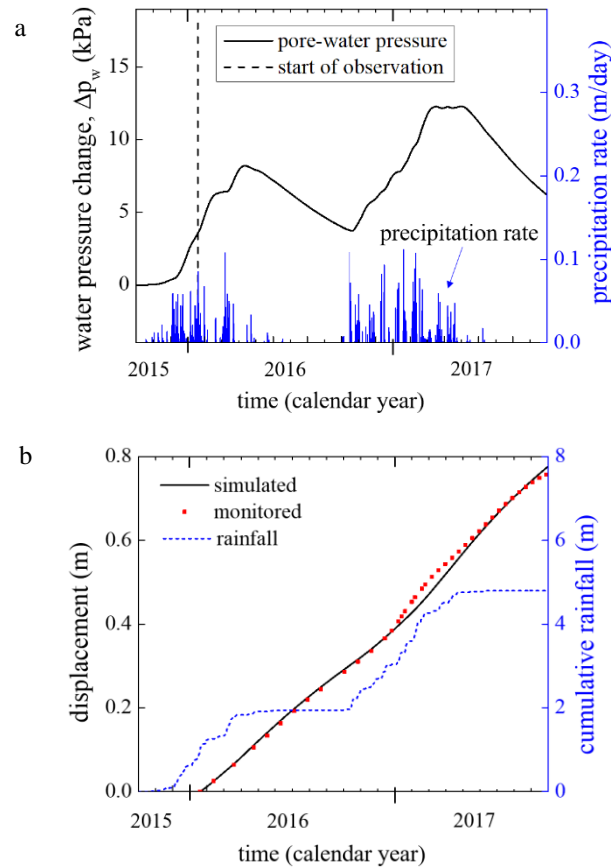
**Figure 2.11 Calibration of Boulder Creek and Mud Creek hydraulic parameters. a) Simulation of Minor Creek compared with 40 m depth. b) Simulation of Minor Creek with 20 m depth.**

Fig. 2.11a shows that when the thickness of Minor Creek is changed to 40 m (i.e., Boulder Creek thickness), the  $k_s^t$  (sliding material saturated permeability) increases to  $4.6\text{E-}6$  m/s and  $S_s$  (storage

coefficient) change to  $0.03 \text{ m}^{-1}$  to simulate a similar hydrological response. Similarly, as depicted in Fig. 2.11b, when the thickness of Minor Creek is changed to 20 m (i.e., Mud Creek thickness),  $k_s^t = 4.6\text{E-}6 \text{ m/s}$ , and  $S_s = 0.07 \text{ m}^{-7}$ . The deeper the infiltrated depth, the higher diffusivity is required to obtain the same hydrological response, thus leads to our simulated parameters difference for each case.

### 2.5.3 Boulder Creek landslide movement

Boulder Creek landslide (Fig. 1.2), northern California Coast Ranges, has displayed stable sliding for decades (Mackey and Roering, 2011). Although no ground-based monitoring of deformation or pore-water pressure is available at the site, surface movements from January 2016 to October 2017 (Fig. 2.12b) were measured by Handwerger et al. (2019) via InSAR images acquired by the Copernicus Sentinel-1 A/B satellites. The InSAR data show that the landslide exhibits a nearly constant displacement rate (quasi-continuous slow creeping with minor seasonal variations), thus with a temporal trend departing considerably from the episodic motion discussed previously. The average inclination of this landslide is around  $15^\circ$  (Handwerger et al., 2019) and the estimated thickness is 40 m (Mackey and Roering, 2011). The pore-water pressure time history at the landslide base is simulated by assuming a saturated initial condition (water level at ground surface as observed in slopes located in KJf from Schulz et al., 2018; Finnegan et al., 2021; Hahm et al., 2019) and used precipitation data (Fig. 2.12) acquired by NOAA as the surface boundary condition (around 50 km from the landslide). The hydrological parameters (Table 2.2) are back calculated as described in Section 2.5.2, where the reason that leads to different hydrological parameters for each case is also explained.



**Figure 2.12 Pore-water pressure change, rainfall, and displacement of Boulder Creek landslide during 2015 ~2017. a). Pore-water pressure variation at sliding surface and the precipitation rate; b). monitored and simulated landslide movement time history in addition with the cumulative rainfall, model parameters shown in Table 2.**

The computed pore-water pressure changes for Boulder Creek are shown in Fig. 2.12a. We used the same viscosity parameter  $\mu$  for Minor Creek here but in order to better capture the quasi-continuous motion of Boulder Creek we had to reduce the rheological parameter  $\alpha$  to 0.15 (section 3.2 and Table 2.1). We then back-calculated the friction angle  $\varphi$  and found a value around  $26^\circ$  (see Table 2.2) leads to satisfactory results in a form of continuous creep deformation (Fig. 2.12b). Our model is able to reproduce the overall landslide displacement of Boulder Creek after making these parameter adjustments.

#### 2.5.4 Mud Creek landslide movement

Finally, the model's ability to capture the slow and episodic motion displayed by the Mud Creek landslide prior to its catastrophic collapse (Fig. 1.2) is tested. The period of slow-motion between February 28, 2015, and May 13, 2017, is modeled and compared with the monitoring from InSAR data (Handwerger et al., 2019). The sliding profile is measured (Warrick et al., 2019) and here a depth of about 20 m (Handwerger et al., 2019) is assumed. As described in section 2.5.2 pore-water pressure changes (Fig. 2.13a) are simulated with the hydraulic model calibrated based on the procedures discussed before (Section 2.5.2). Precipitation data from the California Climate Data Archive (Fig. 2.13) located around 50 km from the landslide are used as the surface boundary condition.

We find that our hybrid rheological model can overall predict the landslide behavior using a value of  $\alpha = 0.7$ , which is between those used for the Minor Creek and the Boulder Creek sites. Notably, we find that the back-calculated friction angle value is around  $49^\circ$ . This high value is because Mud Creek is steep and thick (i.e., high initial stress ratio), and initial water level located near the ground surface (leads to high pore-water pressure). In this context, the initial basal pore-water pressure computed from stationary flow condition within an infinite slope is around 140 kPa, which is higher than typical conditions observed at other sites and used in soil laboratory testing. In fact, with an initial pore-water pressure around 20 kPa (induced by a water level around 2 m above the sliding surface) as monitored from shallower landslide located in KJf (Finnegan et al., 2021; Iverson and Major, 1987; Schulz et al., 2018), a much smaller friction angle would be back-calculated (around  $34^\circ$ ). Further validation of this value is provided in the Discussion section.

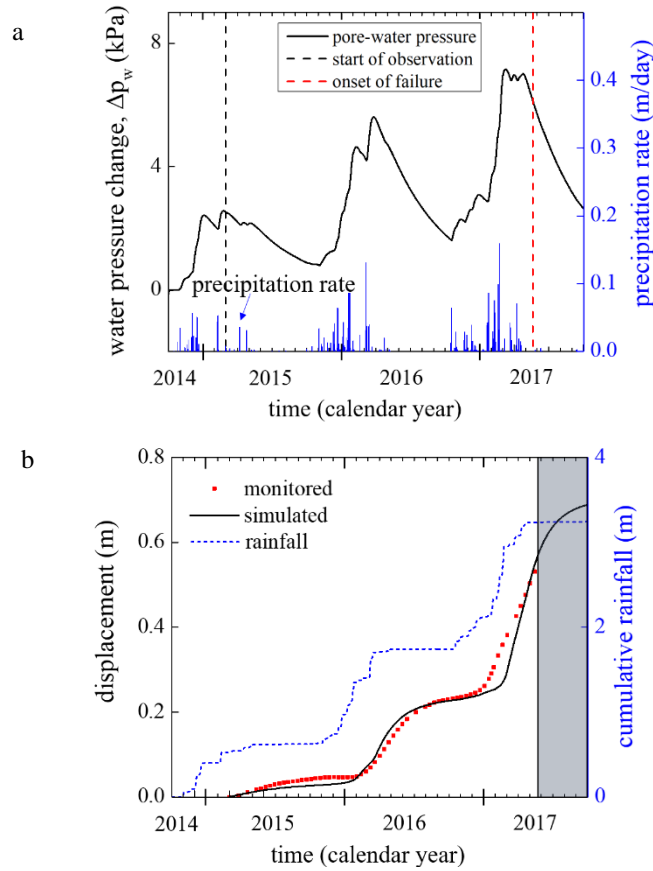


**Figure 2.13** Pore-water pressure change, rainfall, and displacement of Mud Creek landslide during 2014 ~2017. a) Simulated pore pressure variation at sliding surface and the precipitation rate. b) Simulated landslide movement time history and measured cumulative rainfall. The left boundary of the shaded rectangle represents the occurrence of catastrophic acceleration. Our model is not able to capture runaway instability and predicts a return to slow motion (black line inside gray shaded region).

**Table 2.2** model parameters for case studies

Model parameters	Minor Creek	Boulder Creek	Mud Creek
$k_s^t$ (m/s)	4.45E-6	4.6E-6	4.6E-6
$S_s$ (m <sup>-1</sup> )	0.27	0.03	0.07
$\alpha$ (-)	8.00	0.15	0.70
$\mu$ (kPa*s) <sup>-1</sup>	2.1E-8	2.1E-8	2.1E-8
$\phi$ (°)	18.9	26.1	48.5

Although our model cannot describe the runaway acceleration of the landslide, we allowed our simulations to continue to show what our model would have predicted for Mud Creek. Fig. 8b shows that a deceleration and return to stable sliding are predicted after May 20, when catastrophic runaway acceleration occurred. We show this to highlight a key limitation of our model framework and we outline plans to improve this model in the future in the Discussion section below.

## *2.6 Discussion*

The slow-moving landslides are widely observed worldwide, which can lead to crucial damage. It is of great significance to predict the response of those landslides to rainfall events in order to prevent and control the potential damage. In this chapter, we developed a new model to describe the motion of slow-moving landslides driven by precipitation. Our new model incorporates landslide activation under both pre-yield and post-yield scenarios, which is an advance over commonly used viscoplastic models. The model can be used to describe distinct types of landslide motion from episodic to quasi-stable sliding movements with simple parameter calibration.

Viscoplastic models have been used to interpret landslide creeping movement broadly. Most previous studies have used a Bingham-like rheological law (Fernandez-Merodo et al., 2014; Oberender and Puzrin, 2016), which ignores the viscous creeping before the material yield surface is approached. However, earthen materials are found to experience viscosity under the elastic domain (di Prisco and Imposimato, 1996; Sekiguchi, 1984), and therefore models need to account for this non-negligible deformation. Our analysis based on the InSAR data also suggested that some of the areas within active slow-moving landslides were creeping even when materials were in this elastic regime. With this motivation, we developed a new Hybrid rheological model (Eq. 6)

to account for the deformations. Most notably, taking pre-yield viscosity into account can significantly improve simulation of landslide movement.

We found that back-calculated friction angle values were much higher (especially Mud Creek) than those typically reported from lab measurements at landslide sites in KJf (Keefer and Johnson, 1983; Schulz et al., 2018). Our back-calculated friction values differ from these lab values for a few reasons. First, the back-calculated values account for large variations in landslide material properties at the field-scale, such as a block-in-matrix fabric known to the KJf (Roadifer et al., 2009). Second, high friction angles are required to maintain force balance when there are steep slopes, large landslide thickness, and high pore-water pressures. In clay-rich slopes relatively high values of back-calculated friction angle may also partly reflect the consolidation history of the material and the consequent nonlinearity of its strength envelope (Shi et al., 2017). Lastly, we assume that the material has zero cohesion. This assumption is reasonable because most of the earthen materials from landslide shear zones have experienced significant displacement which are likely to have rendered cohesive strength contributions negligible.

Our computational process is data-driven, which means that one site of parameters from a case study cannot be used directly to other cases although the landslide materials are located in the same geological unit (KJf). It is not a surprising result as the landslides are distinct from the viewpoint of topography, average slope angle ( $15^{\circ}$  to  $38^{\circ}$ ); and depth of sliding surface (6-40 m). Some local conditions are also distinct site by site, such as the landslide size (Handwerger et al., 2013; Keefer and Johnson, 1983) and rainfall conditions. In addition, the KJf material properties can also be substantially different (Keefer and Johnson, 1983; Nereson, 2018).

One of the major benefits of predicting the landslide movement using viscoplastic models is that they can describe post-failure landslide motions. This provides an advantage over most elastoplastic models which lack unique solutions in post-failure scenarios (e.g., Puzrin, 2012), thus cannot be used to quantify landslide creep movement behaviors. However, several studies have shown that the viscosity of some slow-moving landslide materials is negligible, especially under the small dynamic range of motion exhibited by slow-moving landslides (e.g., Schulz et al., 2018; Iverson, 2020). Further complicating the issue, there is often a large discrepancy (more than three orders of magnitude) between viscosity values obtained from laboratory tests and compared with the ones gathered from case study parameter back calculations (Angeli et al., 1996; Van Asch et al., 2007). Also, there are other considerations that can result in rate-dependent properties such as thermo-mechanical interactions (Alonso et al., 2016; Veveakis et al., 2007), which are not considered in this paper. These prior studies indicate that viscosity might not be solely sufficient to interpret slow-moving landslide behaviors. It thus encourages us to take other factors into account, such as slope dynamics and flow-deformation couplings inspired by Hutchinson (1986) and Iverson (2005) in our future work.

## *2.7 Summary*

This chapter presents a framework to compute the changes in subsurface pore water pressure driven by precipitation and dynamics of slow-moving landslides. The hydraulic accounts for water mass diffusion across heterogenous slope profiles. Similar to previous work, it is found that the simple 1D diffusion model can capture pore-water pressure variations that are consistent with ground-based monitoring data.

The hydrologic simulations are then used as an input to drive the landslide model. The sliding behavior of three real and three simulated landslides are simulated using the proposed new hybrid viscoplastic model. It shows that a hybrid viscous nucleus combined the benefits of a post-yield Bingham-like rheology that is commonly used to model landslides, and a pre-yield creep that can describe precursory landslide deformation. The results show that the hybrid rheology is able to capture a variety of delayed landslide movements observed at the three landslide sites in the California Coast Ranges. Although a complete assessment of spontaneous transitions to catastrophic acceleration requires some other factors such as thermos-mechanical interaction, progressive connecting of discrete failure surfaces, or a fully coupled hydro-mechanical formulation, which are not addressed in this work. The analyses discussed here provide a versatile strategy to interpret velocity changes in creeping landslides governed by climate change by incorporating explicitly both the hydraulic and mechanical effects responsible for their manifestation, thus offering a springboard for future extensions including coupled pore-water pressure feedbacks and post-failure dynamics.

### **3 DYNAMICS OF SLOW-MOVING LANDSLIDE CONTROLLED BY INELASTIC HYDRO-MECHANICAL COUPLINGS**

Slow-moving landslides affect infrastructures and communities, often causing extensive economic loss. Although it is known that the dynamics of landslide is controlled by hydro-mechanical processes, few analytical models aimed at diagnosing the causes of changes in velocity consider how the inelastic constitutive properties of the shear zone materials modulate the coupling between fluid flow and landslide motion. To address this problem, this chapter proposes a simulation framework incorporating rainfall-induced, deformation-mediated pore water pressure transients at the base of active landslides. The framework which involves the computation of two sequential diffusion processes, one within an upper rigid-porous sliding block, and another affecting the inelastic shear zone, is firstly introduced. It is then used with an elastic-perfectly plastic frictional model to simulate the hydro-mechanical behaviors of a synthetic slope upon rainfall infiltration. Results illustrate that the model can be used to interpret the interaction between matrix deformation and pore-water pressure dissipation. In the remaining of this chapter, the coupled method is used to interpret time histories of active slope motion at multiple sites located in the California Coast Ranges, to test its performance in capturing the dynamics of slow-moving landslides (this chapter is modified from Li et al (submitted)., 2022).

### *3.1 Slow-moving landslide hydro-mechanical couplings*

Slow-moving landslides are phenomena which unfold over several years, often even decades, with major implications for the serviceability of infrastructures, the safety of communities, and the local economy (Nappo, et al., 2019). The mobilization of these landslides is governed by environmental factors, such as precipitation (Handwerger et al., 2013; Bennett et al., 2016; Hilley et al., 2004; Cascini et al., 2010; Finnegan et al., 2021). In this context, the role of the volumetric deformation on the sliding behavior has been extensively explored through field and laboratory measurements (Schulz, et al., 2018; Agliardi et al, 2020); it highlights the significance of coupled effects between infiltration, volume change, and excess pore water pressure generation during cycles of landslide reactivation, motion, and arrest.

Slow-moving landslides can be examined numerically through standard FEM algorithms solving momentum and water mass balance (Daichao et al., 2003). While these approaches can be extended to encompass stages of catastrophic acceleration, it is typical to study triggering and runout stages through distinct formulations. For example, triggering processes are often examined by means of quasi-static methods based on perfectly plastic, elastoplastic or viscoplastic models with embedded failure criteria and accounting for long-term hydrologic processes (Duncan, 2014; Lu et al, 2013; Buscarnera & di Prisco, 2013). By contrast, to capture high mobility events, mesh-free computational tools such as MPM and SPH are coming to prominence to explore large deformation over short amounts of time (Bandara & Soga, 2015; Soga et al, 2016). All these methodologies demand the incorporation of material inelasticity, while usually requiring relatively high computational cost, especially if a seamless connection between slow hydrologic triggering and rapid post-failure movements is desirable.

To explore the landslide dynamics in a simplified, yet computationally efficient manner, analytical methods relying on the infinite slope model have been proposed. In the frame of liquefaction-induced runout, early contributions by Hutchinson (1986) led to a sliding-consolidation framework linking landslide velocity to excess pore-water pressure dissipation. Despite the benefits of this approach, the initiation of the movement was not explicitly resolved, in that triggering was treated as an initial condition to be assessed separately (including through the quantification of the excess pore water pressure at the onset of dynamic motion). The role of the soil nonlinearity on the flow-deformation dynamics was not also included, in that excess pore pressure dissipation was modeled via elastic protocols based on a constant consolidation coefficient. A more profound connection between landslide triggering and propagation was later proposed by Iverson (2005), who extended this early model to encompass excess pore pressure change through basal flux boundary conditions mediated by the soil dilation. Also in this case, however, the ability of the shear zone inelasticity to affect both fluid flow and landslide motion was not included, thus suppressing possible changes in the timescale of excess pore pressure dissipation due to inelastic deformation (Rice, 1975; Di Prisco, 1995; Chen & Buscarnera, 2021). In this chapter, the dynamics of landslides is reexamined through a recent analytical reformulation of the sliding-consolidation framework able to suppress the above limitations, while enabling readily deployable, low computational cost simulations of the entire life cycle of triggering and runout (Chen & Buscarnera, 2022). For this purpose, the framework is extended to incorporate the rainfall infiltration within the sliding material, thus connecting ground surface precipitation to the deformation dynamics.

### *3.2 Coupled flow-deformation framework*

Field evidence suggests that the deformation of creeping landslides originates from localized basal shear zones with thickness varying between several centimeters to a few meters (Corominas et al.,

2000; Leroueil, 2001; Puzrin & Schmid, 2011; Schulz et al., 2018; Finnegan et al., 2021). This simple schematic implies that the upper block slides downslope as a rigid body and the stable material underneath (e.g., bedrock) is inactive (Fig. 3.1a). When precipitation occurs, infiltration impacts, sequentially, the landslide material and the shear zone, generating corresponding pore-water pressure transients. As an outcome, under a constant total overburden the normal effective stress decreases in response to the augmented pore-water pressure (Fig. 3.1b) in accordance with Terzaghi's (1925) effective stress definition. The stress components of shear zone material can be defined as:

$$\sigma_d = \gamma_s h_w \cos^2 \theta$$

$$\tau_d = \gamma_s h_w \sin \theta \cos \theta, \quad (3.1)$$

$$\sigma' = \sigma_d - p_w$$

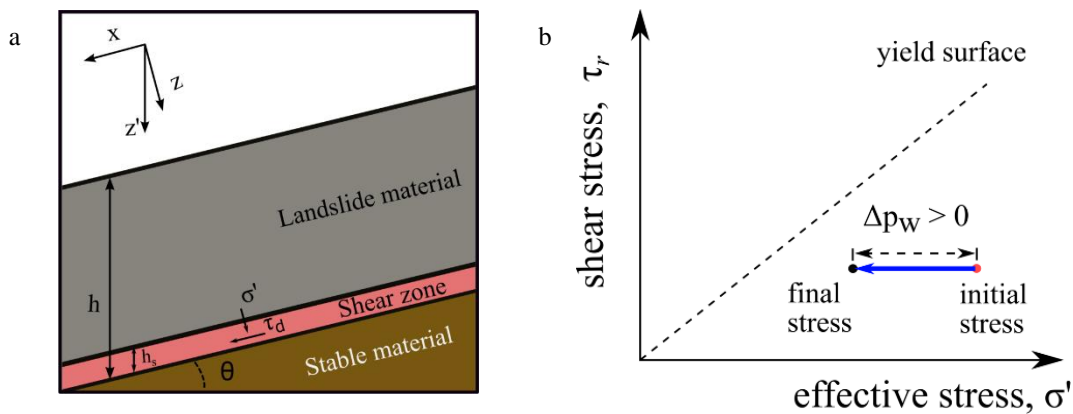


**Figure 3.1 Schematic of slow-moving landslide slope profile and precipitation induced stress change. a) slope components, b) material stress path induced by rainfall infiltration.**

where  $\sigma_d$  and  $\tau_d$  are the normal total stress and shear stress determined from the slope inclination  $\theta$ , the thickness of active landslide  $h$ , and the height of water level,  $h_w$ , and  $\gamma_s$  represent the

saturated unit weight of the soil, respectively.  $\sigma'$  is the effective normal stress, and  $p_w$  is the pore-water pressure. Incorporating elastoplastic constitutive models for the shear zone material enables the landslide dynamics to be analyzed by simulating the deformation in both the tangential and normal direction caused by hydrologic processes.

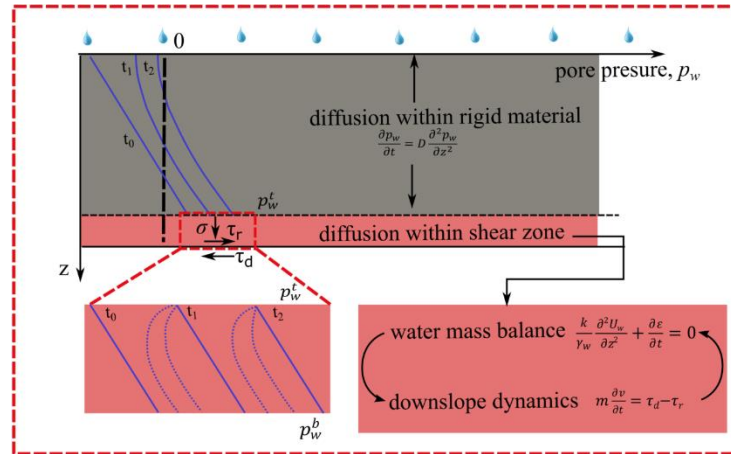


**Figure 3.2 Schematic of infinite slope model used for coupled hydro-mechanical analyses. The governing equations for each diffusion process inside the landslide material and the basal shear zone are also illustrated.**

In this chapter, the hydro-mechanical equations controlling the dynamics of a creeping landslide sliding are set up on a fluid saturated inelastic shear zone. The formulation involves two separate diffusion process: one within the upper landslide mass, here treated as a porous, rigid block; another within the inelastic shear zone (Fig. 3.2). The former diffusion mechanism acts as the main external loading for the basal shear zone, while the latter sets the timescale of excess pore pressure development and dissipation in response to inelastic deformation.

### 3.2.1 Pore-water pressure diffusion within the sliding block

The movement of creeping landslides is governed by precipitation. Upon rainfall, water diffuses within the sliding material and eventually weakens a deeper shear zone. The upper sliding material normally does not show discernible deformation and can be treated as a rigid block. By solving

the water mass balance in this portion of the system, the pore water pressure transients responsible for the mobilization of a landslide can be examined. Indeed, the transient pore water pressure resulting from this analysis represents a triggering agent for inelastic deformation of the basal shear zone. Such transients are computed on the basis of Eq. 3.2, where diffusive effects are encapsulated into two constant parameters, namely the storage coefficient,  $S_s$ , and the saturated permeability of sliding material,  $k_s^t$ , (e.g., Iverson 2000; Cohen-Waeber et al., 2018; Berti & Simoni 2010), as follows:

$$S_s \frac{\partial p_w}{\partial t} = k_s^t \frac{\partial^2 p_w}{\partial z^2}, \quad (3.2)$$

where  $z$  is the normal distance from the ground surface. In this manuscript, the above equation is solved through the numerical algorithm proposed by Lizárraga and Buscarnera (2018). For the sake of simplicity, the hydrologic triggering is simulated by imposing flow (infiltration) conditions at the top of the sliding material and an impervious boundary at its bottom. This is a simplification justified by the frequent observation that basal shear zones possess lower hydraulic conductivity compared to other portions of a slope profile (e.g., Nereson et al., 2018). While more general analyses accounting for permeability contrasts can be carried out (Lizarraga and Buscarnera, 2018), this simplification has limited qualitative bearing on the analyses shown in this paper and will therefore be used as a convenient working hypothesis.

We simulate dry and wet seasonal changes that are typical of sites in California (Swain, 2021). During the simulated wet season, we apply a surface flux boundary condition that is equivalent the precipitation. During the dry season, when rainfall stops, we apply a constant pressure condition with a value coincident with the surface pore-water pressure recorded at the beginning of a water cycle. This strategy ensues the infiltrated water to be dissipated during the dry season in a one-

dimensional setting and matches the measured behavior at several field-monitoring CA landslide sites (e.g., Iverson and Major, 1987; Schulz et al., 2018; Finnegan et al., 2021).

### 3.2.2 Coupled flow-deformation within the shear zone

Within the shear zone, coupled flow-deformation processes can be simulated by analyzing simultaneously the downslope dynamics and water mass balance (Chen and Buscarnera, 2022). In this portion of the slope, the initial stress state (Eq. 3.1) is altered by the interaction between water flow and deformation. From a mechanical viewpoint, the downslope dynamics implies:

$$ma = \tau_d - \tau_r, \quad (3.3)$$

where  $m$  is the mass of the sliding block,  $a$ , its acceleration,  $\tau_d$ , the driving shear stress,  $\tau_r$ , the reaction stress supplied by the shear zone, here regarded as a function of the local constitutive response, as follows:

$$\dot{\tau}_r = G(\dot{\gamma} - \dot{\gamma}^p); \sigma' = E_{oed}(\dot{\epsilon} - \dot{\epsilon}^p), \quad (3.4)$$

where  $G$  is the elastic shear stiffness,  $E_{oed}$  is elastic oedometric modulus.  $\epsilon$  and  $\epsilon^p$  are the total and plastic normal strain;  $\gamma$  and  $\gamma^p$  are the total and plastic shear strain. Eq. 3.4 involves both shear stress and the normal effective stress. The latter is indeed a function of the normal strain and is controlled by volume change. As it will be discussed in the following, plastic strain increments can be computed with constitutive models. However, to link the local shearing response to the landslide movement, the shear strain rate,  $\dot{\gamma}$ , is here computed by assuming a linear velocity profile within the shear zone (MiDi, 2004; Pastor et al., 2015; Siman-Tov & Brodsky, 2021), as follows:

$$\dot{\gamma} = \frac{v}{h_s}. \quad (3.5)$$

This choice enables us to use Eq. 3.3 ~ 3.5 to derive the following sliding equation:

$$\rho_{sat} h \ddot{v} = \dot{\tau}_d - G \frac{v}{h_s} + G \dot{\gamma}^p. \quad (3.6)$$

The normal effective stress change in Eq. 3.4 must follow from rates of volume change compatible with the water mass balance in the shear zone. Here, this process is simulated by treating the fluid as incompressible and considering the rate of volume change as the only source of diffusive feedbacks within the shear zone (Sloan & Abbo, 1999; Mihalache & Buscarnera, 2016), as follows:

$$\frac{k^b}{\gamma_w} \frac{\partial^2 U_w}{\partial z^2} + \dot{\epsilon} = 0, \quad (3.7)$$

where  $k^b$  is the saturated permeability of the shear zone material, and  $\gamma_w$  is the unit weight of water,  $U_w$  is the water head multiply water unit weight. The normal strain rate consists of elastic and plastic deformation ( $\dot{\epsilon} = \dot{\epsilon}^e + \dot{\epsilon}^p$ ). Therefore, we can rewrite Eq. 3.7, as follows:

$$\frac{k^b}{\gamma_w} \frac{\partial^2 U_w}{\partial z^2} + \frac{\dot{\sigma}_d - \dot{p}_w^b}{E_{oed}} + \dot{\epsilon}^p = 0, \quad (3.8)$$

from which it is readily apparent that the inelastic volume change regulates the pressure diffusion process across the sliding zone.

In our model, the time varying pore-water pressure input,  $\dot{p}_w^t$ , at the boundary between the sliding block and shear zone (here computed through the uncoupled diffusion analysis in Eq. 3.2) will serve as a forcing in Eq. 3.8, which is aimed at computing the change of the pore-water pressure at the bottom of the landslide ( $\dot{p}_w^b$ ). While Eq. 3.8 is a second order partial differential equation (PDE), a parabolic approximation of the  $U_w$  profile compatible with analytical solutions of soil consolidation (Wood, 2004) is here used to condense the analysis of the landslide dynamics to an ordinary differential equation (ODE) that can be solved with numerical and/or analytical solutions. Specifically, use of a parabolic pressure profile implies:

$$\frac{\partial^2 U_w}{\partial z^2} = \frac{2(p_w^{sb} - p_w^b)}{h_s^2 \cos^2 \theta}. \quad (3.9)$$

Where  $p_w^b$  represent the basal shear zone static pore-water pressure corresponding to a hydrological forcing at the top of shear zone ( $p_w^{sb} = p_w^t + h_s \cos \theta \gamma_w$ ). Combining Eq. 3.9 with Eq. 3.7, as set of coupled governing equations conveying the effect of the inelasticity of the shear zone material on the landslide dynamics can be obtained, as follows:

$$\dot{p}_w^b = \frac{2Ek^b}{\gamma_w h_s^2 \cos^2 \theta} (p_w^{sb} - p_w^b) + E_{oed} \dot{\epsilon}^p + \dot{\sigma}_d, \quad (3.10a)$$

$$\rho_{sat} h \ddot{v} = -G \frac{v}{h_s} + G \dot{\gamma}^p + \dot{\tau}_d. \quad (3.10b)$$

Its solution can be addressed once the inelastic deformation terms in both equations are specialized with constitutive models.

### 3.2.3 Constitutive models

While an extensive number of constitutive relations for soils is nowadays available (Puzrin, 2012), a natural choice for a specialized form of the proposed framework is a perfectly plastic frictional law (Davis & Selvadurai, 2005). In fact, such constitutive choice enables simplicity, economy of model parameters, and straightforward identification of soil constants for a variety of landslide case studies (Van Asch, 2007; Corominas, 2007; Conte et al., 2014; Schulz et al., 2018). In case of frictional plasticity, it follows:

$$f = \tau - \sigma' \tan \varphi, \quad g = \tau - \sigma' \tan \psi, \quad (3.11)$$

where  $f$  and  $g$  are yield function and plastic potential respectively.  $\varphi$  is the friction angle and  $\psi$  the dilation angle. In this scenario, the plastic deformation in both normal and tangential direction can be obtained as:

$$\dot{\varepsilon}^p = \Lambda \frac{\partial g}{\partial \sigma'}; \dot{\gamma}^p = \Lambda \frac{\partial g}{\partial \tau_r}, \quad (3.12)$$

where  $\Lambda$  is the plastic multiplier (i.e., a scalar quantify the magnitude of plastic effects) determined by the consistency condition of the yield surface. By using normal effective stress and shear strain as control parameters (Buscarnera et al., 2011), it follows that:

$$\Lambda = \frac{1}{H-H_2} \left( \frac{\partial f}{\partial \sigma'} \sigma' + \frac{\partial f}{\partial \tau_r} G \dot{\gamma} \right), \quad (3.13)$$

where  $H$  is the hardening modulus,  $H_2$  is a plastic modulus determined by the control conditions used to quantify plastic effects. Based on Eq. 3.11, the moduli in Eq. 3.6 can be expressed as:

$$H = 0; H_1 = -\frac{\partial f}{\partial \sigma'} E_{oed} \frac{\partial g}{\partial \sigma'} = -\tan\varphi E_{oed} \tan\psi; H_2 = -\frac{\partial f}{\partial \tau_r} G \frac{\partial g}{\partial \tau_r} = -G. \quad (3.14)$$

Here,  $H = 0$  in that the selected constitutive law is perfect plastic. Introducing Eq. 3.14 into Eq. 3.13 and combining the result with Eq. 3.10, the complete set of coupled governing equations based on the selected constitutive law is:

$$\dot{p}_w^b = \frac{k^b E_{oed}}{\gamma_w} \frac{2(p_w^{sb} - p_w^b)}{h_s^2 \cos^2 \theta} A + B \frac{1}{\tan\varphi} \frac{Gv}{h_s} + \dot{\sigma}, \quad (3.15)$$

$$\rho_s h \dot{v} = \frac{k^b E_{oed}}{\gamma_w} \frac{2(p_w^{sb} - p_w^b)}{h_s^2 \cos^2 \theta} A \tan\varphi - B \frac{Gv}{h_s} + \dot{\tau}_d.$$

where  $A$  and  $B$  are dynamic coefficients expressed as  $A = \frac{G}{G + \tan\varphi E_{oed} \tan\psi}$ , and  $B = \frac{\tan\varphi E_{oed} \tan\psi}{G + \tan\varphi E_{oed} \tan\psi}$

respectively. From Eq. 3.15, the interaction between shear zone hydraulic flow and mechanical process can be computed.

### 3.2.4 Nondimensionalization

It is often beneficial to identify nondimensional timescales controlling the dynamic system because it helps understand the relation between distinct timescales involved in our study such as hydrological forcing and water diffusion. Also, it can reduce the complexity of governing equations. In this study, standard nondimensionalization strategies (Tan, 2011) are used. This involves rescaling the system variables by normalizing them for a reference quantity, here denoted through an overhead hat (e.g.,  $\hat{t}$  for a reference time). On such basis, the normalized quantities can be displayed through an overhead tilde (e.g.,  $\tilde{t}$  for normalized time, equals to  $t/\hat{t}$ ). Selection of reference quantities with clear physical meaning facilitates the identification of the underlying mechanics. Here, the reference time is selected as the duration of forcing ( $\hat{t} = T$ ), while other reference quantities are  $\hat{\sigma} = \hat{p}_w = \sigma_0 = \rho g h \cos \theta$ ,  $\hat{\tau} = \tau_0 = \tan \theta \sigma_0$ ,  $\hat{a} = \tau_0 / \rho h$ ,  $\hat{v} = \hat{a} \hat{t}$ .

Accordingly, the governing equation (Eq. 3.15) can be re-written as:

$$\dot{\tilde{p}}_w^b = 2T_{lc}^e A (\tilde{p}_w^{sb} - \tilde{p}_w^b) - B \frac{\tan \theta}{\tan \psi} T_{lw}^e \tilde{v} + \tilde{\sigma}_d, \quad (3.16)$$

$$\ddot{\tilde{v}} = 2T_{lc}^e A \frac{\tan \psi}{\tan \theta} (\tilde{p}_w^{sb} - \tilde{p}_w^b) - B T_{lw}^e \tilde{v} + \tilde{\tau}_d.$$

where A and B are the dynamic coefficients resulting from frictional plasticity.  $T_{lc}^e = \frac{E_{oed} k_s^s T}{\gamma_w h_s^2 \cos^2 \theta}$ , is the ratio of total forcing time divided by the characteristic consolidation time for elastic material, which controls the shear zone hydraulic diffusion when shear zone deforms elastically. In addition, considering the standard expression of the shear wave velocity in an elastic medium,  $v_s^e = \sqrt{G/\rho}$ , it is possible to define a reference time of shear wave to travel across the sliding material ( $\tilde{t}_h$ ) and the shear zone ( $\tilde{t}_{hs}$ ), defined as:

$$T_{lw}^e = (\tilde{t}_h \tilde{t}_{hs})^{-1} = \frac{GT^2}{\rho h h_s}. \quad (3.17)$$

Therefore, the coupled behavior of a creeping landslide inside the shear zone involves a number of controlling nondimensional parameters dictating its dynamics, including the diffusion time ( $T_{lc}^e$ ), the shear wave propagation time ( $T_{lw}^e$ ), the slope inclination ( $\theta$ ), and the elastoplastic properties encapsulated into the dynamic coefficients A and B.

### 3.3 Model performance

#### 3.3.1 Precipitation induced diffusion and elastic response

To explore the framework's ability to simulate landslide movements induced by precipitation, it is first tested with an artificial rainfall event (lasts for 30 days ( $T$ ) with a constant intensity ( $q$ ). While the analysis is purely illustrative, the range of model parameters is chosen on the basis of typical evidence available for landslide sites in the California Coastal Range. Hence, the rainfall intensity is set equal to the saturated permeability of sliding material ( $k_s^t$ ), here assumed to be  $3 \times 10^{-6}$  m/s (Keefer & Johnson, 1983). The storage coefficient ( $S_s$ ) is set to 0.26 (according to back calculated diffusivity around  $1.1 \times 10^{-5}$  m<sup>2</sup>/s from Handwerger, et al., 2019). Stiffness parameters for this manuscript are taken as: oedometric modulus  $E_{oed} = 5$  MPa, and shear modulus  $G = 2$  MPa based on soil composition (Keefer & Johnson, 1983). The pore-water pressure change at the interface between sliding material and active shear zone ( $p_w^t$ ) can be computed numerically. The results are provided in Fig. 3a, which shows that the  $p_w^t$  increases monotonically after the wetting front approaches the top of shear zone (20 m) when  $\tilde{t}$  is around 0.3.

The computed  $p_w^t$  will then serve as the hydraulic boundary condition activating coupled behavior inside the deformable shear zone. Simulations are conducted for different values of  $T_{lc}^e$  (Eq. 3.16)

to examine its role on pore pressure diffusion processes within the shear zone. In this study,  $T_{lc}^e$  depends on the value of the hydraulic conductivity,  $k_s^e$ , as discussed in previous section.

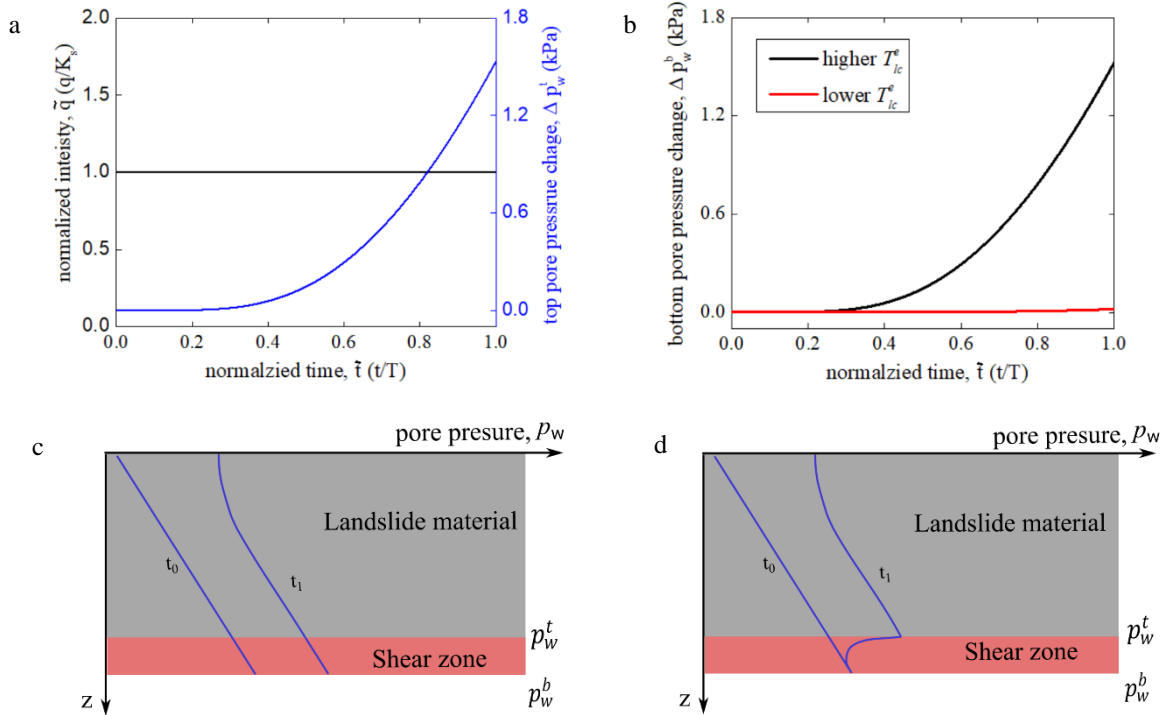


**Figure 3.3 Simulation of pore-water pressure transients caused by precipitation. a) Simulated pore-water pressure change at top of shear zone caused by a constant rainfall. b) Computational results of bottom shear zone pore-water pressure change, corresponding to different value of  $T_{lc}^e$ ; c & d) schematics of pore-water pressure distribution with higher and lower  $T_{lc}^e$ , where higher  $T_{lc}^e$  results from shear zone permeability ( $k^b$ )  $5.5 \times 10^{-7}$  m/s, and lower  $T_{lc}^e$  indicate  $k^b = 5.5 \times 10^{-12}$  m/s. Stiffness parameters are taken as: oedometric modulus  $E_{oed} = 5$  MPa, and shear modulus  $G = 2$  MPa.**

Fig. 3.3b shows that, when  $T_{lc}^e$  is relatively high, diffusion takes place rapidly within the shear zone, thus the hydraulic response ( $\Delta p_w^b$ ) at the bottom of the shear zone follows instantaneously the hydrologic forcing (i.e., the application of pore pressure changes,  $\Delta p_w^t$ , at the top of the shear zone). The pore pressure profile in this scenario is illustrated in Fig. 3.3c, which distributed in a hydrostatic form. On the contrary, pore-water pressure change can be delayed in the shear zone in the presence of low  $T_{lc}^e$  values. It is illustrated in Fig. 3.3d, where the basal pore pressure barely changes despite the application of a diffusive pressure forcing at the top of the deformable zone.

Since these tests are conducted for soil under elastic regime, infiltration does not involve approach of the yield surface and mobilization of the plastic resources of the shear zone. As an outcome, no sliding is generated. Under this scenario, the hydraulic diffusion process is governed solely by  $T_{ic}^e$ .

### 3.3.2 Behaviors under plastic regime

When the fluctuations of the effective stress state induced by infiltration are large enough to engage the frictional yield surface, plastic shear strain and consequent sliding occur. Separating from elastic regime, the material yield surface also starts to regulate the stress changes and corresponding deformation. For example, if material dilation angle ( $\psi$ ) is zero, no excess pore-water pressure can be induced. In this context, the pore-water pressure increase will be the same as triggered by water diffusion in elastic regime (Fig. 3.1b). Yet, under elastoplastic framework, the yield surface cannot be surpassed. The pore-water pressure increase will thus lead to stresses change along the yield surface towards the left bottom (Fig. 3.4a). As an outcome, strength loss (Eq. 3.3) and following runaway failure will be generated. Most notably, if non-zero plastic normal deformation is developed, excess pore-water pressure will be induced and regulate the slope dynamics. Dilative plastic deformation will generate negative excess pore-water pressure (Fig.3.4b), which is opposite to the pressure change triggered by flow infiltration (Fig. 3.1b). For shear zone material (with relatively small permeability), the pore-water pressure increase induced by infiltration can be overcome by the dilation generated negative excess pore-water pressure. As an outcome, the pore-water pressure increase triggered by infiltration will pause once the shear zone material is driven to the plastic regime. Dilative deformation generates self-regulating effects which constraint the pore-water pressure build-up. In contrast, contractive deformation would lead to an opposite outcome, by generating positive excess pore-water pressure and augmenting the infiltration effects (Fig. 3.4c), eventually leading to higher strength loss and runaway failure.

For our first landslide simulation in the plastic regime, we model landslide motion with dilative material. We apply a simple synthetic pore-water pressure event distributed normally with a magnitude of around 11 kPa over one year ( $T = 365$  days) at the top of the shear zone to represent pore-water pressure changes expected during a water cycle consisting of wet season and following dry season (Fig. 3.5). The  $T_{lc}^e$  ( $k^b = 5.5 \times 10^{-9}$  m/s) is set to cause nearly instantaneous pore-water pressure change (Fig. 3.5a). When  $\varphi = 20^\circ$ , the material yield surface is not approached and there is only elastic deformation. In contrast, a lower friction angle ( $\varphi = 17^\circ$ ) leads to plastic shearing (Fig. 3.5a & b, point B' to B'') under the same hydrological forcing.

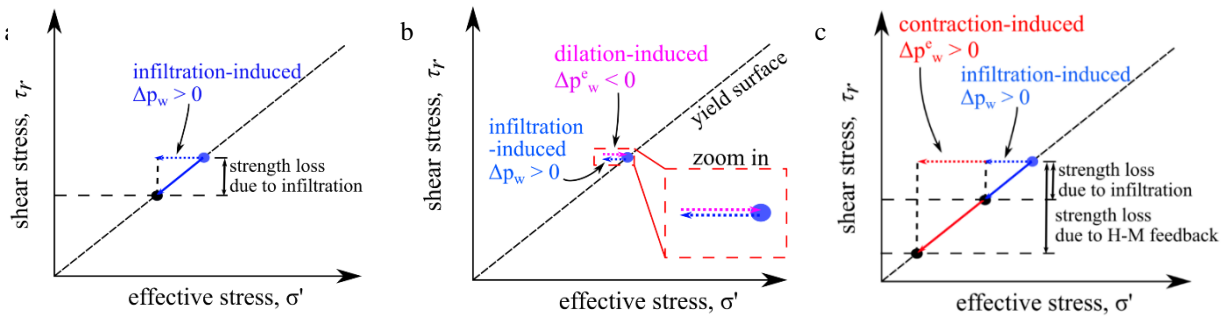


**Figure 3.4 Schematics of hydrological response generated by plastic normal strain. a) Stress change caused by hydrological forcing in plastic regime with nil normal plastic deformation. b) Dilative material generated self-regulating behavior. c) Contractive material induced self-feeding mechanisms.**

Fig 3.5a and 3.5b show that, for  $\varphi = 17^\circ$ , plasticity ensues when the imposed pore-water pressure at the top of the deformable zone is close to 8 kPa (i.e., point B', at  $\tilde{t} = 0.4$ ). Subsequently, plastic deformation begins to develop in both normal and tangential directions (Fig. 3.5b). Regulated by plastic dilation, negative excess pore-water pressure is generated. The self-regulating effect halts the growth of pore-water pressure and stops the landslide from accelerating further (Fig. 3.5f).

As the pore-water pressure applied at the top of the shear zone begins to drop and drives the material back into the elastic regime (point B'',  $\tilde{t} = 0.6$ ), the basal pore-water pressure decreases and there is a transition from plastic to elastic deformation. At the same time, sliding stops (Fig.

3.5b point B''), marking the end of the episodic development of negative excess pore-water pressure coupled with downslope sliding. For the case with  $\varphi = 20^\circ$  (Fig. 3.5 a, c, e), the whole process is in elastic regime, there is no sliding occurred, and no excess pore-water pressure will be induced. (Fig. 3.5b). These results confirm that sliding occurs only if precipitation mobilizes the inelastic resources of the shear zone material (Fig. 3.5b). Here, the pore-water pressure increase driven by infiltration is halted because of the plastic dilation induced negative excess pressure (Fig. 3.5d), which is different from the delayed pore-water pressure change in elastic domain (Fig 3.3d) induced by limited diffusivity. It also indicates that both the elastic and plastic deformation regulate the timescale of water diffusion. Most notably, our model shows (similar to other studies) that dilation in the plastic regime leads to self-regulated landslide motion.

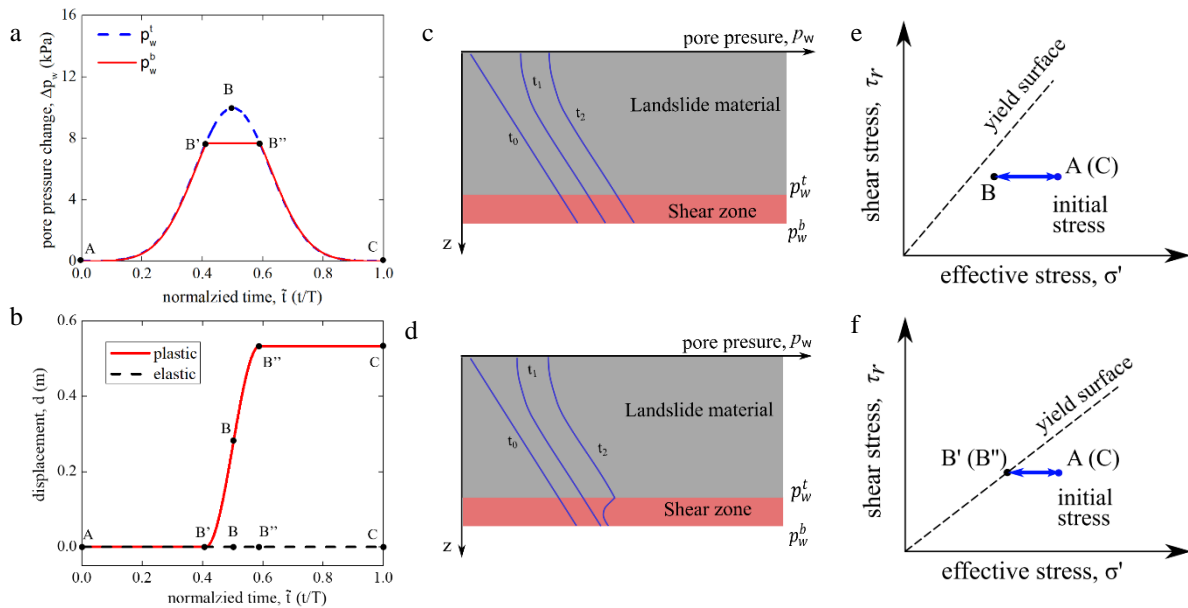


**Figure 3.5** Simulation of the hydro-mechanical response of an infinite slope subjected to imposed pore-water pressure change at the top of its shear zone. a) top shear zone pore-water pressure changes in one year, with the bottom response under both elastic and plastic regime. b) Downslope displacement, c & d) pore-water pressure profile when material is under elastic & plastic regime. e & f) Schematic of hydrological response in elastic and plastic regime. Synthetic slope tested here is assumed to be 7 m deep, inclination  $15^\circ$ , dilation angle  $\psi = 2^\circ$ .

### 3.3.3 Coupling effects

Plastic normal deformation in this study is governed by the dilation angle  $\psi$  (Eq. 16). To further investigate its effects, the same synthetic slope and pore-water pressure variation illustrated in Fig. 5 are tested with different values of  $\psi$  ( $5^\circ$ ,  $2^\circ$ , and  $0^\circ$ ), but equal friction angle ( $\varphi = 17^\circ$ ).

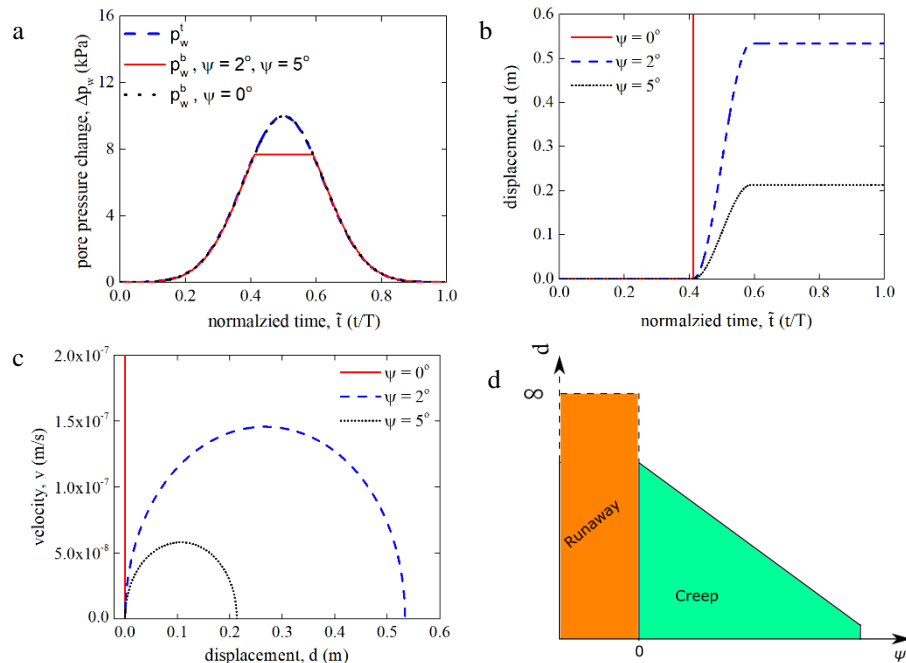


**Figure 3.6 Slope hydro-mechanical response corresponding to different dilative potential. a) pore-water pressure at the top and bottom of shear zone. b) Simulated displacement with different dilation angle, c) simulated velocity vs. displacement, d) the relationship of sliding velocity and dilation angle, with the condition for liquefaction.**

Fig. 3.6a shows that pore-water pressure time series at the bottom of the slope predicted for cases with dilative deformation (i.e., positive  $\psi$ ) coincide, thus leading in all cases to self-regulating effects. By contrast, these regulating effects vanish in the analyses conducted with  $\psi = 0^\circ$  and runaway failure occurs. The result also indicates that induced by self-regulating effect illustrated by Fig. 3.4b, for dilative materials the normal effective stress and pore-water pressure will stop changing in plastic regime. As an outcome, the pore-water pressure value will be constant and be independent of the dilation angle value in plastic regime. On the one hand, the shear zone

diffusivity is limited thus making the negative excess pore-water pressure driven by plastic dilation higher than the infiltration induced pore-water pressure increase. The pore-water pressure at yielding thus cannot keep increasing under infiltration. On the other hand, further decrease of the pore-water pressure will push the stress states back to elastic domain, at that moment the negative excess pore-water pressure no longer existed. Therefore, once the yield surface is approached, pore-water pressure will experience no further change. However, material with different dilation angle under the same amount of pore-water pressure change will induce different amount of plastic deformation. The higher the dilation angle, the smaller the plastic deformation, i.e., volume change and downslope sliding will be triggered. Fig. 3.6b illustrates that, for a dilation angle of  $5^\circ$ , the simulated sliding displacement is around 0.2 m. This movement more than doubles for  $\psi = 2^\circ$ , reaching more than 0.5 m. Hence, the higher the dilation angle, the stronger the self-regulating effects, thus resulting into lower overall sliding displacement.

Most notably, when  $\psi$  is  $0^\circ$ , no negative excess pressure can be induced to preclude the pore-water pressure increase, as illustrated by Fig. 3.4a. Then strength loss and corresponding high displacement (i.e., runaway acceleration) will be generated (Fig. 3.6a~3.6c). The same analysis can be conducted even for shear zone materials experiencing contraction (i.e.,  $\psi < 0$ ). This scenario mimics so-called liquefaction effects, i.e., self-feeding growth of excess pore-water pressure accompanied by loss of shearing resistance (Iverson, 2005; Iverson et al., 2015; Chen & Buscarnera, 2022). The sharp transition between these different landslide dynamic regimes is qualitatively illustrated in Fig. 3.6d. While the incorporation of multiple nonlinear constitutive laws is necessary to simulate the abrupt development of excess pore-water pressure and high mobility failure events such as liquefaction, it is beyond the scope of this paper, our synthetic results point out the crucial importance of accounting for potential approach of critical state

conditions and/or for stress-induced changes in volume change behavior if landslide models are to be used to distinguish stable episodic slip events from catastrophic runaway movements.

### *3.4 Case studies*

In this chapter, three landslide sites have been considered to test the proposed framework: Two Towers landslide (Schulz et al., 2018), Minor Creek landslide (Iverson & Major, 1987), and Mud Creek landslide (Handwerger et al., 2019). Their movement have been monitored using ground-based or remote sensing technologies. The Two Towers landslide hourly movement was measured from 11 November 2014 to 22 July 2017 using a biaxial tilt sensor (Schulz et al, 2018). Minor Creek landslide was monitored between 1982-1985 using ground-based tools including extensometer (Iverson 1987). Mud Creek landslide, central California Ranges, were monitored between 2015 and 2017 (Handwerger et al, 2013; 2019) through satellite interferometric synthetic aperture radar (InSAR). These cases display distinct trends of movement over time, thus allowing ideal benchmarks to verify the accuracy of the proposed framework.

#### *3.4.1 Parameter optimization method*

For the case studies in this paper, all model parameters were assessed by optimization procedures focusing on the identification of best fit values for  $k^b$  (shear zone permeability),  $\varphi$  (friction angle), and  $\psi$  (dilation angle). We used a grid search inverse method to optimize these parameters (Allmendinger, 1998). This method computes the objective function (OBJ) from initial guesses based on typical ranges of these parameters and then searches the minimum OBJ.

$$OBJ = \sum (d_o - d_s(k^b, \varphi, \psi))^2, \quad (19)$$

where  $d_o$  is observed displacement;  $d_s$  is simulated displacement. The parameters ( $k^b, \varphi, \psi$ ) lead to the minimum OBJ will be the optimized ones. Take an example of Two Towers landslide analysis (detail see the next section), we perform a grid search for  $\psi$  ranging between  $1^\circ$  to  $5^\circ$  (dilation angle for clayey material is limited, Vermeer and de Borst, 1984). OBJ values corresponding to  $2^\circ$  ( $\psi$ ) are shown as an example in Fig. 3.7. The analysis provides a narrow band of values (dark blue in Fig. 3.7) with relatively small OBJ values. Among them, the minimum value can be found. Optimized parameters are displayed in Table 1.

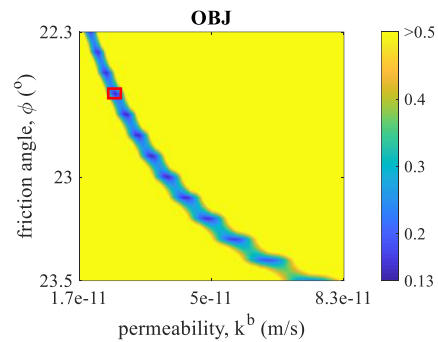


**Figure 3.7 Inverse analyses obtained OBJ values corresponding to friction angle and permeability when  $\psi=2^\circ$ , optimized parameter is indicated by the red polygon.**

### 3.4.2 Two Towers landslide

The Two Towers landslide (Fig. 1.2) is around 250 m long and averages about 40 m in width and 7 m in depth; with an average inclination of  $15^\circ$ . The groundwater head and landslide movement were monitored from November 2014 to July 2017 by Schulz et al (2018). Clay swelling was observed at the site. Although it is likely to have played a role in landslide dynamics, its role was not explicitly incorporated here; focus is placed instead on shear-induced volume change.

Through optimization process explained before, the model parameters can be optimized as displayed in Table 1. Fig. 3.8a shows the simulated pore-water pressure distribution at the bottom of the shear zone, characterized by delayed basal hydrological response compared to the forcing pore-water pressure imposed at the top of the shear zone ( $p_w^t$  and corresponding  $p_w^{sb}$ ). Most notably, Fig 3.8b shows that, although a mismatch exists between model and data (i.e., the simulated movement begins earlier than the observations and slightly underestimates the measured displacement in 2016 and 2017), the overall simulated trend is consistent with the monitoring data at the Two Towers landslide site.

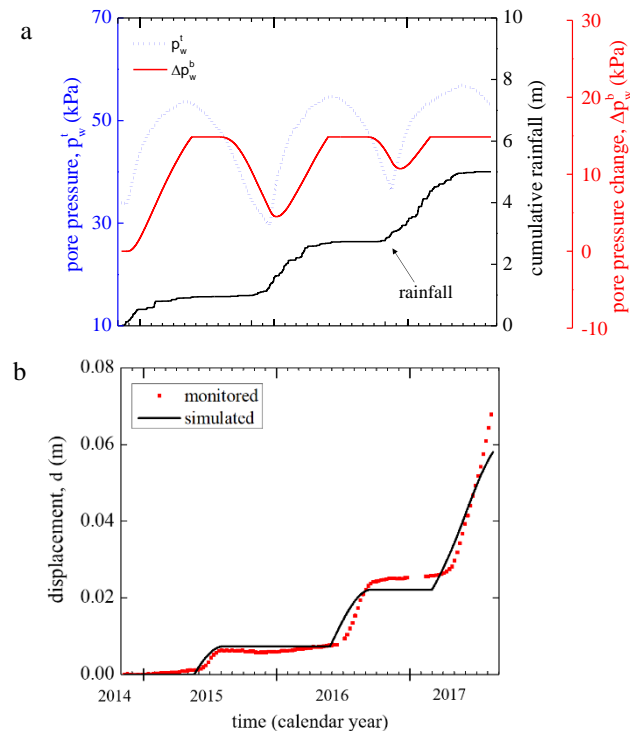


**Figure 3.8 Simulation of Two Towers landslide and relevant monitoring. a) Monitored pore-water pressure change at top of shear zone, optimized pore-water pressure distribution at the bottom of shear zone, and cumulative rainfall, b) computational displacement from optimization compared to the monitored value.**

### 3.4.3 Minor Creek landslide

Minor Creek landslide (Fig. 1.2), a compound, complex, slow-moving landslide, covers about 10 hectares in Redwood Creek drainage basin, northern CA Coast Ranges. Iverson & Major (1987)

provided three years detailed rainfall, groundwater and movement data (Fig. 3.9a and 3.9b) of this landslide from August 1982 to September 1985. The average slope angle is  $15^\circ$ ; the thickness of the landslide along its longitudinal axis is 6 m (Iverson, 1985).

Saturated permeability ( $k^t = 9 \times 10^{-7}$  m/s) and storage coefficient ( $S_s = 0.45$ ) of the sliding material can be determined using the monitored pore-water pressure data (Fig. 3.9a). The diffusivity ( $2 \times 10^{-6}$  m<sup>2</sup>/s) is similar to the value back calculated by Iverson and Major (1987). Then, similar to our Two Towers landslide simulation, parameter optimization is used to constrain the mechanical parameters of the shear zone material and capture the observed displacement.

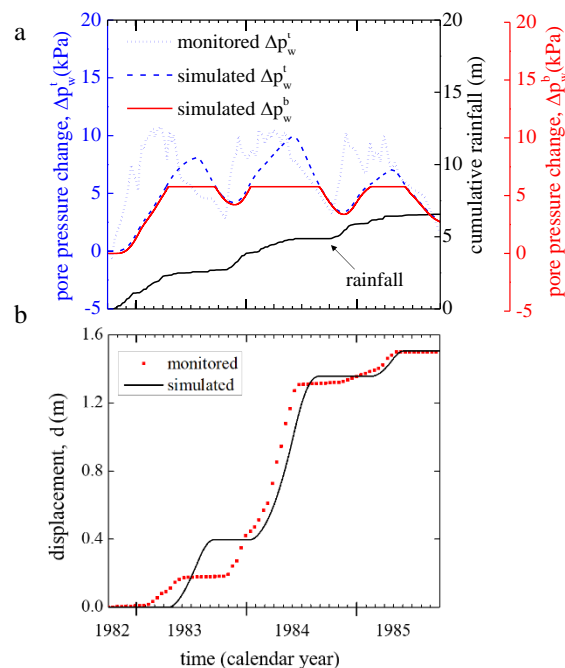


**Figure 3.9 Simulated and monitored hydrological and mechanical behaviors at the Minor Creek landslide site. a) monitored and simulated pore-water pressure at top of the shear zone, simulated pore-water pressure at the base of the shear zone, and cumulative rainfall. b) Monitored and simulated displacement.**

Despite an overestimation of the time at which the movements are predicted to begin, the analysis results into a satisfactory match with the monitoring data. In agreement with prior interpretations by Iverson and Major (1987), our model indicates that the sliding behavior is governed by two

hydraulic factors: (i) the magnitude of the pore-water pressure at the top of the landslide shear zone (the higher the maximum value, the larger the potential for the shear zone to be driven into a plastic regime, thus initiating sliding); (ii) the duration of the plastic stage, during which large shear strain can be accumulated.

#### 3.4.4 *Mud Creek landslide*

Mud Creek landslide (Fig. 1.2), Central California Coast Ranges, is selected as another study site. The Mud Creek landslide displayed stable sliding for more than 8 years; however, it suddenly failed catastrophically on a dry day (May 20, 2017) following a prolonged period of heavy rainfall. This event has caused great damage to the California highway 1 and it has been extensively studied through a variety of hydrologic and hydromechanical models (Handwerger et al., 2019; Warrick, 2019) through InSAR before the catastrophic failure occurred..

Mud Creek is characterized by relatively steep terrain with an average slope angle around  $32^\circ$ . Its shear zone is estimated to be located at a depth of about 20 m (Handwerger et al., 2019). In this analysis, given the lack of site-specific hydraulic observations, the forcing pore water pressure ( $p_w^t$ ) is simulated by using as a reference the computations shown for the Minor Creek site as discussed in section 2.5.2. Similarly, as all cases studies examined here are located in the Franciscan Mélange, to consider the difference in depth of sliding (from 7 m of Minor Creek to 20 m of Mud Creek), the hydraulic parameters are rescaled ( $k_s^t = 3 \times 10^{-6}$  m/s and  $S_s = 0.14$ ) to generate a similar time history of  $p_w^t$ . Using these parameters, the pore pressure distribution of Mud Creek landslide can be computed as illustrated by Fig. 3.10a, where the local cumulative rainfall is also illustrated.

The optimization strategy discussed in the previous sections is also used for this case, leading to simulation of both basal pore-water pressure (Fig. 3.10a) and sliding movement (Fig. 3.10b). The

results are consistent with the InSAR observations prior to the catastrophic collapse. Notably, the optimized friction angle for Mud Creek is very high (about  $48^\circ$ ), which is an outcome of the steep (i.e., high initial stress ratio), deep seated slope and nearly fully saturated initial condition (leads to high pore-water pressure). In this context, the initial basal pore-water pressure is around 140 kPa, which is higher than typical conditions used in soil laboratory testing.

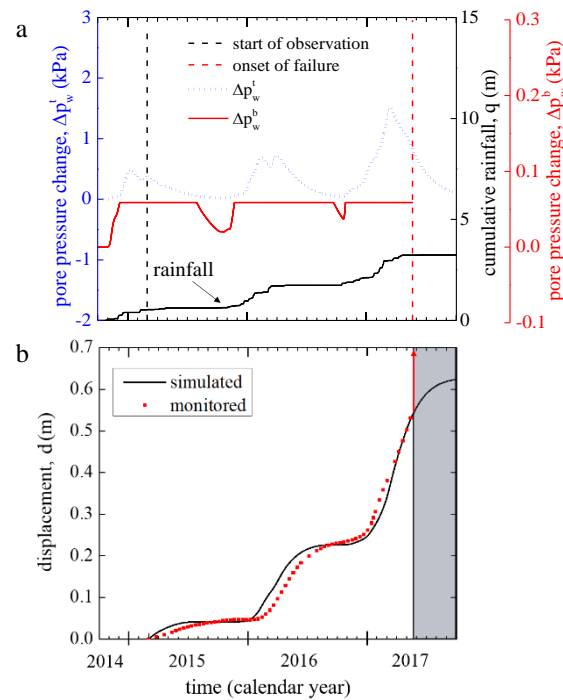


**Figure 3.10 Simulated and monitored hydrological and mechanical behaviors at the Mud Creek landslide site. a) Simulated pore-water pressure distribution at top and bottom of the shear zone and cumulative rainfall. b) Monitored and simulated displacement by the end of stable sliding. The left boundary of the shaded rectangle represents the occurrence of catastrophic failure.**

**Table 3.1. optimized parameters for each case study**

Model parameters	Two Tower	Minor Creek	Mud Creek
$k^b$ (m/s)	$2.7 \times 10^{-11}$	$3.3 \times 10^{-9}$	$6.4 \times 10^{-10}$
$\varphi$ ( $^\circ$ )	22.6	19.3	47.8
$\psi$ ( $^\circ$ )	2	2	1

The estimated the landslide velocity to be between 0.02 m/s and more than 1 m/s (according to Warrick et al., 2019, the post-failure accumulation zone extended at least 175 m) when failure occurred (indicated by the red arrow in Fig. 3.10b). This mobilization is clear signatures of a catastrophic failure characterized by velocity and acceleration far exceeding those representatives of episodic seasonal movements (within 1m/year). However, with a positive dilation angle, the model results will always predict self-regulating creep. As an outcome, if we extend the simulation beyond the failure point, deceleration will occur (Fig. 3.10b) in response to the decrease of pore-water pressure due to lack of rainfall forcing (Fig. 3.10a). It can be thus concluded that in order to capture runaway stages the model needs to possess vanishing dilative effects (Fig. 3.6d). Once again, while the constitutive law used in this paper to illustrate the characteristics of the model does not involve a gradual approach of critical state, this example makes readily apparent that the future incorporation of more advanced constitutive laws within the framework proposed here is highly beneficial for a comprehensive examination of the transition from stable episodic landslide motion to runaway failure.

### *3.5 Discussion*

In this chapter, a hydro-mechanical modeling framework is proposed to capture the dynamics of slow-moving landslides in response to rainfall infiltration. It enables the simulation of landslide creeping under self-regulated dilative effects and runaway failure when there is no negative excess pore-water pressure generated for non-dilative material (Fig. 3.6d). The model can be used to simulate different modes of slow-moving landslide movement triggered by precipitation. However, in current its form with a perfect plastic constitutive law, the transition from stable creep to runaway failure cannot be captured as illustrated in our case study of Mud Creek landslide. It thus encourages us to apply and develop more advanced constitutive laws, such as those used in a

critical state model (Roscoe et al., 1958) into account to simulate the catastrophic runaway acceleration.

The model has been used to simulate three landslides located in KJf and obtained satisfactory results. Among them, the Two Towers landslide has also been studied by Schulz et al (2018) using a limit equilibrium method. They computed the factor of safety of the Two Towers landslide incorporating a strength coefficient which is governed by the clay swelling. It has been shown that the clay swelling controlled the lag between the water level fluctuation and landslide activation. In this manuscript, our hydro-mechanical coupled method can be used to compute the displacement trend and obtain consistent results with the monitoring. Yet, some mismatch existed such as the simulated displacement always occurred earlier at each year and the magnitude of movement at the last two years are underpredicted. This indicates that taken clay swelling into account will improve our simulation results for Two Towers landslide, it also encourages us in our future study to take other hydro-mechanical effects such as clay swelling and unsaturated effects from vadose zone into account.

The Minor Creek landslide has also been studied by Iverson (2005) using a shear-induced dilation model. His simulation shown that a dilation angle ( $3^\circ$ ) would lead to a satisfactory sliding computation. Similarly, our simulation can capture the trend of movement of Minor Creek landslide. In addition, our methodology is able to take the inelasticity's effects on excess pore-water pressure growth into account when analyzing the hydro-mechanical coupling. It influences the model application in simulating active sliding and more importantly, the dynamics of liquified failure events (Rice, 1975; Chen and Buscarnera, 2021).

As discussed in Chapter 2, another widely used methodology under uncoupled framework to simulate slow-moving landslide behaviors is viscoplastic models (Van Asch et al., 2007; Angeli et al., 1996; Oberender and Puzrin, 2016). These types of models can be used ideally to capture creeping landslide movement under quasi-static framework. However, there are some issues existed in incorporating viscosity in landslide creeping analyses, such as: some earthen material viscosity is negligible (Schulz et al., 2018; Iverson 2020); large discrepancy can be found between viscosity parameters obtained from laboratory tests and real case back calculations (Angeli et al., 1996; Van Asch et al, 2007). In this chapter, proposed hydro-mechanical coupling framework can be used to interpret landslide creeping behaviors without incorporating earthen material viscosity. Meanwhile, it enables the simulation of runaway failure without abrupt external loading, thus can be regarded as an advanced method in capturing the slow-moving landslide dynamics.

### *3.6 Summary*

This chapter proposed a framework enabling the study of rainfall induced landslide dynamics, with the goal to decipher the interaction between precipitation, pore water pressure change, and inelastic deformation within the shear zone of active landslides. Two sequential diffusion processes are considered, one within a sliding block and another within an inelastically deformable basal shear zone. While the former is used to simulate hydraulic forcing on top of the shear zone, the latter enables explicit consideration of the inelasticity of the shear zone material, thus modulating both the timescales of sliding and pore water pressure diffusion through dedicated constitutive laws. Spatial condensation procedures are used to derive a set of coupled ordinary differential equations reflective of the landslide dynamics and accounting for the feedbacks transient water flow, inertial movement, and material inelastic properties. To illustrate the main characteristics of the proposed

framework, the model was linked with a perfectly plastic constitutive law enabling dilation and/or contraction of the shear zone material during sliding.

It was shown that the model can operate both under elastic and plastic regimes. By suppressing plastic effects, the framework is able to simulate delayed hydraulic forcing as a function of the diffusivity of both upper slope and elastic shear zone deformability parameters. Moreover, it was shown that sliding can be simulated if the hydraulic forcing drives the effective stress state within a plastic regime. Notably, the simulations indicate that the onset of plasticity alters dramatically the timescale of excess pore pressure response, and in turn the sliding velocity, through constitutive feedbacks modulating the effective diffusivity of the shear zone. Case studies indicate that distinct types of landslides behaviors can be simulated satisfactorily with reduced computational cost and a limited number of model parameters. Most notably, the framework enables the computation of catastrophic runout in the presence of either contractive shear zone material (liquefaction events) or critical state conditions (lack of dilation). In addition to its versatility in capturing evidence of episodic landslide sliding, the main advantage of the proposed framework is the virtually endless opportunities it offers to augment the constitutive description of the shear zone material and enable automatic convergence towards critical state conditions and thus gradual approach of catastrophic landslide mechanisms as a function of the varying rate and magnitude of hydraulic forcing, sliding velocity, and excess pore pressure change.

#### **4 SIMULATION OF CATASTROPHIC LANDSLIDE DYNAMICS BASED ON CRITICAL STATE PLASTICITY**

The catastrophic failure of moving landslides can cause extensive damage and even loss of life. Depending on the landslide type, such events can be preceded by long stages of stable slow motion (e.g., velocity  $< 1$  m/year). It is thus of great significance to understand the causes of their devastating acceleration and predict that under what scenarios slow creep movements can turn into rapid landslides failing catastrophically. With this motivation, this chapter examines the runaway dynamics of creeping landslides from the viewpoint of hydro-mechanical interactions mediated by an elastoplastic constitutive behavior. For this purpose, the coupled flow-deformation framework discussed in the previous chapter will be used as a starting point. Yet, at variance the constitutive description of plastic deformation within the landslide shear zone will be significantly enriched. In fact, as it was previously shown, the perfect plastic Mohr Coulomb model, widely used in standard geotechnical design and soil mechanics characterization, can satisfactorily capture the stable sliding behavior of slow-moving landslides in the presence of dilative effects encapsulated into a pre-calibrated dilation constant. However, this framework is unable to capture one of the cornerstones of soil mechanics, i.e., the close link between shear strength and volume often encapsulated into so-called stress dilatancy relationships (Rowe, 1962) and instrumental in the development of the most comprehensive and widely accepted theoretical standard for the interpretation of the results of highly controlled, instrumented laboratory tests of geomaterial deformation: the critical state theory (Casagrande 1936; Roscoe et al., 1958). In this chapter it is argued that unless critical state conditions are taken into account (i.e., unless the dependence of strength and current volume and their evolution towards a steady state at which both strength and porosity reach constant values is considered), it will not be possible to capture transitions from

slow sliding to runaway failure. The analyses shown in the remainder of this chapter are therefore aimed at taking these missing elements into account, by incorporating a critical state constitutive model into the previously proposed coupled hydro-mechanical framework. The selected model (Modified Cam Clay) and its performance in simulating the transition from stable sliding to catastrophic runaway acceleration is then examined. Followingly, a runaway index that can be used to numerically evaluate the evolving dynamics of a moving landslide is proposed. Most notably, the rationale here used to assess whether a slow-moving landslide can experience weakening and is eventually driven towards catastrophic failure is discussed in light of measurable pre-failure movement patterns. In the following, the proposed methodology is tested against selected case studies to validate that the fate of a landslide on the basis of its time-dependent movements induced by hydrologic forcing.

#### *4.1 Landslide catastrophic failures*

Catastrophic landslides take place worldwide and cause numerous fatalities (Hendron & Patton, 1985; Schuster et al., 2002; Runqiu, 2009; Haque et al., 2016; Stark and Hungr, 2014). For instance, the Vajont landslide, occurred on October 9, 1963, in Northern Italy, killed 1917 people (Hendron and Patton, 1985); the Oso landslide, occurred on March 22, 2014, near Oso, Washington, caused 43 fatalities (Wartman et al., 2016); an even more recent landslide event was reported in the area of Guizhou, China, in July 2019, causing about 42 fatalities (Li et al., 2019). It is normally observed that catastrophic failures possess velocity around or above 1m/s. Such peak movement rates, however, are often anticipated by much slower creep stages characterized by velocity within or around 1m/year (Voight, 1978). It is thus of great significance to predict the causes of such major acceleration in order to protect human lives and infrastructures.

With this goal in mind, numerous researchers have examined several factors which can contribute to catastrophic landslide acceleration. From a thermo-mechanical viewpoint, temperature change inside the landslide material during creep has been studied as a possible factor involved in the runaway dynamics of landslides. According to these studies, increased temperature can lead to growth of excess pore-water and consequent cushioning effects responsible for decreased strength in the shear zone (Romero and Molina, 1974; Anderson, 1980; Voight and Faust, 1982). The role of the temperature on water flow has also been studied, showing that it may contribute to a deterioration of the stability conditions (Vardoulakis (2002); Veveakis et al., (2016)). Given the complexity of testing and validating these arguments at either laboratory or field scale, other studies have explored the potential effect of purely mechanical processes often ignored in standard geomechanical analyses, such as progressive failure due to strain-softening or velocity weakening

(Alonso et al., 2016) and the consequent coalescence of discrete failure zones (Eberhardt et al., 2004).

Another widely studied factor which can lead to runaway failure is hydro-mechanical coupling. In fact, increased pore-water pressure generated by mechanical loading or hydrological forcing will lead to decreased of effective normal stress (Terzaghi, 1925). As an outcome, earthen materials experience loss of strength and slopes may begin to slide if static equilibrium along the tangential, downslope direction is no longer satisfied (Hutchinson, 1986). However, high mobility runaway failures suggest the presence of some source of strength loss both before and after the devastating acceleration (Voight, 1978). This argument has been one of the leading reasons to the mechanics of catastrophic landslides from the standpoint of material stability theories (Lade, 1997; Buscarnera and Whittle, 2013). Along similar lines, by taking flow-deformation coupling into account, Iverson (2005) studied the landslide dynamics by assigning a boundary condition to link volumetric changes within the shear zone with water infiltration, pore pressure transients, and the resulting downslope dynamics. In this study, a dilative shear zone would lead to stable sliding and contraction on the country will induce runaway failures. In this chapter, the landslide dynamics from creep sliding to catastrophic failure will be studied with a similar goal in mind, but with emphasis on the crucial role of the constitutive behavior of the plastically deforming material within the shear zone. For this reason, a critical state constitutive model will be used to regulate the timescale of pore pressure change and the related interaction between water flow and shear zone deformation by using the coupled framework discussed in Chapter 3.

#### *4.2 Coupled framework incorporating critical state plasticity*

In Chapter 3, a coupled flow-deformation framework was formulated and used to simulate the sliding dynamics of landslides with the widely used Mohr-Coulomb perfectly plastic constitutive law. However, the proposed framework enables the incorporation of any constitutive description of the inelastic behavior of shear zone materials, thus allowing the simulation of both stable sliding and catastrophic runaway failure when the rheological properties of the underlying constitutive law are enriched. Indeed, the use of a perfect plastic constitutive law (Mohr Coulomb) equipped with constant values of strength and volume change characteristics inevitably limits the ability of the model to capture transitions of the predicted landslide dynamics. In this section, a critical state constitutive law is used to suppress these limitations, with obvious consequences on the inferred time-dependent feedbacks of excess pore water pressure development and landslide acceleration.

##### *4.2.1 Limitations of landslide dynamics simulations based on perfect plasticity*

As explored by previous studies, catastrophic landslides are often anticipated by creep movements (Voight, 1978; Hendron and Patton, 1985; Wartman et al., 2016), which indicates that slow-moved landslides can suffer runaway acceleration when special conditions are met. Here, in order to test the capability of the proposed hydro-mechanical coupling framework to replicate a spontaneous increase in landslide velocity as an outcome of hydrologic forcing (pore-water pressure increased from 0 to 20 kPa then kept constant (Fig. 4.1a)) applied on the top of a synthetic landslide shear zone (parameters are described in Fig. 4.1 caption). This load is sufficient to bring the shear zone material into a plastic deformation regime and activate downslope movements. The computation is conducted using the perfectly plastic Mohr-Coulomb model (Eq. 3.15).

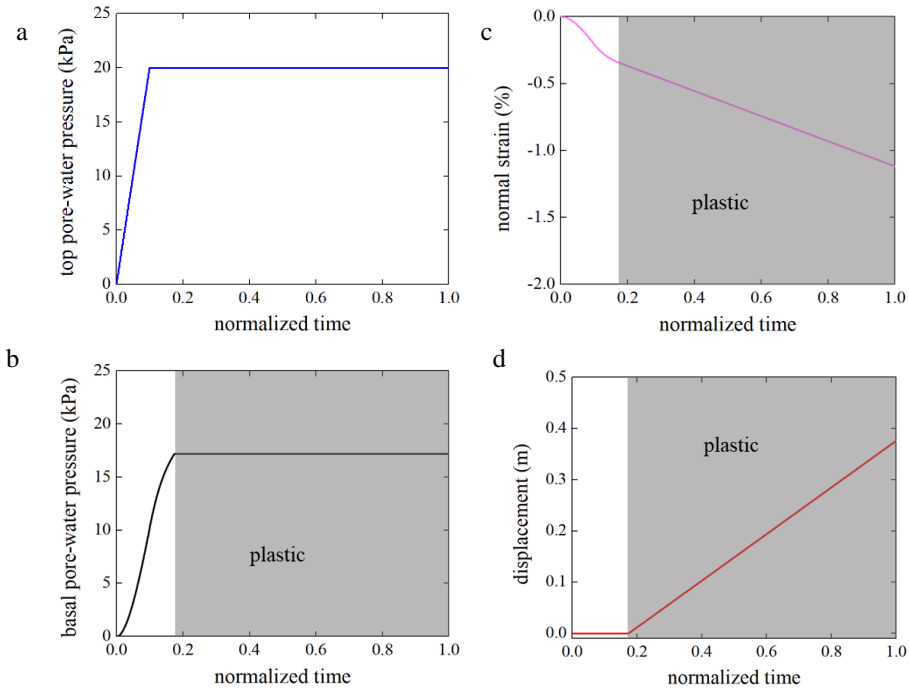


**Figure 4.1 Synthetic landslide response of pore-water pressure change applied on top of the shear zone by using the Mohr-Coulomb perfectly plastic model. a) Applied pore-water pressure. b) Pore-water pressure change within the basal shear zone. c) Induced normal strain. d) Generated landslide displacement; a shaded polygon indicates that the material has achieved a plastic deformation regime. For this synthetic landslide experiments the model parameters were chosen to resemble one of the study sites, Mud Creek landslide (Warrick et al., 2019; Handwerger et al., 2019), thus setting  $h = 20$  m,  $\theta = 32^\circ$ ,  $\gamma_{sat} = 21$  kN/m<sup>3</sup>,  $E_{oed} = 5$  Mpa,  $G = 2$  Mpa,  $\varphi = 36.1^\circ$ ,  $\psi = 1^\circ$ , and  $k_s^b = 1 \times 10^{-8}$  m/s.**

The results show that the basal pore pressure changes monotonically until the shear zone material is driven to plastic deformation domain (Fig. 4.1b); at when plastic dilation starts to develop (Fig. 4.1c). As an outcome, the increase of basal-pore water pressure is prevented under plastic domain because of dilation-induced feedbacks (Fig. 4.1b). Meanwhile, the plastic normal strain (Fig. 4.1c) is found to increase at constant rate because of the constant dilation angle assumed by the Mohr-Coulomb (MC) model. Thus, the displacement caused by plastic deformation along the direction tangential to the slope will also increase at a constant gradient (Fig. 4.1d). These trends are not reflective of catastrophic failure, but rather of a steady state motion driven by the imposed pore water pressure. In other words, the simulated landslide can be readily shown to reduce its velocity as soon as the forcing is removed (i.e., the mechanism is not self-feeding, but rather self-regulated).

For this case, a positive dilation angle is used. While as shown before, a negative dilation angle (i.e., a marker of loose packing functional to replicate plastic compaction during shear) or even vanishing dilation (i.e., a condition of plastic shear at constant volume, commonly referred to as critical state) can induce catastrophic runaway failure. It is thus interesting to explore how improvements of the constitutive framework can modify the resulting predictions. For example, decades of experimental research based on soil testing have extensively demonstrated that the strength and deformation properties of soil evolve nonlinearly during deformation (Fig. 4.2).

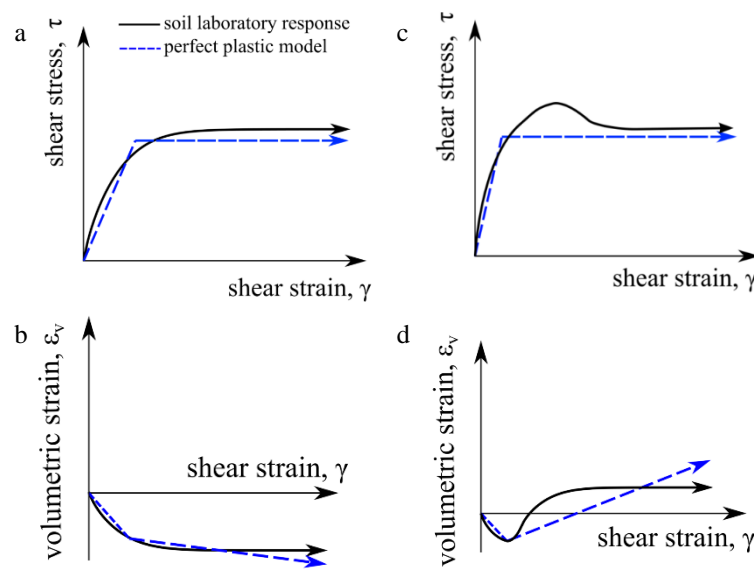


**Figure 4.2 Schematic of typical stress strain relations representing soil behavior during shear experiments compared against predictions of a perfect plastic model. a) shear stress vs. shear strain for strain-hardening response (e.g., loose sand under drained loading or normally consolidated clay). b) normal strain vs. shear strain. c) shear stress vs. shear strain for strain-softening response (e.g., dense sand or over-consolidated clay). d) normal strain vs. shear strain.**

Fig. 4.2 shows schematically the stress and strain behaviors of typical earthen materials subjected to shearing (Muir Wood, 1990). Perfect plastic models (such as MC) will generate sharp transition from an elastic to a plastic regime, which emerges when the yield stress ratio  $\eta_y$  is reached and involves constant strength (Fig. 4.2a & 4.2c). By contrast, laboratory tests indicate that soft soils

(e.g., loose sand or normally consolidated clay) tend to experience a smooth development of plastic strain since the early stages of loading, up until the point of failure, when the sustained shear stress reaches a maximum, constant value. During this process, the material experiences a loss of volume (i.e., it contracts during shear) until the failure point; by contrast, MC model (Fig. 4.2b) predicts constant rate of dilation when material is under plastic domain. On the contrary, stiff geomaterials (e.g., dense sand or over-consolidated clay) tend to be characterized by a peak shearing resistance that decays upon further deformation until achieving a lower, fully softened, strength level (Fig. 4.2c). During this process, stiff geomaterials typically exhibit volume increase (i.e., dilation) until the failure point; however, perfect plastic model (MC) obtains constant rate of dilation (Fig. 4.2d) once the material is under plastic regime. Notably, in either scenario the volume change properties of the material (and, hence, the tangent dilation or contraction) that evolve gradually until the ultimate conditions at a vanishing point (i.e., no further volume change) cannot be captured by perfect plastic models.

Simulating such trends is significant, especially in a context in which the shearing resistance of the shear zone material is modulated by substantial, inelastic, feedback controlled by the tendency of the shear zone material to dilate, and thus able to modulate its strength evolution in conjunction with strain-hardening and/or strain-softening feedbacks. From a mechanics standpoint, these aspects are likely to influence the transition from stable sliding to catastrophic failure known to occur during catastrophic landslide events (Voight, 1978). In this scenario, a selection of constitutive models that would take these missing elements into account is needed. Motivated by this, critical state models (Muir Wood, 1990) will be used hereafter to simulate the stable sliding and catastrophic acceleration.

#### 4.2.2 Coupled analyses based on the Modified Cam Clay plasticity model

Here, Modified Cam Clay (MCC) model (Roscoe and Burland, 1968) is used by virtue of its simplicity and ability to take critical state phenomena into account. Standard MCC is usually defined in the so-called p-q invariant space typical of triaxial testing (Wood, 2004). In this thesis, the analytical expression of such classic model is used to remap the core idea of MCC into the stress space that is relevant for the downslope landslide dynamics, i.e., based on normal effective stress and shear stress tangential to the considered infinite slope. This representation involves a classic elliptic yield surface geometry, and it is given below:

$$f = \tau^2 + m^2 \sigma' (\sigma' - \sigma_c), \quad (4.1)$$

where  $m$  is a shape parameter of the yield surface (it marks the stress ratio at the top of the surface),  $\sigma_c$  is the internal variable which bounds the size of yield surface (commonly referred to as pre-consolidation pressure, in that it encapsulates the past consolidation history of the material). As displayed in Fig. 4.3a by the shaded area, any stress state located inside the yield surface underpins elastic deformation. Upon loading, the stress state can change by implying a departure from the elastic regime. In this case, the yield surface is reached instantaneously for normal-consolidated (hard) clay (Fig. 4.3b), by contrast after an elastic shearing for over-consolidated (soft) clay. At variance with perfectly plastic models, MCC involves so-called hardening/softening feedbacks (Fig. 4.3c & 4.3d), i.e., it implies the evolution of the shear stress, plastic strains in both shear and normal direction, and internal variable,  $\sigma_c$ . According to a pre-defined hardening rule,  $\sigma_c$  is determined as follows:

$$d\sigma_c = \frac{\sigma_c}{B_p} d\varepsilon^p. \quad (4.2)$$

The parameter  $B_p$  in the above equation is a hardening constant quantifying the yield surface evolution upon plastic loading. Eq 4.2 assumes that the yield surface development is dependent on the plastic normal strain, thus implying that hardening capabilities vanish when the material exhibits plastic shear at constant volume (i.e., critical state, Fig. 4.3d). As in all standard plasticity models, the plastic strain rate can be determined in accordance with a plastic potential ( $g$ ), which for Modified Cam Clay can be labeled by the symbol  $g$  and expressed as:

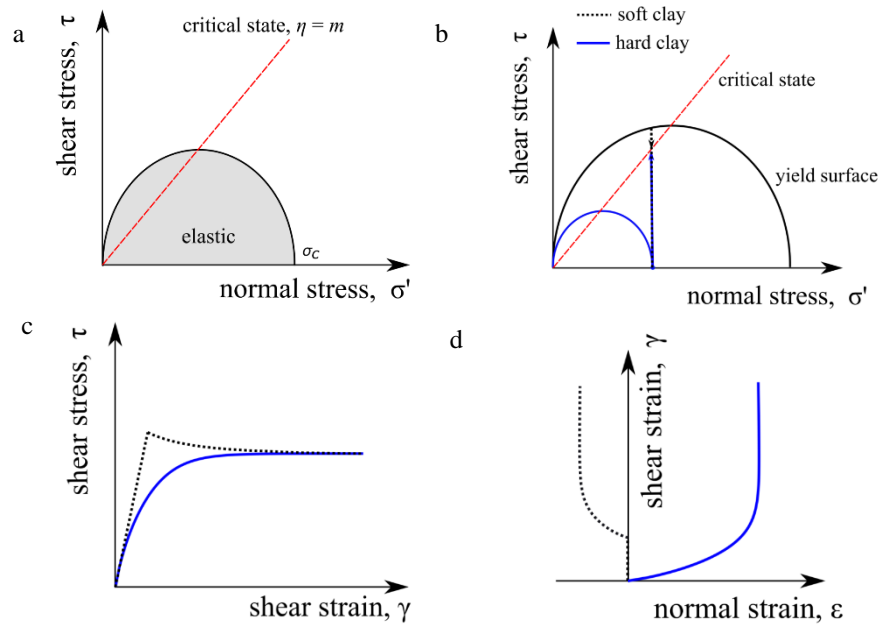


**Figure 4.3 Schematic of stress, strain response under shearing corresponding to the MCC model. In this schematic the multi-axial stress state is neglected. a) Graphical representation of yield surface and corresponding elastic domain. b) Stress path under strain-controlled shearing and initial yield surface for both soft clay (over-consolidated) and hard clay (normal consolidated). c) relation between shear stress and shear strain. d) relation between shear strain and normal strain.**

$$g = \tau^2 + M^2 \sigma' (\sigma' - \sigma_c). \quad (4.3)$$

Where  $M$  is the critical state stress ratio marking lack of volume change upon shearing. For the standard case of associated flow rule (i.e., coincidence between yield surface and plastic potential,  $f = g$ ) as assumed in this study,  $M = m$ . By inserting these constitutive functions into the sliding

consolidation governing equations (Eq. 3.15), the coupled flow-deformation dynamics based on MCC can be written as follows:

$$\begin{aligned} \dot{p}_w^b &= A_{11}(p_w^b - p_w^t) + A_{12}v \\ \dot{v} &= A_{21}(p_w^b - p_w^t) + A_{22}v \end{aligned} \quad (4.4)$$

where the dynamic coefficients  $A_{11} \sim A_{22}$  are

$$\begin{aligned} A_{11} &= -\frac{k_s^s}{\gamma_w} \frac{2E_{oed}}{h_s^2 \cos^2 \theta} \frac{\sigma' m^2 \frac{P_c}{B_p} \sigma'(m^2 - \eta^2) + G4\tau^2}{\sigma' m^2 \frac{P_c}{B_p} \sigma'(m^2 - \eta^2) + \sigma'(m^2 - \eta^2) * E_{oed} * \sigma'(m^2 - \eta^2) + G4\tau^2} \\ A_{12} &= \frac{\sigma'(m^2 - \eta^2) * E_{oed} * \sigma'(m^2 - \eta^2)}{\sigma' m^2 \frac{P_c}{B_p} \sigma'(m^2 - \eta^2) + \sigma'(m^2 - \eta^2) * E_{oed} * \sigma'(m^2 - \eta^2) + G4\tau^2} \frac{2\eta}{m^2 - \eta^2} \frac{G}{h_s} \\ A_{21} &= \frac{k_s^s}{\gamma_w} \frac{2E_{oed}}{h_s^2 \cos^2 \theta} \frac{1}{\rho h} \frac{G4\tau^2}{\sigma' m^2 \frac{P_c}{B_p} \sigma'(m^2 - \eta^2) + \sigma'(m^2 - \eta^2) * E_{oed} * \sigma'(m^2 - \eta^2) + G4\tau^2} \frac{m^2 - \eta^2}{2\eta} \\ A_{22} &= -\frac{1}{\rho h} \frac{\sigma' m^2 \frac{P_c}{B_p} \sigma'(m^2 - \eta^2) + \sigma'(m^2 - \eta^2) * E_{oed} * \sigma'(m^2 - \eta^2)}{\sigma' m^2 \frac{P_c}{B_p} \sigma'(m^2 - \eta^2) + \sigma'(m^2 - \eta^2) * E_{oed} * \sigma'(m^2 - \eta^2) + G4\tau^2} \frac{G}{h_s} \end{aligned} \quad (4.5)$$

Using Eq. 4.4, the hydro-mechanical response triggered by hydrological forcing (induced by rainfall) can be computed. The top pore-water pressure change displayed in Fig. 4.1a will be used again here to test a similar synthetic slope characterized by a shear zone deformation controlled by MCC. In this scenario, the induced stress path will be as depicted in Fig. 4.4a in a form that normal effective stress decrease in elastic domain and increase when material entering plastic regime. And the induced normal strain rate is no longer constant (Fig. 4.4c). In addition, the basal pore-water pressure decreases gradually until critical state, when its evolution is halted (Fig. 4.4b gray shaded area). There are two factors that can contribute to this response: first, the normal deformation is dilative, thus preventing pore-water pressure increase; second, the dilative strain

leads to softening, and hence to contraction of the yield surface and consequent strength loss (Eq. 4.2). As an outcome, the effective normal stress increases in response to the decreased pore-water pressure. Meanwhile, following the emergence of plastic deformation, sliding starts to develop (Fig. 4.4 c & 4.4d, where 4.4d is a zoomed in image for 4.4c, to better visualize the sliding behavior before and at critical state). At the point when critical state is reached, no further plastic dilation occurs (Fig. 4.4a normal strain keeps a constant value) and excessive displacement starts to develop. Fig. 4.4d shows clearly that the slope transits from stable sliding, under plastic regime, to runaway failure, when critical state is approached. On such basis, the failure mechanism and instability analyses will be discussed in the following section.

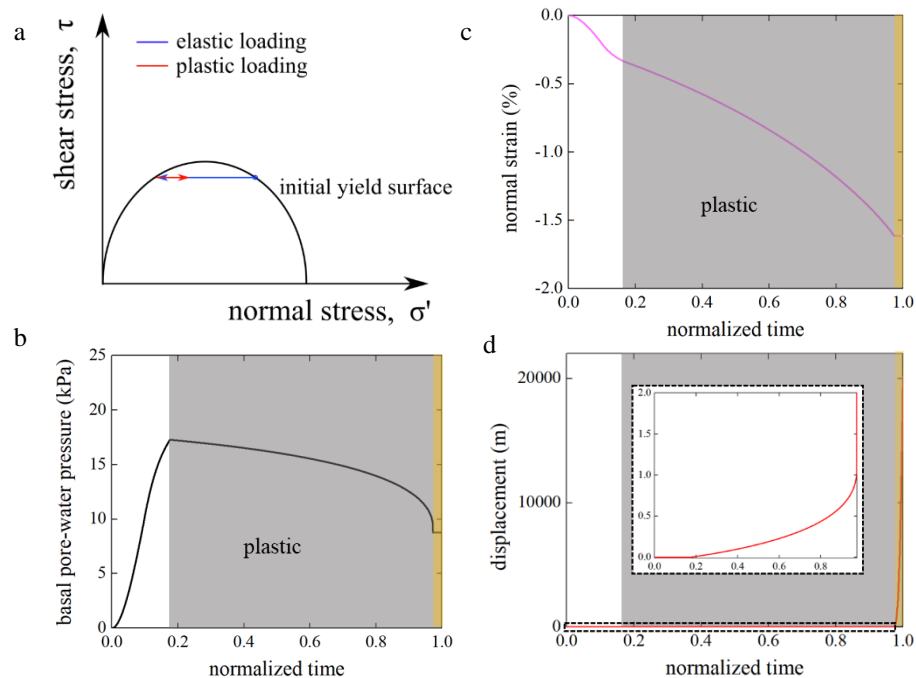


**Figure 4.4 Synthetic landslide response of pore-water pressure change applied on top of the shear zone by using Modified Cam Clay model. a) Stress path upon applied hydrological forcing in elastic and plastic domain sequentially. b) Basal shear zone hydrological response in pore-water pressure change. c) induced normal strain. d) Landslide displacement, the inset shows the zoomed in displacement at the initiation of runaway failure. Shaded polygon indicate material enter plastic regime; the yellow polygon marks the entering of critical state. Total time is 20 days, for this synthetic landslide experiments the model parameters were the same as illustrated by Figure 4.1 caption, except  $B_p = 30$  and  $m = 0.7$ , (this  $m$  value leads to the similar yield stress ratio.**

### *4.3 Simulation of catastrophic failure*

One of the most significant goals for this chapter is to determine whether a slow-moving landslide will fail catastrophically. To achieve this goal, a crucial question is: how can we detect based on its slow creeping regime if a slow-moved landslide is driven closer to a runaway failure? To answer this question, in this section the mechanisms that lead to runaway acceleration are explored. Subsequently, an index that can be used to assess the stability of the landslide deformation process will be proposed.

#### *4.3.1 Failure mechanism*

In order to understand what drives a slow-moving landslide to runaway failure, the previous case of runaway acceleration (Fig. 4.4) is explored in multiple steps (labeled as A, B, and C in Fig. 4.5). Stage A indicates the initial stresses determined from the components of the landslide self-weight and initial hydrologic conditions; stage B illustrates the entrance into a plastic domain; stage C depicts the approach of critical state. From A to B (Fig. 4.5a & 4.5b), is the elastic wetting periods, during which the basal pore-water pressure change is governed by linear diffusion with constant diffusivity (Fig. 4.5e) and no displacement is triggered (Fig. 4.5f), in that the system undergoes no shear stress variation. Meanwhile, normal strain is developed with dilative effects (volume increase) as an outcome of decreased effective normal strain (Fig. 4.5d).

When the stress state is driven into the plastic domain (Stage B), plastic shearing begins (tangential downslope sliding displayed in Fig. 4.5f). In the normal direction, dilative strain is induced (as shown in Fig. 4.5d). In the meantime, the basal pore pressure starts to decrease (Fig. 4.5e) as an outcome of dilation and strain-softening. At stage C the material reaches critical state, thus implying lack of volume change (zero normal strain rate) as shown in Fig. 4.5d. In this scenario,

wetting-induced pore-water pressure growth can no longer be dissipated, which leads to excessive displacement (Fig. 4.5f) and constant basal pore-water pressure (Fig. 4.5e).

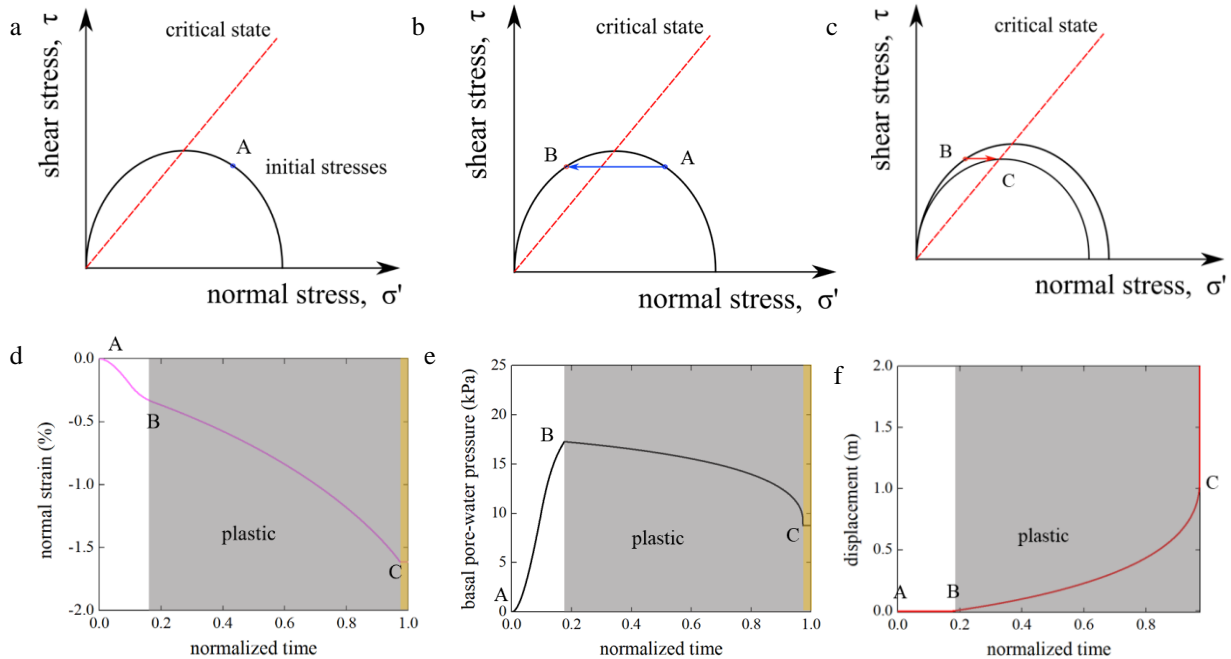


**Figure 4.5 Schematic of stress path, yield surface evolution, and deformation response due to hydrological forcing. a-c) variation of stress status and yield surface triggered by wetting signal displayed in Fig 4.1a at different stages (A, B, and C). d) Normal strain change, e) basal pore-water pressure, f) landslide displacement.**

Therefore, the slope will be unstable when the stress path approaches the critical state. In other words, upon wetting, when the plastic normal strain induced by the yield surface contraction drives the material stress state to critical state, failure occurs.

#### 4.3.2 Self-regulating index

On such basis, an index that can be used to evaluate slope stability against runaway failure can be devised. For this purpose, here the analytics of yield surface evolution under plastic wetting. As displayed in Fig. 4.6a,  $\eta_p$  represents the peak stress ratio ( $\tau/\sigma'$ ), which constraints by the yield surface and only changes when the yield surface evolves. It is known that any elastic loading triggering from or resulting in stress path inside the yield surface generates only reversible

deformation and causes no yield surface change. While, as illustrated by Fig. 4.6b, a plastic stage caused by pore water pressure increase can cause the yield surface to contract and reduce the peak stress ratio from  $\eta_p^1$  to  $\eta_p^2$ . When  $\eta_p$  reaches the critical state threshold,  $M$ , acceleration occurs, marking the onset of unstable conditions. It represents the fading of self-regulating effects and following runaway failure. Under this circumstance, the safety of a slope can be encapsulated in the following self-regulating index:

$$A = \eta_p/M, \quad (4.6)$$

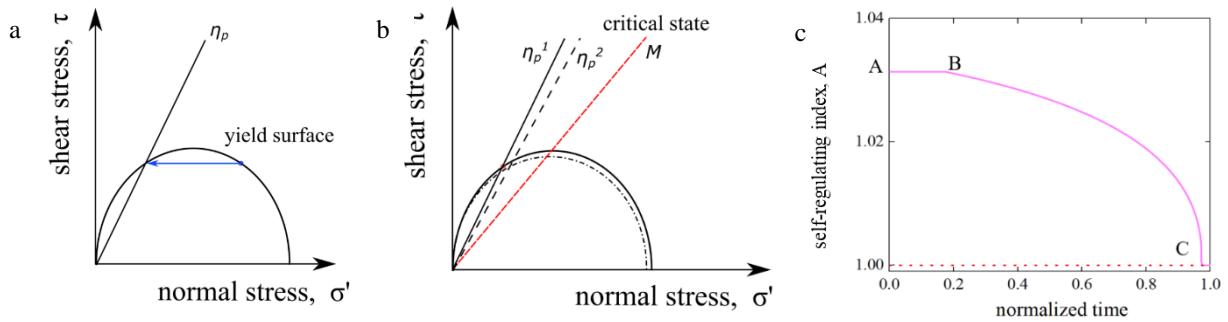


**Figure 4.6 Formulation of self-regulating index. a) schematic of rainfall infiltration induced hydrological forcing in elastic domain and corresponding  $\eta_p$ . b) The yield surface and  $\eta_p$  evolution under wetting. c) Tracking of self-regulating index during the simulation illustrated in Fig. 4.5.**

where failure will occur when  $A = 1$ . The higher the value of  $A$ , the further the stress state is from critical state; which leads to a more stable slope. And the value of  $\eta_p$  can be computed from:

$$\eta_p = \frac{2\tau_0}{\sigma_c - \sqrt{\sigma_c^2 - 4\tau_0^2/m^2}}. \quad (4.7)$$

Where the internal variable,  $\sigma_c$ , is computed directly from the governing equations (Eq. 4.4). To be specific, at each time the increment of internal variable can be solved by

$$\dot{\sigma}_c = \frac{\sigma_c (\sigma' (m^2 - \eta^2) P_w + 2\tau G \frac{v}{h_s}) \sigma' (m^2 - \eta^2)}{B_p \sigma' m^2 \frac{P_c}{B_p} \sigma' (m^2 - \eta^2) + G4\tau^2}. \quad (4.8)$$

It is therefore possible to track the value of instability index  $A$  during a simulation. Fig. 4.6b shows that during the pre-yielding stage of rainfall forcing  $A$  is constant until stage B, in that no change of  $\eta_p$  can be induced.  $A$  then starts to decrease when the material is driven into the plastic regime and approaches the threshold value  $A=1$  when critical state is reached. This analysis therefore indicates that the proposed index can be used to explore the dynamics of a slow-moving landslide. On such basis, the following subsection will focus on assessing the progression of the potential for runaway conditions in a moving landslide based on measurable creep movements.

#### *4.3.3 Simulation of the evolving landslide dynamics in response to successive rainfall cycles*

To examine the questions asked in the previous sections, here the proposed sliding consolidation model is used in conjunction with five cycles of artificial rainfall events sequentially imposed on a synthetic landslide (Fig. 4.7). Each of the cycles consists of a period of constant rainfall, with intensity equal to half of the saturated permeability, and a following stage with no imposed rainfall mimicking a dry period during which the system is not forced hydrologically and may deform only as a function of delayed hydro-mechanical feedbacks mediated by the shear zone inelasticity (Fig. 4.7a). The example simulation is conducted to replicate sequential wet and dry seasons observed in the California Coast Ranges (Corominas, 2000), where the case studies selected for this thesis are located. Using the hydrological model explained in section 3.2.1, the pore-water pressure at top of the landslide shear zone can be computed based on a diffusion model (Fig. 4.7a). These trends qualitatively represent the cyclic pore-water pressure time history inside slopes of the California Coast Ranges (Iverson and Major, 1987; Schulz et al., 2018; Finnegan et al., 2021).

Under this hydraulic loading, the hardening parameter  $B_p$  determines the rate of yield surface evolution, as well as how  $\eta_p$  moves towards critical state. Here, three values of  $B_p$  (labeled as

stable (S), Medium (M) and Weak (W), Fig. 4.7 caption) for the synthetic landslide are tested to link the observable hydro-mechanical behaviors to different material weakening extent. From Eq. 4.2, the higher the value of  $B_p$ , the smaller the yield surface will evolve under plastic loading, i.e., the less weakening potential the material possesses. In other words, the slope will be more stable upon wetting with a higher value of  $B_p$ . With the applied hydraulic loading, as displayed in Fig 4.7b, material W undergoes higher pore pressure dissipation under plastic wetting, while material S barely experience this change. The self-regulating index can also be computed (Fig. 4.7c) during the whole wetting process. It shows that index  $A$  for material W experiences the largest decrease (from around 1.15 at the beginning to slightly above 1.1 by the end). Meanwhile  $A$  barely changes for material S, and material M experiences an intermediate change of  $A$  from 1.15 to around 1.13.

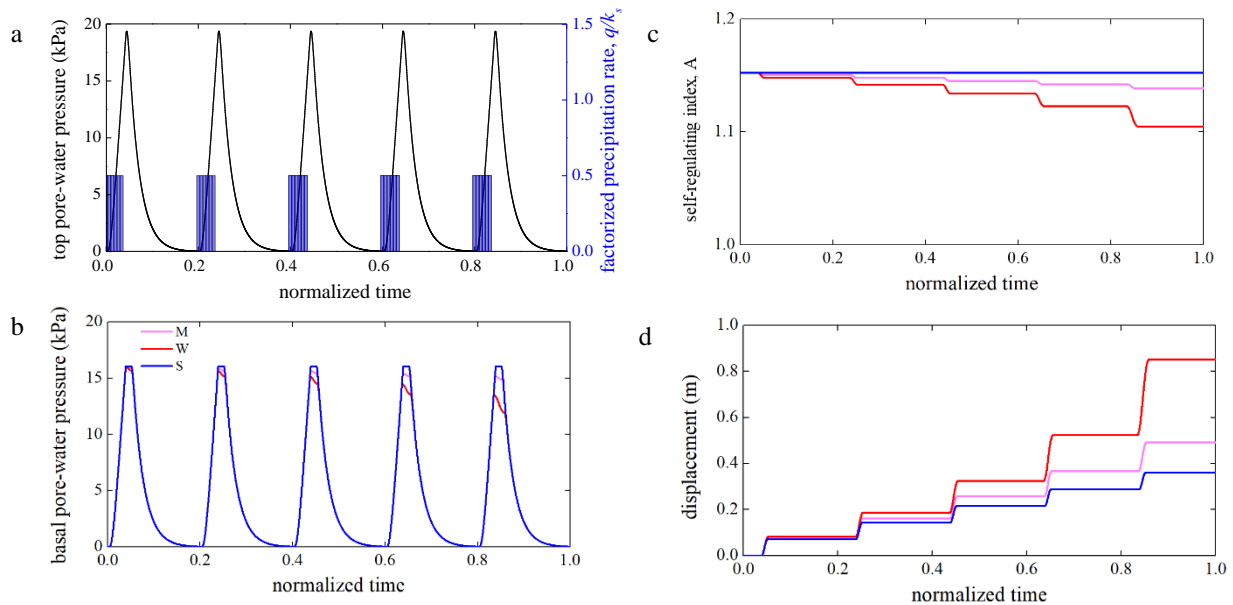


**Figure 4.7 Simulated landslide response after five sequential synthetic rainfall events. a) rainfall events applied at the landslide surface and induced pore-water pressure at the top of the shear zone. b) Basal shear zone pore-water pressure changes for each material deformation scenario (S indicates stable, W indicates weak, M indicates medium). c) Computed self-regulating index, d) generated displacement. Each water cycle's total duration is 30 days, for this synthetic landslide experiments the model parameters were chosen to resemble the Two Towers landslide study site (Schulz et al., 2018), thus setting  $h = 7$  m,  $\theta = 15^\circ$ ,  $\gamma_{sat} = 21$  kN/m<sup>3</sup>,  $m = 0.34$ ,  $k_s^s = 5 \times 10^{-8}$  m/s, and The hardening parameter  $B_p$  for material S, M, and W equals to 1E6, 14, and 7 respectively.**

Most notably, the wetting induced stable sliding displacement (Fig. 4.7d) shows that the relative stable material (S) undergoes almost the same magnitude of movement (slightly below 0.08 m) after each hydraulic cycle. While the weak material (W), mobilized around 0.3m under the last hydraulic cycle (around four times higher compared with the response after the first hydraulic cycle). This result indicates that under cycles of the same magnitude, if a slope is driven towards failure and the material is weakening, more displacement will be generated at later cycles. Although cycles of hydraulic forcing with the same intensity and duration are not common, these simulation results indicate that the magnitude of creep movement can imply whether a slope is driven closer to runaway failure.

#### *4.3.4 Comparison with landslide movement measurement*

To examine the same questions from the behaviors of real landslides, the trend of movements and hydrological forcing of several cases and relevant simulations are explored here. Fig. 4.8 shows ground-based monitoring of the Minor Creek landslide from 1982 to 1985 by Iverson and Major (1987). It was reported that when the water level passed a specific threshold plotted in Fig. 4.8, landslide movements would mobilize. Although water level had similar magnitude season after season, during the second year of observation (1982) the duration at which the water level was sufficiently high to induce slope movement was monitored to be longer (as indicated by the shaded polygon in Fig. 4.8). As stressed by Iverson and Major (1987), this effect led to larger displacements during that year. In fact, the higher magnitude of movement still falls in the range of slow-moved type of landslides (Hungr, 2014).

Based on these data, the synthetic landslide example shown before can be repeated with reference to three bell-shape cycles of pore-water pressure change with the similar magnitude, but with different duration as displayed in Fig. 4.9a (i.e., the second cycle possess longer duration, when

the slope is activated, thus mimicking the hydraulic forcing of the abovementioned Minor Creek event). In this case two materials (W and S in Fig. 4.7) are used to represent stable and weak scenarios for the shear zone material. The results show that if the material is relatively stable under cycles of wetting, the basal pore-water pressure and the self-regulating index barely change (Fig. 4.9b & 4.9c). Meanwhile, the displacement triggered by the first and third hydraulic cycle are the same (around 0.07m from Fig. 4.9d). On the contrary, for a relatively weak material,  $A$  decreases from around 1.15 to 1.12. Significantly, for the weakening material, larger displacement will be triggered by the last hydraulic cycle (around 0.2 m) although the wetting events for the first and third cycles are the same (Fig. 4.9a).

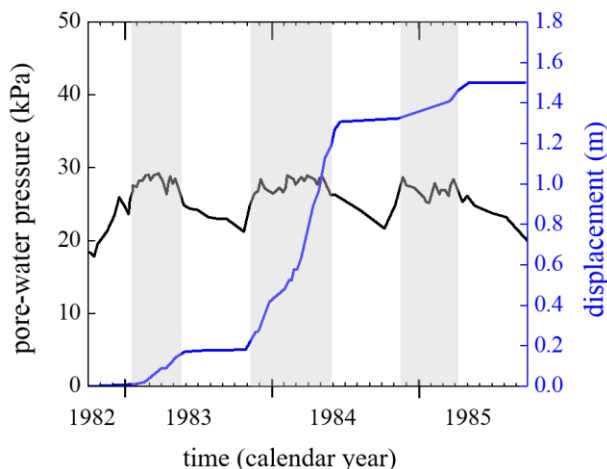


**Figure 4.8** Ground-based monitored water level and displacement of the Minor Creek landslide from 1982 to 1985. shaded bands indicate the periods during which the water level was above a triggering threshold, thus inducing landslide mobilization (Figure from Iverson and Major, 1987).

This example can help us explain the sliding mechanism observed at Minor Creek as a stable event.

Fig. 4.8 shows the duration of landslide activation (water level above the threshold) in the third observation year is similar with the first year, meanwhile, the displacement induced in these two years are also similar. As well as the (Fig. 4.9) simulation of S material illustrated, similar magnitude of movement are captured during the first and third cycle, correspondently, the self-

regulating index experience no discernible decrease. These analyses indicate that Minor Creek landslide was relatively stable during the observations, which matches the observed movement patterns for this landslide.

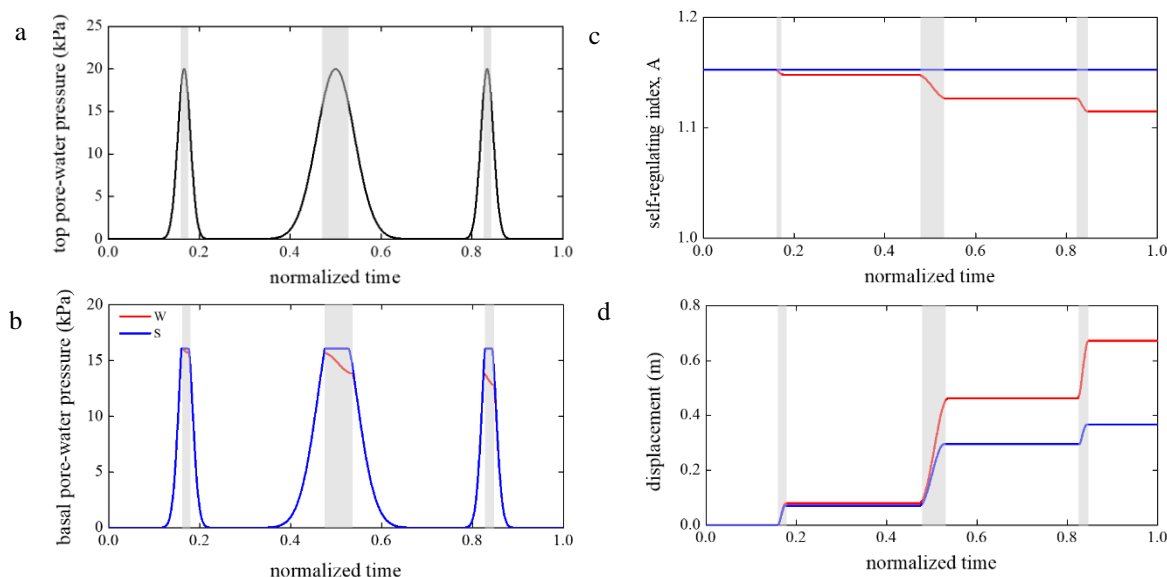


**Figure 4.9** Landslide response to three wetting pulse that with same magnitude but different shape of pore-water pressure distribution. a) Applied pore-water pressure changes on top of shear zone. b) Basal pore-water pressure changes. c) Self-regulating index evolution under wetting. d) Wetting induced slope displacement. Shaded polygon indicates material under plastic domain. Each water cycle is 30 days long. The previous synthetic landslide (Fig. 4.7) is tested here with material W and S.

In addition to explore stable creep movements, this section also investigates the performance of the sliding consolidation model based on MCC for a case that suffered catastrophic acceleration. In this case, the Mud Creek landslide event (discussed before) is analyzed and compared against simulations of another moving landslide displaying stable response (Paul Slide), located about 30 km away from the Mud Creek site, but also within the KJf. For these two cases, movements from 2015 to 2017 were collected (Fig. 4.10a) with InSAR analysis by Handwerger et al., (2019). The precipitation has also been observed by a nearby rain gage (20 km from Paul slide), cumulative rainfall is plotted in Fig. 4.10b. It shows that in three consecutive years from 2015 to 2017, the magnitude of cumulative rainfall increased monotonically with consecutive wet and dry season

(Corominas et al., 2000). As a result of this forcing, both landslides experienced an increase of their downslope velocity in the later year.

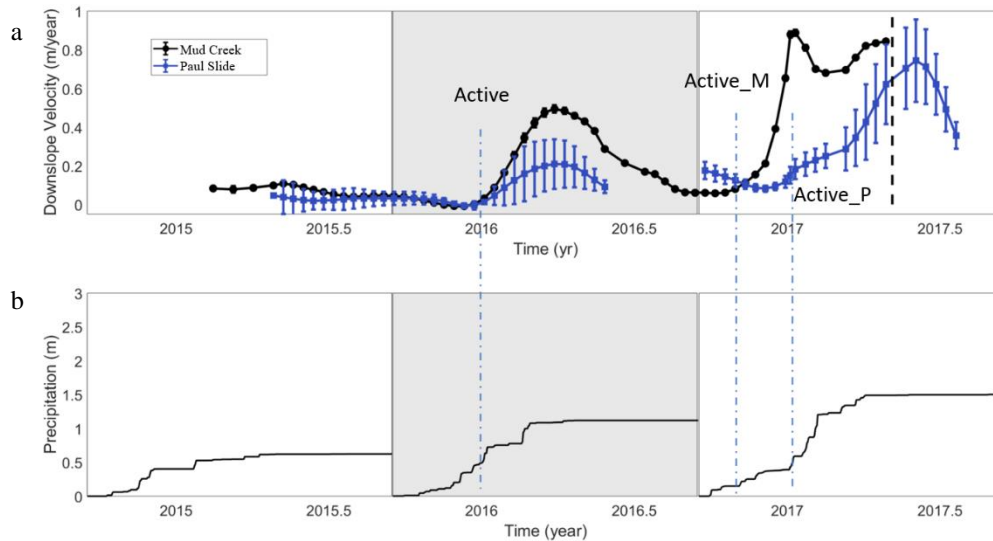


**Figure 4.10** Velocity of the Mud Creek landslide and Paul Slide and corresponding cumulative precipitation data from 2015 to 2017. a) InSAR observed velocity change (data after Handwerger et al., 2019). b) cumulative precipitation recorded from a weather station located 20 km and 50 km from Mud Creek and Paul Slide. Dash-dot line represents the obvious acceleration of each case at each year, dash line A is a reference line showing that the acceleration of Paul slide corresponding to the cumulative rainfall.

In order to interpret the mechanics of pre-failure movements induced by hydraulic cycles with increased cumulative rainfall, the synthetic landslide is tested with consecutive water cycles as illustrated in Fig. 4.11a. As a result, the pore-water pressure transients upon rainfall infiltration can be computed by the hydrological method discussed before.

Two materials (S and M from previous simulation in Fig. 4.7) are tested upon these hydraulic events. Here the M material is used to investigate a weakening behavior, in that these wetting events with increased magnitude induce discernible differences between M and S scenarios, also it will bring material W to failure which makes it less straight-forward to be compared. Simulations show that weakening material will experience decrease of self-regulating index, decreased bottom

pore-water pressure during plastic wetting, and larger movements (Fig. 4.11b-d). Significantly, the movement activation time for each simulated material will be different in the later hydraulic cycle.

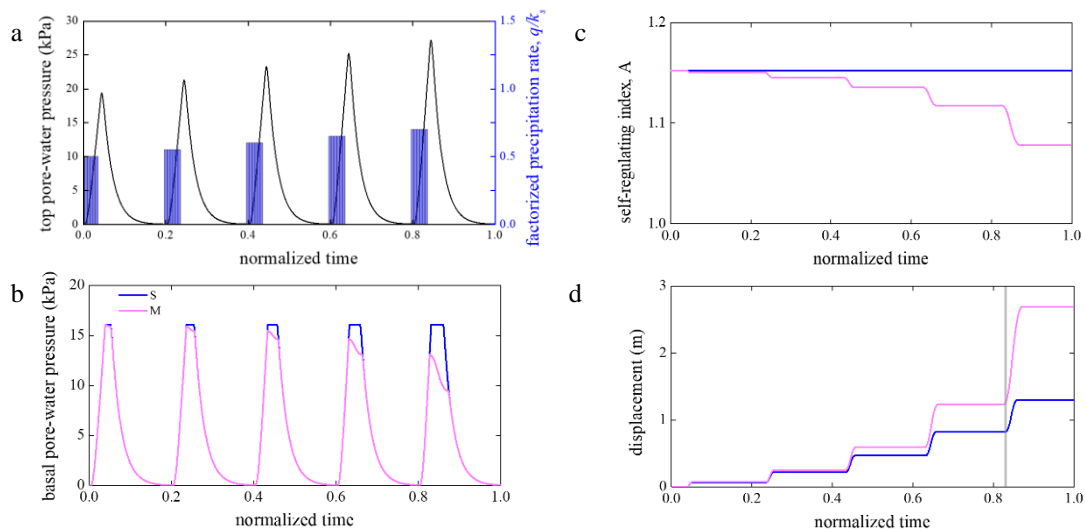


**Figure 4.11** Landslide response to five consecutive wetting pulses induced by monotonically increased constant rainfall. a) Applied rainfall condition on the top of ground surface and induced pore-water pressure changes on top of shear zone. b) Basal pore-water pressure changes. c) Self-regulating index changes under wetting. d) Wetting induced slope displacement. The shaded band indicates the time lag between two plastic stage activations. Each water cycle is 30 days long. The previous synthetic landslide (Fig. 4.7) is tested here with material M and S.

Specifically, in Fig. 4.11d, the material M activates earlier than material S as illustrated by the shaded polygon. The time lag, although not readily apparent, is important to emphasize some of the key signatures of weakening behavior in slow-moving landslides. For example, by examining the simulations of Mud Creek and Paul slide, the activation time for both cases in each water year is marked by dot-dash lines (Fig. 4.10). It can be shown that, although both landslides experience higher velocity in later water years, Paul Slide is mobilized by a similar amount of cumulative rainfall. However, in 2017 Mud Creek starts to slide under a considerably lower amount of cumulated rainfall. Such an early activation signals that Mud Creek was being driven towards failure, as well as the simulated response of material S (Fig. 4.11). From these analyses, if a slope

is weakening upon wetting, it tends to be triggered by increasingly lower magnitudes of hydraulic forcing compared to previous events.

These analyses, in addition to synthetic landslide simulations, suggest that the stable stages of slow creep that precede rapid spontaneous stages of acceleration can be used to indicate if a landslide is approaching conditions favoring a runaway dynamics. In addition, it was shown that the proposed self-regulating index can be used to evaluate the type of landslide dynamics quantitatively, as illustrated in synthetic landslide simulations mobilized by very simple hydraulic events. In the next section, the proposed methodology will be further used to examine two study sites, with the goal to capture their movement dynamics, as well as their potential to runaway failure.

#### *4.4 Case studies*

In this section, two of the landslide sites described before (Two Towers and Mud Creek) will be studied from the viewpoint of their potential to develop a runaway dynamics. The Mud Creek landslide is selected to test the model performance in capturing the transition from stable slow movements to catastrophic runaway failure. By contrast, the Two Towers landslide, already shown to display stable creep movements, is used as a comparison to illustrate the versatility of the proposed approach.

##### *4.4.1 Two Towers landslide*

Two Towers landslide, which has been simulated in Section 3.4.1 by using a Mohr-Coulomb model is simulated again here in conjunction with MCC. For this case, precipitation and induced basal pore pressure are all monitored (Fig. 4.12a), where the pore-water pressure is observed through ground-based equipment (Schulz et al., 2018) and applied directly to simulate the displacement. In accordance with the proposed methodology, the unknown parameters are the

saturated permeability ( $k_s^S$ ), the yield parameter ( $m$ ), and the hardening parameter ( $B_p$ ) of the shear zone material. After trial and error, when the parameters equal to the values in Table 4.1, the monitored displacement can be captured satisfactorily as illustrated in Fig. 4.12b.

More significantly, during the computation of displacement, the self-regulating index (Eq. 4.6) can be tracked directly and simultaneously as plotted in Fig. 4.12c. Results show that, this landslide barely experiences self-regulating index variation during the three years hydrological effects ( $A=1.08$  and is not driven closer to 1 during simulation), which indicates that this slope is stable, and no runaway failure would be triggered, just as observed.

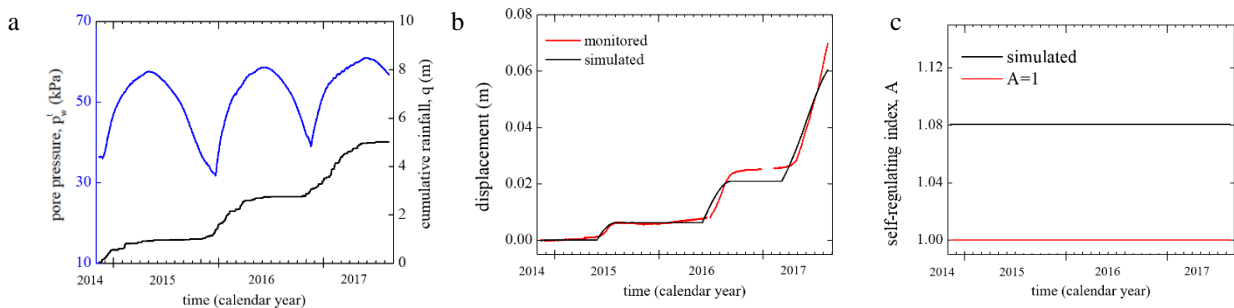


**Figure 4.12 Simulated displacement and computed self-regulating index for Two Towers landslide. a) Monitored cumulative rainfall and basal pore-water pressure. b) Simulated and monitored displacement. c) simulated self-regulating index in addition to the failure scenario,  $A=1$ . Data after Schulz et al., 2018.**

#### 4.4.2 Mud Creek landslide

Mud Creek landslide is here used to test the model performance in capturing the transition from stable sliding to catastrophic acceleration based on records of pre-failure movement. This case has been discussed previously, emphasizing that this landslide failed catastrophically after years of stable sliding. Here, the MCC parameters are calibrated by fitting observed pre-failure movements and then used to examine the evolution of the self-regulating index.

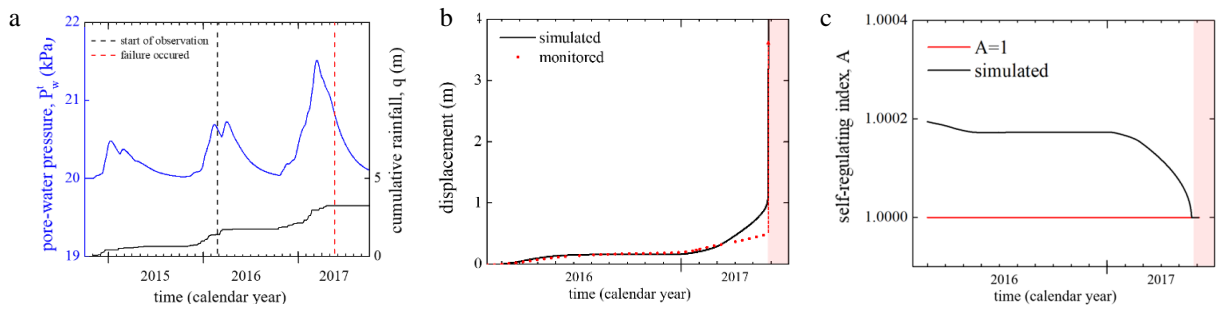


**Figure 4.13 Simulated pore-water pressure, displacement and self-regulating index of Mud Creek landslide. a) monitored cumulative rainfall and simulated basal pore-water pressure. b) Simulated and monitored displacement. c) simulated self-regulating index in addition to the failure scenario,  $A=1$ . The displacement data is obtained by Handwerter et al., 2019 through InSAR analysis.**

**Table 4.1 Parameters for each case study**

Model parameters	Two Towers	Mud Creek
$k_s^s$ (m/s)	$2.6 \times 10^{-11}$	$1.3 \times 10^{-11}$
$m$ (-)	0.4	1.1
$B_p$ (-)	1000	6990

Since ground-based pore-water pressure monitoring is not available for this case, simulated pore-water pressure changes (Fig. 4.13a) at the top of the shear zone (i.e., driven by the precipitation measurements) are used, as explained in Section 3.4.3. Applying this hydrologic loading to the shear zone and simulating the landslide movement with the proposed methodology (parameters in Table 4.1), the stable creep of this landslide can be captured. Most notably, the runaway failure that took place on May 20<sup>th</sup> can also be simulated (Fig. 4.13). Similarly, the self-regulating index during the modelling of displacement can be tracked (Fig. 4.13c). The results shows that index  $A$  approaches 1 around the failure time. This example corroborates the premise of this chapter, i.e., that the combination of coupled flow-deformation framework with critical state theories is

essential to distinguish stable creeping landslides from systems that, although apparently stable, possess an underlying progression towards runaway conditions associated with impending critical state.

#### *4.5 Summary*

Catastrophic slope failures can lead to loss of life and cause excessive damage to infrastructure. These devastating events are normally anticipated by slow movement manifesting over durations spanning from few days to decades, which makes it crucial to explain the emergence of rapid acceleration based on records of slow movements. With this motivation, this chapter focused on the transition from stable sliding to runaway failure, with the goal to define a metric to evaluate the potential for runaway conditions based on pre-failure movements. The methodology used in this chapter is based on the coupled flow-deformation platform proposed in Chapter 3. In particular, this chapter explores the factors that promote transitions from stable movement to catastrophic failure. To address these issues, the sliding consolidation framework is therefore augmented by incorporating a critical state plasticity model (Modified Cam clay) accounting for the simultaneous evolution of both shear strength and volume change characteristics on the basis of well-established soil mechanics theories.

Simple hydraulic events have been simulated to examine the dynamics of synthetic landslides, as well as to explore the model's capability to simulate runaway events following slow creep. In addition, an index conveying the potential for runaway events ( $A$ ) was proposed, to facilitate the identification of deteriorating stability conditions. Furthermore, the manifestation of a slope that experiences weakening was explored on the basis of its creep movement. The results of the analyses show that pre-failure trends such as, the magnitude and duration of creep movements under

sequential hydrological forcing, can be used to examine the stability of a slow-moving landslide. The methodology is then applied to studies sites located in the California Coast Ranges. The results show that by capturing creep movement, it is possible to infer landslides possessing marked tendency to approach runaway failure. These results and the proposed methods can be therefore regarded as useful tools to investigate the dynamics of landslides by linking their stages of stable creep driven by rainfall with the emergence of devastating acceleration, an activity essential to reduce the risk for communities and protect strategic infrastructure.

## 5. CONCLUSIONS AND FUTURE WORK

### *5.1 Summary*

This thesis has formulated new physically-based models able to replicate the dynamics of slow-moving landslides, including possible transitions from a stable, self-regulated creeping stage to unstable, self-feeding runaway events. The models were all based on underlying elasto-plastic or visco-plastic representations of the inelastic deformation within a basal shear zone, as well as on the role of such inelastic effects on the coupling between excess pore pressure feedbacks and landslide motion. The model was tested on the basis of different case studies, all selected from widely characterized test sites across the California Coast Ranges. Such datasets were used to calibrate the model parameters and test its performance in capturing distinct modes of movement, ranging from slow quasi-continuous sliding to episodic slips or even catastrophic runaway failures.

Based on in-situ observations, the geomechanical model used to simulate the dynamics of slow-moving landslides was assumed to consist of three components: rigid landslide body, undeforming stable material, and basal shear zone where most of deformation is concentrated. The simulations illustrated in this thesis were all based on a simple scheme of infinite slope, and thus represented the development of pore pressure transients through 1D numerical diffusion models driven by rainfall infiltration. Consequently, the external loading of the shear zone material resulting into mobilization of plastic deformation was obtained in accordance with Terzaghi's principle of effective stress as a result of fluctuations of the normal effective stress.

On such basis, mechanical and hydrological models specialized for an inelastic shear zone material were used. A new hybrid rheological law which aims at replicating the inelastic strain rate of earthen materials prior to frictional yielding was proposed to reconcile landslide motion analyses

with evidence from remote sensing measurements. It was shown that the proposed model can be used to capture satisfactorily different types of slow-moving landslides, ranging from quasi-continuous sliding to episodic slips. However, given the formulation of the model in a quasi-static context, its applicability for landslides characterized by stages of dynamic behavior was limited.

As expounded in prior studies, this work also recognized the importance of volume changes in the shear zone. This premise led to the formulation of a versatile fully coupled hydro-mechanical framework to simulate the landslides dynamics triggered by hydrologic forcing as a function of general constitutive description of inelastic deformations within the shear zone. Specifically, the proposed framework can be used to solve the interaction between water flow and earthen material elastoplastic deformation. The framework included sequential, interconnected diffusion processes within the landslide body and the inelastic shear zone. By using a simple Mohr Coulomb model, the proposed methodology can predict either stable creep or catastrophic runaway failure depending on the plastic properties of the shear zone material, including its dilative/contractive nature. Case studies show that distinct types of landslide behaviors can be simulated satisfactorily with reduced computational cost and a limited number of model parameters.

Most notably, the framework was able to resolve the transition from stable sliding to catastrophic runaway failures if combined with the critical state theory, here incorporated by means of the classic Modified Cam Clay model. On such basis, a self-regulating index was proposed that can be used to evaluate the character of the calibrated landslide motion in terms of deterioration of the shear zone properties and convergence towards catastrophic behavior. Possible strategies to explore this transition from stable creep to runaway failure were discussed and a number of case studies was used to test the model performance numerically.

## *5.2 Discussion and recommendations for future research*

This thesis presented physically-based hydrological and mechanical models that can be used to solve the dynamics of landslides driven by rainfall infiltration. The proposed methodologies can be used to interpret distinct types of landslide motion satisfactorily. Most significantly, they enable the prediction of catastrophic runaway acceleration if combined with the critical state theory.

The proposed hybrid rheological model was shown to improve simulations of creeping landslide behavior compared to classic Bingham-like rheology. Most notably, it was shown that it has the potential to interpret multiple classes of time-dependent landslide behaviors, including quasi-continuous creep and episodic slips.

The main advantage of the proposed coupled hydro-mechanical framework is the ability to be linked with virtually any constitutive law for inelastically deformable geomaterials, thus opening endless opportunities in terms of the simulation of the magnitude and rate of landslide movements, including transitions between deformation regimes. These benefits include the possible to augment the constitutive description as desired, or as required by the type of application. For example, this thesis illustrated the benefits of incorporating the critical state theory to enable spontaneous convergence towards catastrophic landslide response as a function of varying rates and magnitudes of hydraulic forcing, sliding velocity, and excess pore pressure. While the proposed model remains simplified in nature, it offers enormous benefits in terms of computational efficiency compared to other simulation methods such as those based on FEM, MPM, or SPH computations.

Most notably, in this thesis, multiple a novel metric to evaluate the transition of a slow-moving landslide from its stable (pre-failure) movement to runaway behavior was proposed. By analyzing the magnitude and duration of landslide creep, in conjunction with the corresponding character of

the hydrologic forcing, it was shown that it is possible to anticipate whether a slope undergoes weakening upon downslope movement and is destined to achieve critical state conditions and, eventually, a catastrophic landslide dynamics. The proposed framework thus provides powerful tools to monitor the life cycle of landslides and forecast devastating mass wasting hazards.

Despite these benefits, similarly as other computational methodologies, limitations exist which warrant further research and enrichments of the proposed approach. At this reference, below some potential opportunities stemming from this work are outlined to guide future research on landslide science. In particular:

- i) The current methodology has been built by using the standard of infinite slope model. Although widely used in landslide analyses, this simplified representation of the slope morphology inevitably fails to capture numerous aspects of the hydro-mechanics of landslide movement, including lateral resistance, downslope fluid flow and consequent seepage drag, and progressive failure associated with localized weakening of the shear zone material. To address these issues, higher-dimensional models are called for.
- ii) The infiltration within the landslide body shown in this work is solved by a linear diffusion equation involving water mass balance and consequent computation of pore-pressure transients upon precipitation. This choice inevitably neglects the non-linear effects stemming from lacking saturation within the vadose zone, which here could not be considered primarily because of the lack of relevant ground-based observation. However, unsaturated effects can greatly influence slow-moving landslides activation and their subsequent dynamics of motion. Future extensions of the present work may thus involve augmented diffusion-advective models able to take unsaturated effects into account. In an effort to do that, the unsaturated parameters regarding earthen

material Water Retention Curve and Hydraulic Conductivity Function can be obtained through optimization based on ground-based monitoring and/or remote sensing data of water content distribution.

- iii) The proposed framework based on critical state model leads to failure after a sufficient number of hydrologic forcing cycles. Since sliding during wetting induces a decrease of self-regulating index, even for a considerably stable slope, theoretically the state is always driven closer to failure following each cycle of sliding (even if, based on some of the cases studied in this thesis, this may occur at very slow pace). It is therefore valuable to investigate the fate of each actively moving landslide under long-term forcing scenarios, in order to estimate for an expected (or average) precipitation how long will it take for the self-regulating index to reach critical conditions. The self-regulating index evolution of a slow-moving landslide is governed by the material weakening, hydrological forcing, etc. The shorter a slope is expected to experience runaway failure from computation, it is more dangerous. This investigation would provide an ideal indicator to examine the fate of a slow-moving landslide when forecasting and manage the landslide damage.
- iv) The Modified Cam Clay model works well on capturing the landslide dynamics under cycles of hydraulic forcing. However, it is also interesting to investigate the model's performance during droughts. In fact, once the yield surface is approached by a drying-induced stress path, the self-regulating index will increase, thus indicating a state moving away from failure. This simple result fits satisfactorily common expectations, in that a slope will be driven towards runaway failure under extreme precipitation, and on the contrary, it will become more stable under extreme droughts. However,

following the drying driven surpassing of yield surface, downslope movement induced by plastic shear strain may also be induced. Although observations of slope movement under dry season are scarce, their analysis can be interesting to examine how numerous drought cycles can generate apparent drying-induced over-consolidation of the shear zone material and thus alter the strength properties that will govern the landslide response upon successive extreme rainfall. A possible way to improve the methodology to examine these phenomena is therefore the incorporation of bounding surface plasticity models suitable to study cycles of alternating consolidation paths, and consequent impacts on the resistance of cyclically loaded shear zone materials.

## **APPENDIX. REGIONAL-SCALE SIMULATION OF FLOWSLIDE TRIGGERING IN STRATIFIED DEPOSITS**

Work in this appendix focuses on the simulation of two types of shallow landslide triggering at stratified deposits, and is prepared based on Li et al., 2021. Capturing the failure mechanisms responsible for static liquefaction is a challenging task for the zoning of landslide susceptibility. While geomechanical models accounting for solid-fluid coupling can identify locations prone to flowslides, their performance in regional settings is impacted by the lack of procedures to replicate accurately stratigraphic heterogeneities. To mitigate this inconvenience, this appendix discusses the performance of a spatially-distributed model aimed at capturing distinct landslide triggering mechanisms in layered deposits. The proposed model is able to take into account the vertical heterogeneity of individual slope units, while dramatically reducing the computational cost of regional-scale analyses. The following sections illustrate briefly the numerical model and its implementation. Afterwards, the model is tested with reference to an extensively studied series of shallow landslides that took place in 1998 in the region of Campania, Italy, after a heavy rainstorm event. In the remaining, the same methodology is used with reference to four municipalities characterized by different representative stratigraphic conditions, in order to discuss its performance in the presence of sites with widely different site heterogeneity.

### *A.1 Flowslide triggered in stratified deposits*

Landslide susceptibility zonation is the first step of regional hazard management (Ayalew & Yamagishi, 2005). Very often, it is also an extraordinarily challenging task, especially in case of rainfall induced slope instabilities, which can take place within a temporal interval of few hours and involve areas of several km<sup>2</sup> (Baum et al., 2005; Van Westen et al., 2006). More importantly, various failure modes (Hungr et al., 2014) can exist across the same landscape, each leading to a different degree of post-failure mobility. Among them, two interesting end-members are frictional slips (characterized by a clearly identifiable failure surface and often displaying slow, episodic movement) and liquefaction-induced flowslides (caused by an unstable growth of the pore fluid pressure and ensuing rapid runaway movements). Such different forms of shallow landslides can often be observed within same region (Cascini et al., 2008), depending on site-specific combinations of slope angle, porosity and degree of saturation (Picarelli et al., 2008; McKenna et al., 2012). As a result, their complexity and coexistence call for an accurate characterization of the hydro-mechanical processes leading to them and responsible for the initiation of either form of slope failure. Over the last several decades, a remarkable amount of contributions to the regional-scale modeling of landslide models has become available (Montgomery & Dietrich, 1994; Wu & Sidle, 1995; Pack et al., 1998; Crosta & Frattini, 2003; Baum, et al., 2010; Bellugi et al., 2015), most of them being rooted on the mechanics of frictional failure. However, comparatively smaller attention has been given to shallow landslides driven by other forms of soil instability, such as static liquefaction.

A departure from such logic is encoded into recently proposed numerical strategies to compute safety factors for flowslide triggering at regional scale (Lizárraga and Buscarnera 2017; Lizarraga et al., 2017). Similar to earlier suggestions (Iverson & Major, 1987; Iverson, 2005; Buscarnera and

di Prisco, 2013), these tools capture the role of hydro-mechanical coupling on the onset of shallow landslides. However, they also make reference to the idealized case of homogeneous deposit, which is widely known to affect severely the intensity of pore pressure transients, the location of failure zones and the degree of saturation at failure (Cuomo & Iervolino, 2016; Reid, 1997; De Vita et al., 2013). This appendix aims to remove the abovementioned approximations in the representation of the natural heterogeneity by incorporating stratigraphic layering in the analysis of flowslide triggering. For this purpose, the methodology proposed hereafter builds on the vectorized Finite Element framework recently proposed by Lizárraga and Buscarnera (2018), through which it is possible to solve transient infiltration equations in regional-scale settings in a computationally efficient fashion.

## *A.2 Model implementation*

### *A.2.1 Hydraulic model*

A key component involved in the analysis of rainfall-induced landslide processes is the simulation of pore pressure transients due to infiltration events. Such steps relies on the enforcement of the water mass balance, which in the unsaturated regime can expressed as follows (Richards, 1931):

$$nC_w(h) \frac{\partial h}{\partial t} = \nabla \cdot [K(h) \nabla (h + z)], \quad (\text{A1})$$

where  $n$  is the porosity,  $h$  is the pressure head induced by capillarity,  $t$  is time,  $z$  is the vertical coordinate,  $K(h)$  is a hydraulic conductivity function (HCF), and  $C_w(h)$  is the unsaturated storage coefficient (i.e., the rate of change of degree of saturation  $S_r$ , with respect to  $h$ , determined by water retention curve, WRC). Eq. A1 supplemented with initial and boundary conditions constitute the problem to solve for each slope unit within the landscape.

Although under special circumstances such second-order partial differential equation can be solved in analytical form (Iverson, 2000; Srivastava and Yeh, 1991), the wide variety of nonlinear models for water retention and permeability, as well as the need to incorporate natural heterogeneity, often call for numerical solutions. Here, a Finite Element algorithm is used for this purpose (Lizarraga and Buscarnera, 2018) in order to ensure flexible assignation of material properties, boundary conditions and layering characteristics. This choice involves a spatiotemporal discretization in order to convert the differential problem in algebraic form (Celia et al., 1990; Van Dam & Feddes, 2000). Galerkin spatial discretization and an explicit forward temporal scheme have been used, thus following standard computational techniques for multi-phase flow (Chen et al., 2006; Zienkiewicz et al., 1999).

### *A.2.2 Mechanical model*

Landslide susceptibility analyses require the evaluation of the margin of safety of individual slope units. Here, such step is carried out with reference to idealized infinite slope models spatially distributed across the landscape. For each of these, factors of safety, FS, are computed in order to signal failure (i.e.,  $FS < 1$ , in accordance with standard limit equilibrium methods; Duncan et al., 2014). In this work, the FS expressions proposed by Lizárraga & Buscarnera (2017) on the basis of material stability theories (Buscarnera and di Prisco, 2011; 2012) have been used to assess instabilities initiated by either frictional slip or liquefaction (i.e., flowslides). Specifically, the FS associated with the onset of frictional slips under drained conditions is given by:

$$FS_{SLIPS} = \frac{\tan\phi'}{\tan\alpha} \chi_s \quad (\text{A2a})$$

$$\chi_s = 1 + \frac{ks}{\sigma_{net}} \quad (\text{A2b})$$

where  $\varphi'$  and  $\alpha$  are friction angle and slope inclination, respectively,  $\sigma^{net}$  is the net stress,  $s$  is the suction value and  $k$  is a parameter that quantifies the effect of suction on the shearing resistance. The coefficient  $\chi_s$  incorporates the effect of suction on stability of the slope, reflects the suction variation impact on strength. By contrast, the FS reflecting the onset of flowslides is given by:

$$FS_{FLOWS} = \frac{\tan\varphi^{LIQ}}{\tan\alpha} \chi_s \chi_w \quad (A3a)$$

$$\chi_w = 1 - \left( \frac{\sigma^{net}}{k} + s \right) \left( r_w + \frac{n}{\lambda S_r G(S_r)} \right) \quad (A3b)$$

where  $\varphi^{LIQ}$  is the mobilized friction angle at the onset of liquefaction,  $r_w$  is a suction-hardening parameter,  $\lambda$  is the plastic compressibility,  $S_r$  is the degree of saturation,  $G(S_r)$  is the derivative of the water retention curve with respect of  $S_r$ . As is readily apparent from the previous expressions, both types of FS are expressed as functions of suction, thus incorporating a strong dependence of the margins of safety on transient hydraulic processes.

### A.2.3 Vectorized Finite Element Framework

The vectorized Finite Element framework used in this paper was proposed by Lizárraga and Buscarnera (2018). Rather than simulating sequentially infiltration equations for all the cells of a discretized landscape, this method runs the calculations in aggregated form by arranging the cells representing individual slope units through a matrix notation. The main benefit of such strategy is the possibility to substantially reduce the computational costs of a regional-scale analyses. For example, with reference to the computational assessment of landslide susceptibility for an 8 km<sup>2</sup> landscape discretized with pixel resolution of 5 x 5m, this approach can result to computation time of about one third compared to a sequential solution method. The key features of the vectorization

algorithm specific for this paper are schematically depicted in Fig. A1, while further details are provided by Lizarraga and Buscarnera (2018).

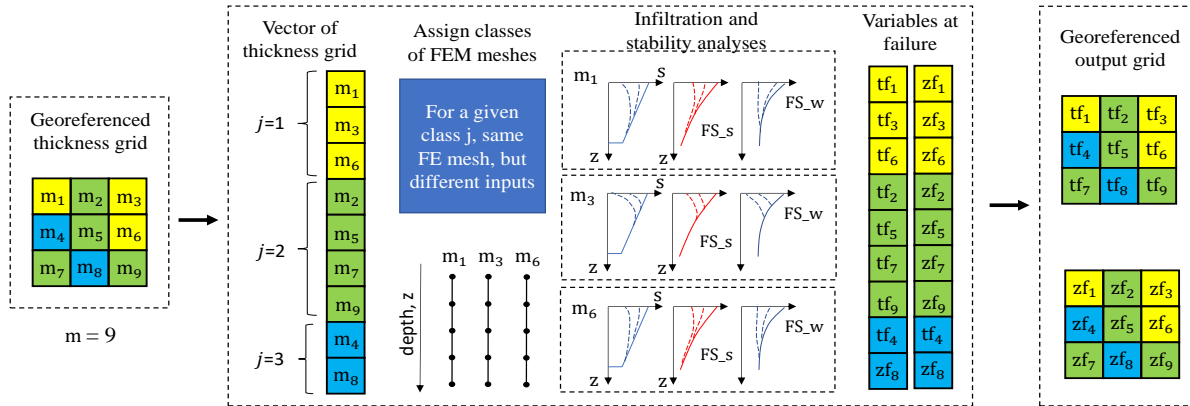


**Figure A.1 Schematic representation of model workflow.  $m$  = number of cells,  $j$  = number of cell classes with the same FE mesh,  $tf$  = failure time,  $zf$  = failure depth,  $s$  = suction,  $FS_s$  = factor of safety of slips failure;  $FS_w$  = factor of safety of flowslides.**

### A.3 Case study

#### A.3.1 Selected sites

The events that took place in 1998 in Campania, Italy, after a heavy rainstorm, represent some of the most extensively studied cases of shallow landslide of the recent history. Detailed accounts of these events are provided by numerous contributions (Crosta and Dal Negro, 2003; Guadagno et al. 2005; Cascini et al. 2011). Here, only key data immediately relevant for the purposes of this paper are briefly discussed.

The area of interest is in the Pizzo d'Alvano massif. The soils involved in the abovementioned shallow landslides consist of interbedded layers of unconsolidated air-fall pyroclastic deposits. Here, alternations of ashes and pumices are often found, resulting in stratified profiles across the landscape (Cascini et al, 2005) with thickness ranging from less than a meter to more than 5 meters (Cascini et al., 2008). While the landscapes where most landslides occurred are characterized by a

depth to bedrock within 2 m. In such accordance, computation in this work involved slope units are with thickness of 0.5m, 1.3m and 2m. Furthermore, the hydrologic properties of ashes vary according to their deposition history and depth (Sorbino and Nicotera, 2013). As a consequence, two types of ash, labeled as A and B (for the upper and buried ashes, respectively) are defined.

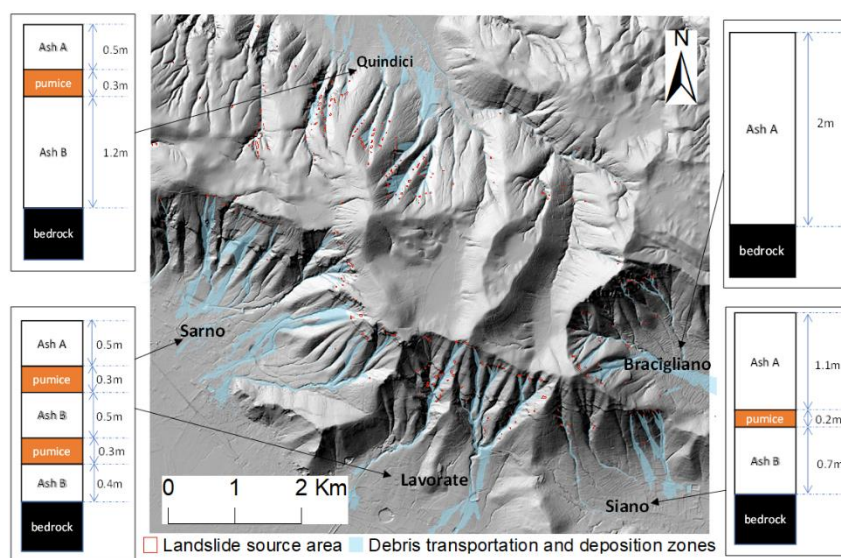


**Figure A.2 Stratigraphic conditions for multiple sites across a portion of the Pizzo d'Alvano massif affected by shallow landslides and failure source area (based on Crosta & Dal Negro, 2003; Cascini & Sorbino, 2003).**

Although highly variable layering was found across the region, Crosta and Dal Negro, (2003); Cascini & Sorbino (2003) identified typical stratigraphic profiles for multiple sites across the affected area (Fig. A2). At the same time, the landslides source areas were mapped over the landscape, along with their transportation and deposition zones (Frattoni et al., 2004). Based on this information, a georeferenced database was generated for the purposes of the analyses discussed hereafter (5x5m DEM).

In addition, available rainfall intensity records from rain gauges located at nearby meteorological stations were used. Specifically, data from the Lauro station (i.e., the closest to the study area) were selected for the analyses.

### A.3.2 Mechanical parameters

The model involves five mechanical parameters (Table A1). Among them, the first four parameters for Ash A were determined on the basis of standard geotechnical tests by Lizarraga et al. (2017). Slight variations in friction angle between ashes were reported by Pirone et al. (2015), while data for pumices is lacking. Thus, for simplicity, identical values of these parameters are here used for all layers. Finally, the remaining parameter  $r_w$ , which controls the susceptibility of a soil to wetting-induced instability, is back calculated for each layer based on the approach proposed by Lizarraga and Buscarnera (2017). Specifically, its value for the two ash is chosen to preserve the flowslide susceptibility calibrated by Lizarraga and Buscarnera (2017). By contrast,  $r_w$  is set to zero in the pumices, thus reflecting lack of flowslide triggering at depths corresponding to such layers.

**Table A.1 Description of mechanical parameters and calibrated values.**

Name of parameter (units)	Symbol	Calibrated value
Friction angle (°)	$\varphi'$	38
Mobilized friction angle at the onset of static liquefaction (°)	$\varphi^{LIQ}$	26
Suction-sensitivity of shear strength (-)	$k$	0.6
Plastic compressibility (-)	$\lambda$	0.11
Suction-hardening parameter Ash A (Kpa <sup>-1</sup> )	$r_w$ (Ash A)	7.35
Suction-hardening parameter Ash B (Kpa <sup>-1</sup> )	$r_w$ (Ash B)	0.72
Suction-hardening parameter Pumice (Kpa <sup>-1</sup> )	$r_w$ (Pumice)	0.0

### A.3.3 Hydraulic parameters

The calibration of the hydrologic parameters for each layer is shown in Fig. A3. Correspondent data related to Water Retention Curve (WRC) and Hydraulic Conductivity Function (HCF) provided by Crosta & Dal Negro (2003) and Pirone et al. (2015) respectively. The model calibration results based on an exponential WRC (Stanier and Tarantino, 2010) and a Gardner HCF (Szymkiewicz, 2012) are displayed as continuous lines in Fig. A3. In addition, extensive tests

regarding HCF of Ash A were conducted (Sorbino, 2005; Papa, 2007; Damiano et al., 2012), where the saturated permeability of such layer were reported between  $1e-6m/s$  and  $3e-6m/s$ .

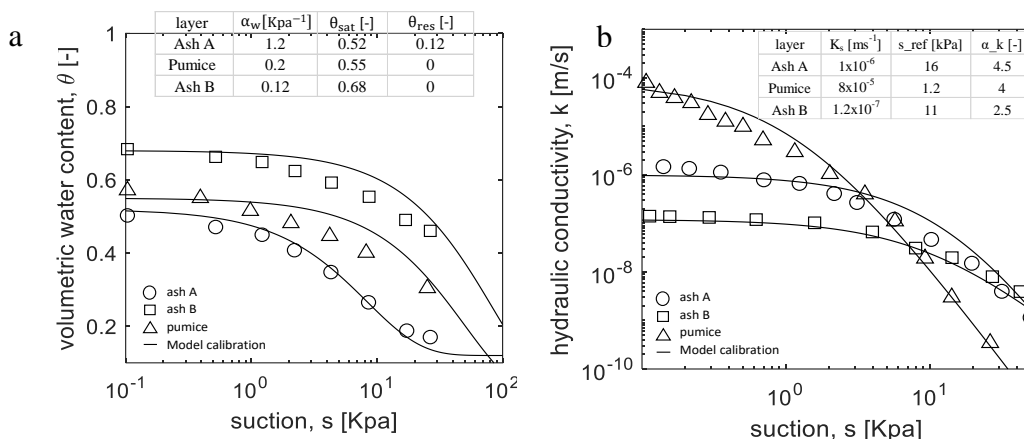


**Figure A.3 Calibration of hydraulic parameters. a) water retention curve (data after Crosta & Dal Negro 2003), b) hydraulic conductivity function (data after Pirone et al. 2015).**

#### A.4 Assessment of model performance

The proposed methodology is here tested against landslide records available for the city of Sarno, for which extensive field and laboratory data is available (Sorbino and Nicotera, 2013). Previous flowslide triggering simulations for this same site have been recently conducted with reference to uniform stratigraphic conditions (Lizárraga et al., 2017). As a consequence, the site offers a unique opportunity to compare the results obtained for the case of layered liquefiable slopes against those resulting from the use of a baseline homogeneous model.

##### A.4.1 Categorization of failure mechanisms

Landslide types are often classified on the basis of their post-failure mobility. In this paper, the term *flowslide* is used to refer specifically to phenomena where static liquefaction is responsible for the initial triggering of the downslope movement, thus often resulting in rapid buildup of pore

water pressure and consequent runaway failure of a fluidized soil mass (Hung et al. 2014). This underlying mechanics is distinct from the phenomenology of frictional failure, in which a well-defined slip surface is generated and the failure leads to limited or negligible engagement of pore water pressure, as well as to relatively little mobility. For these reasons, this more common class of shallow failure is here referred to as *frictional slip*, in that it is treated as an uncoupled (drained) mechanism associated with the engagement the soil strength. Accordingly, the failure mechanisms detected at the Sarno site can be differentiated based on their propagation distance (Crosta & Dal Negro 2003).

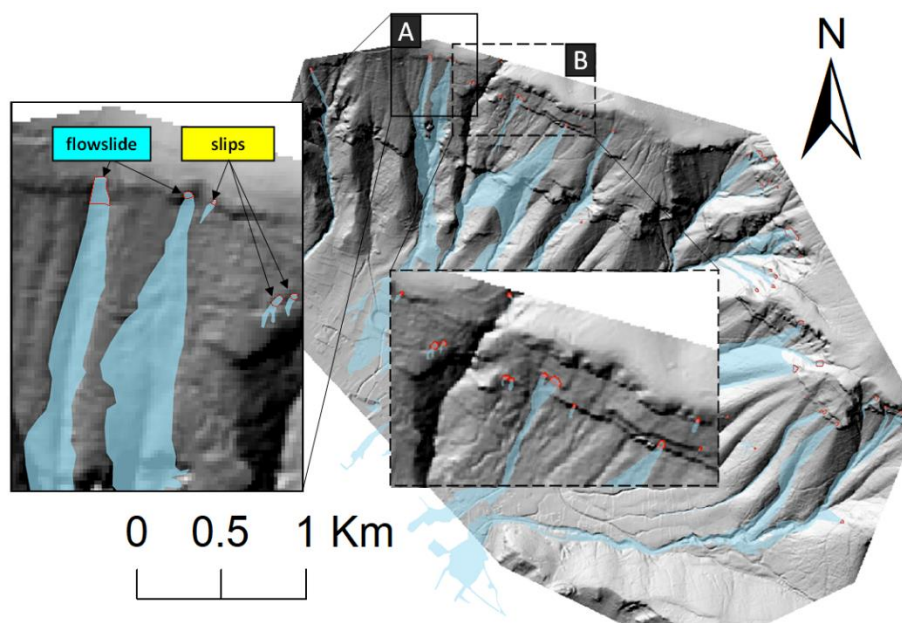


**Figure A.4** Landslide transportation and deposition zones (Crosta and Dal Negro 2003).

Let us consider for example area A in Fig. A4, where five landslides source areas were detected. Three of such landslides led to a post-failure movement of limited extent (i.e., runout distances lower than 30 m), and can thus be classified as frictional slips. On the contrary, the other two failures resulted into large downslope flow-like movements (i.e., runout distance larger than 1 Km), which propagated along the landscape gully. Such type of failures will be here categorized as

flowslides. Although the analysis of the available data at the Sarno site indicates predominance of flow-like failure (i.e., 28% of frictional slips and 72% of flowslides), the distribution of failure mechanisms is by no means spatially homogeneous. In fact, sectors of the landscape where one type of failure mode is predominant can be identified. This is the case of area B in Fig. A4, where a much higher concentration of frictional slips was detected compared to the rest of the site (9 slips out of total 12 failures). Such variations in the frequency of failure mechanisms will be used to test the spatial accuracy of the model predictions.

Preliminary analyses based on layered model slopes were conducted (see stratigraphic profile for the Sarno site in Fig. A2). Specifically, the simulations were inspected by comparing them with those of a homogeneous model based solely on the saturated permeability ( $k_s$ ) of Ash A. For the latter, varying values of  $k_s$  equal to  $1 \times 10^{-6}$  m/s,  $2 \times 10^{-6}$  m/s and  $3 \times 10^{-6}$  m/s were used, in agreement with reported laboratory data. To ensure the consistency of the comparison, these values of  $k_s$  were also used to model Ash A in the stratified model. By contrast, the hydraulic properties of all other layers were set defined on the basis of the calibration in Fig. A3. Both models show satisfactory performance in capturing failure events spatial distribution (Fig. A6) when  $k_s$  equals to  $2 \times 10^{-6}$  m/s. (Details of computation results regarding spatial distributions are discussed in the next subsection, here the concentration is settled on the failure mechanisms.) Under this scenario, the failure mechanisms identified by the model are shown in Fig. A5.

The results show that the stratified model predicts the occurrence of 19% slips and 81% flowslides, while the homogeneous model computed only 8 percent slips. Therefore, although both models predict higher frequency of flowslides, the homogeneous case leads to a severe overestimation of flowslides, while the model based on a more realistic soil profile is characterized by a better agreement with the recorded landslide inventories.

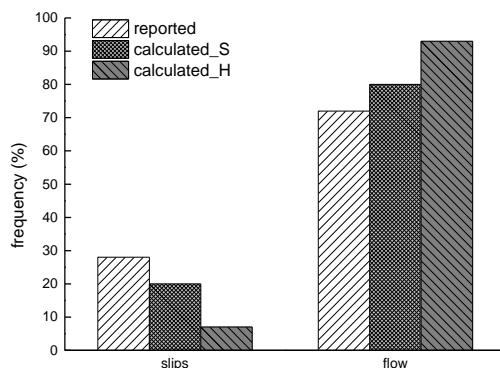


**Figure A.5** Reported and computed relative frequency of slope failure mechanisms.

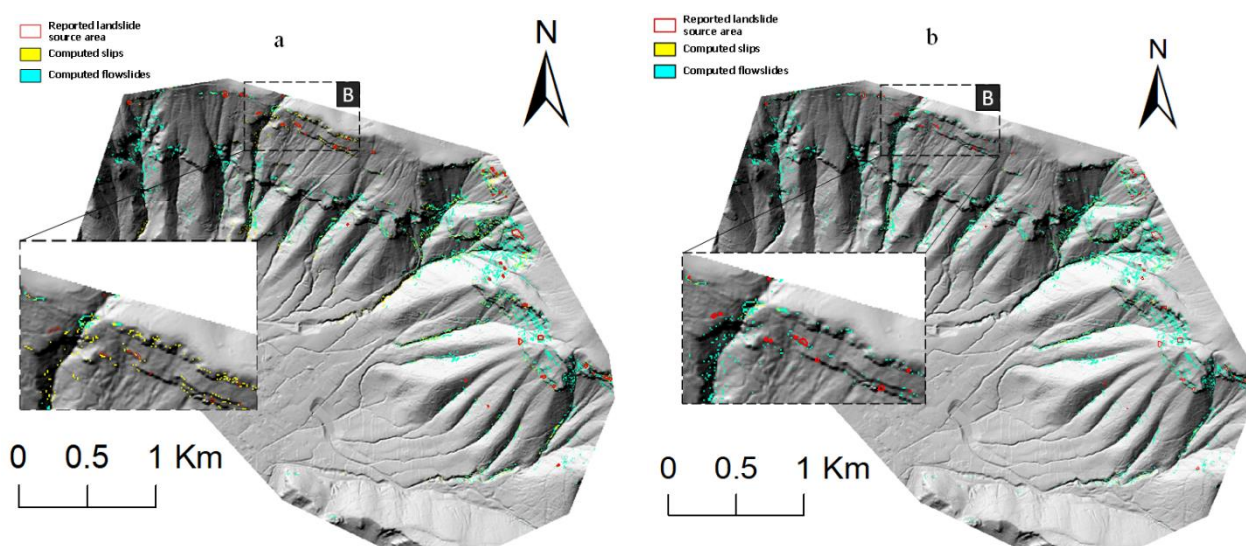


**Figure A.6** Spatial distribution of simulated failure mechanisms through layered and homogeneous models. a) Model based on layered slopes, b) Model based on homogeneous slopes.

The accuracy of the simulations can also be assessed in terms of its spatial accuracy. This is here done with reference to the previously mentioned area B (Fig. A6) in which frictional slips display higher concentration. It is readily apparent that the model with stratigraphic heterogeneity correctly predicts dominance of frictional slips in such sector, while the homogeneous model predicts almost exclusively the onset of flowslides. Such result further emphasizes the advantages resulting from a more realistic representation of permeability contrasts within naturally heterogeneous slopes.

#### A.4.2 Spatial performance

As discussed above, the simulation has been conducted with calibrated parameters (Table A1 & Fig. A3) and Ash A  $k_{\text{sat}}$   $1 \times 10^{-6}$ ,  $2 \times 10^{-6}$ , and  $3 \times 10^{-6}$  m/s according to laboratory tests (Sorbino, 2005; Papa, 2007; Damiano et al., 2012). The results obtained through homogeneous and heterogeneous models are now compared in terms of Success Index (SI), Error Index (EI) and their ratio, SI/EI (Table A2). Such metrics proposed by Sorbino et al. (2010), can be used to assess quantitatively the model performance. In particular, SI represents the percentage ratio of computational cells indicated correctly the reported landslides sources, while EI illustrates the percentage of overprediction.

**Table A.2 Comparison of performance metrics from models with homogeneous and layered slopes. The simulations based on homogeneous slopes assume constant saturated permeability throughout the domain, with value equal to that Ash A. For the stratified model, the Table indicates only the value of saturated permeability,  $k_s$ , of Ash A. The value of  $k_s$  for the other layers is defined in accordance with the hydraulic parameter calibration illustrated in Fig A3.**

Homogeneous model	SI (%)	SI/EI	Stratified model	SI (%)	SI/EI
$K_s = 1 \times 10^{-6}$ m/s	12.7	12	$K_s = 1 \times 10^{-6}$ m/s	18	12
$K_s = 2 \times 10^{-6}$ m/s	28.3	12	$K_s = 2 \times 10^{-6}$ m/s	30	12.5
$K_s = 3 \times 10^{-6}$ m/s	23.8	12	$K_s = 3 \times 10^{-6}$ m/s	33.6	12.4

Results shown in Table A.2, the optimized prediction of two models are both for  $K_s$  equals to  $2 \times 10^{-6}$  m/s scenarios. The performance of all models resulted in values of SI/EI ratio between 2 and 4 times larger than those reported in similar studies for this area. Although this signals a satisfactory performance of all model scenarios, the results based on a realistic depiction of the stratigraphic heterogeneity resulted into higher values of both SI and SI/EI compared to the corresponding homogeneous model. In other words, the incorporation of natural heterogeneity leads not only to better spatial accuracy, but also to more reliable identification of landslide source with lower overprediction of potentially unstable zones.

To further discuss the spatial performance of the model with layered slopes, Fig. A7 reports the landslide triggering susceptibility map obtained from simulations based on  $K_s$  of  $2 \times 10^{-6}$  for Ash A. Although certain sectors of the landscape are still characterized by overprediction (e.g., area D), the computations are able to identify all landslide source areas and the predominant type of slope failure. By contrast, in other sectors (e.g., areas A, B and C), satisfactory agreement with the reported landslide source areas is achieved with limited overprediction. In particular, four clusters of unstable cells were computed in area A, with three of them displaying considerable overlap with the reported source areas.

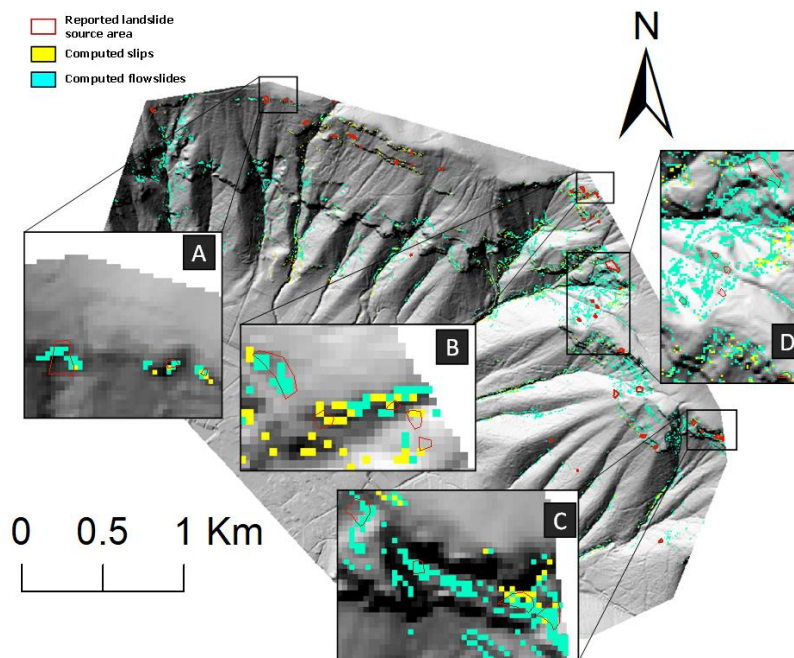


**Figure A.7 Predicted landslide triggering mechanisms in the Sarno site (source areas reported by Frattini et al, 2004).**

#### *A.4.3 Temporal performance*

The temporal stages of landslide initiation for part of the landslides that took place across the Sarno site (contours in Fig. A8a) was discussed by Cascini et al. (2011), who constrained the most likely failure times (44 to 48 hours after the start of the rainstorm) on the basis of witness reports.

Although the accuracy of such values is invariably affected by a number of uncertainties, it can be used as a tentative reference to assess the temporal performance of the model.

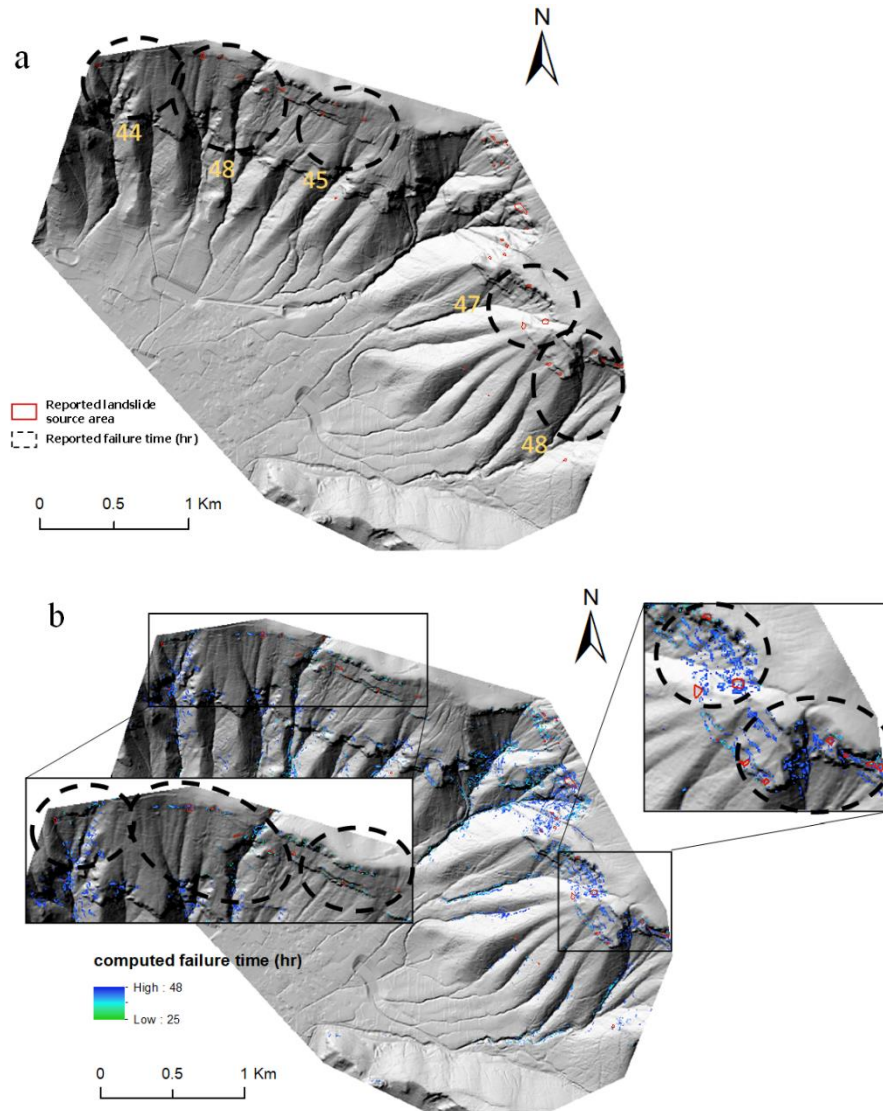


**Figure A.8 Sarno landslide failure time. a) Reported from Cascini et al. 2011, b) calculated in this work**

The computed failure time obtained from the model with layered slopes is shown in Fig. A8b for two specific areas. In the western sector of the landscape, the landslides enclosed by contours with bright green color represent earlier failure mobilization. Except the central contour, where failure was reported to have occurred at the end of the storm, these results are in good agreement with the

data. In the eastern sector of the landscape, the computations are enclosed by contours with darker color, marking relatively late failure initiation. Such results are also consistent with the inventory, thus corroborating the accuracy of the model performance also from the temporal standpoint.

At this reference, a further comparison between homogeneous and layered model is shown in Fig. A9. For both cases slips were predicted to have mostly occurred during the early stages of the storm. Most importantly, the reported failure time (Cascini et al. 2011) ranged between 44 and 48 hours. From Fig. A9a it is readily apparent that the failures computed by the stratified model are concentrated after 41 hours. By contrast, in the homogeneous model, the failure time distribution displays two peaks, one from 32 to 36 hours, and another from 40 to 48 hours. As a result, it can again be concluded that under the standpoint of the temporal predictions, the model based on stratified slopes provides a superior performance compared to an equivalent homogeneous model.

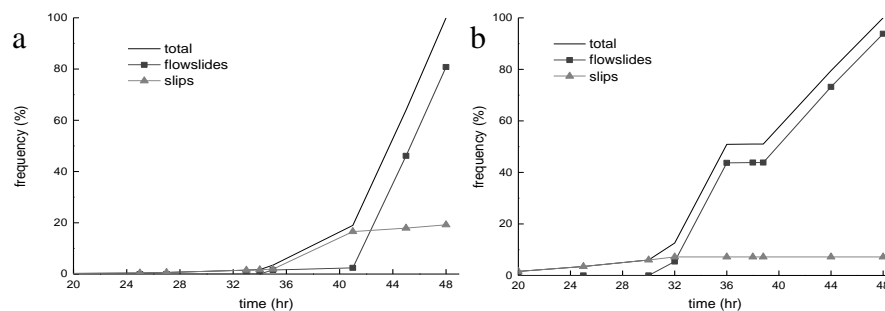


**Figure A.9 Computed failure time history. a) Obtained from stratified model, b) from homogeneous model**

#### *A.4.4 Failure depth*

The failure depth is another important feature to assess the performance of a landslide modeling platform. Such feature can also be calculated both in the stratified and the homogeneous model. The results are compared in Fig. A10 with reported data (based on which the failure depth ranges from 0.4 m to 1.8 m).

For both scenarios, flowslides tend to be obtained at shallow depths. However, while the homogeneous model predicts failure depths densely distributed around 0.4 m, the stratified model provides 40% failures at 0.5m, 40% at 0.9 m, and 20% at depths deeper than 1.3m. It is clear that the failure depths predicted by the stratified model resembles much more closely the distribution emerging from field surveys, thus indicating another important metric for which the incorporation of stratigraphic heterogeneity into a geomechanical model leads to beneficial outcomes.

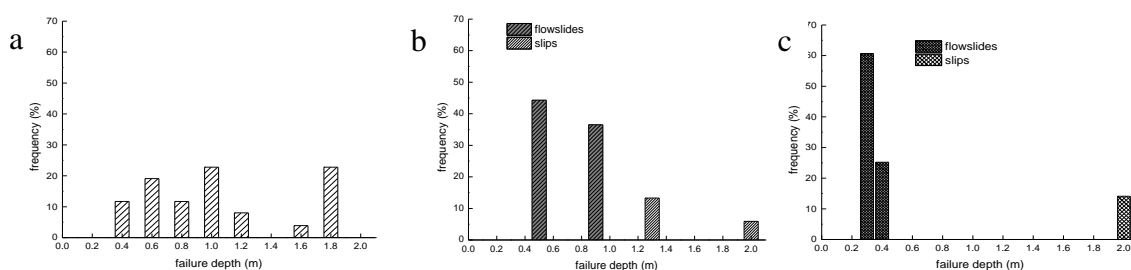


**Figure A.10 Computed and site-investigated failure depth. a) reported by Crosta & Dal Negro 2003, b) calculated from the stratified model, c) calculated from the homogenous model.**

### *A.5 Model application in other sites*

Although, the richness of data at both field and laboratory scale, for the site of Sarno provides an optimal platform to test the model performance, here a broader set of validation examples are discussed with reference to four additional municipalities belonging to the same geological setting (Quindici, Lavarate, Siano and Bracigliano, Fig. A2). Such step relies on field surveys reported by Crosta & Dal Negro and Cascini & Sorbino, from which characteristic stratigraphic profiles for each of these sites were reported. As a result, this additional series of examples is functional to discuss the model performance in the presence of widely different vertical heterogeneity scenarios. Given the prevalence of alternations of deposits of Ash A, Ash B and pumices across Campania, the model functions and parameters previously discussed on the basis of data available for the

Sarno site will be considered applicable also to this new set of analyses. This choice clearly represents a major simplification, in that rigorous analyses would require a complete reassessment of both site-specific hydraulic and mechanical properties, as well as initial and boundary conditions. However, despite its shortcomings, this choice is here simply intended as a working hypothesis aimed at testing differences in model performance for idealized cases in which variations of the stratigraphic profile represent the only important departure between one site and another.

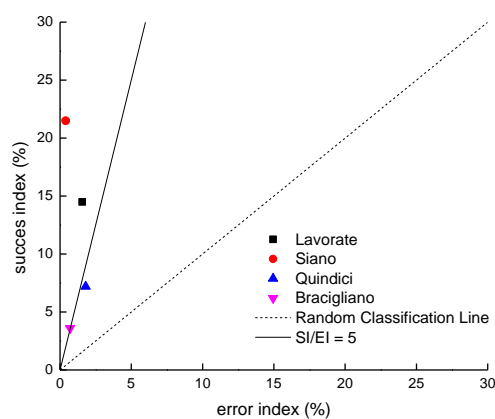


**Figure A.11 Results of model spatial performance for four selected municipalities across the Pizzo d'Alvano massif**

Fig. A11 illustrates an assessment of the spatial performance of the model based on some of the metrics previously discussed, SI and SI/EI. The simulations for Quindici and Bracigliano return values of SI/EI between 3 and 5, hence much lower than those obtained for Sarno, but still close to previous model performances reported by other authors (Frattini et al, 2004; Sorbino et al., 2010; Godt et al., 2008). By contrast, the results reported in Lavorate is nearly twice as high (i.e., SI/EI=9.3), and thus closer to the performance obtained for the Sarno site. Finally, an even superior performance was obtained with reference to the site of Siano, for which values of SI/EI nearly one order of magnitude higher than those obtained for the other sites were obtained (i.e., SI/EI=54).

Such major variability in performance clearly suggests that, despite its importance, the stratigraphic profile cannot be regarded as the only factor differentiating one site from the other. At the same time, they indicate that the performance of all models relying on stratigraphic heterogeneity is at the very least comparable with that of other similar models available in the literature and can even be order of magnitudes superior to standard models when the calibrated parameters reflect the actual hydro-mechanics of the soils present at the site.

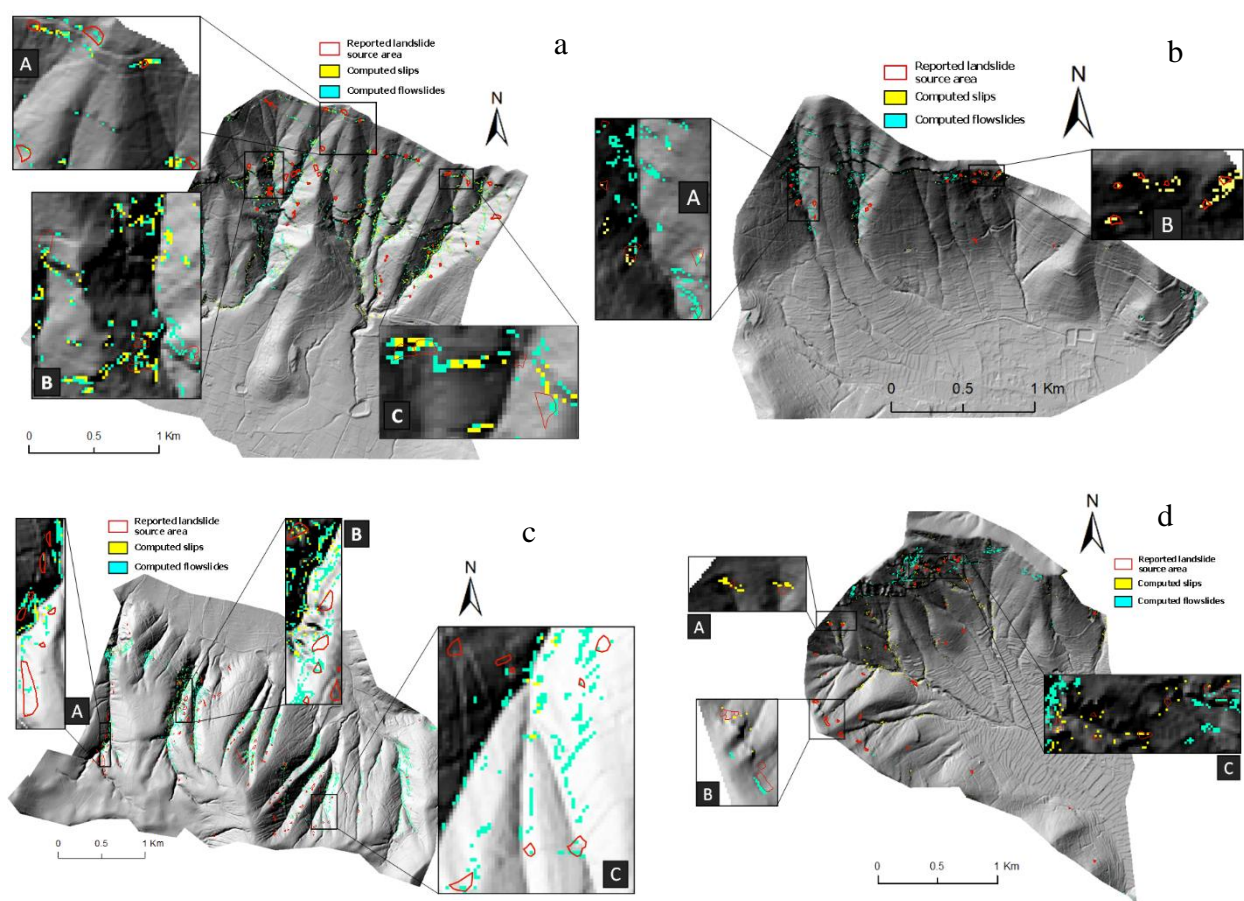


**Figure A.12 Predicted failure triggering mechanisms at different sites. a) Lavorate, b) Siano, c) Quindici, d) Bracigliano.**

Fig. A12 displays the spatial performance of the model for each site. Specifically, in Lavorate (Fig. A12a), although few landslides in the northern sector are not captured, instability events were

correctly identified at almost all other locations, especially in the areas labeled as A, B and C, where fourteen landslide contours show satisfactory overlap with the computed failure zones.

The results for the Siano site (Fig. A12b) also indicate an acceptable detection of source areas, while guaranteeing relatively low levels of overprediction. Specifically, in the areas labeled as A and B most failures are successfully captured.

Finally, as previously anticipated, the quality of the model performance cannot be regarded equally satisfactory for the sites Quindici and Bracigliano. With reference to Quindici, the source of this mismatch is highlighted in correspondence of the areas labeled as A, B and C (Fig. A12c), where the predictions simply surround the reported source areas instead of overlapping with them. Similar comments can be made for the Bracigliano site (Fig. A12d), where only few flowslides in the northern sector and scattered slips across the eastern part of the landscape have been predicted. Insets centered around the zones labeled as A, B and C correspondingly indicate that the reported failures are only partially captured.

#### *A.6 Discussion*

Despite the acceptable metrics obtained for all the five sites, such detailed analysis of the predicted spatial patterns of failure indicates remarkable variability of the model performance, thus requiring further discussion. Specifically, it is necessary to explain the factors responsible for the relatively poor performance of the model at the sites of Quindici and Bracigliano, as well as identify possible future model refinements that could mitigate the current shortcomings.

Among the two abovementioned sites, the municipality of Bracigliano was modeled with a rather uniform soil profile based exclusively on Ash A (Fig. A2). Hence, the model lacked the highly permeable pumice layer characterizing the stratigraphic profile used for all the other sites. On one

hand, this placed even further weight on the use of material properties calibrated for another site (i.e., Sarno), in that the use of a single layer would require a direct site-specific recalibration of the parameters associated with infiltration and failure. On the other hand, the assumption of perfect homogeneity may have led to relatively weaker pore pressure accumulation, which in other models was promoted by permeability contrasts and facilitated failure (see discussion in Lizarraga and Buscarnera, 2018). It is therefore possible that the complete removal of the pumice layer represents an oversimplification of the subsurface heterogeneity of the Bracigliano site, which, although less heterogeneous than others, may still have been impacted by the presence of pumices.

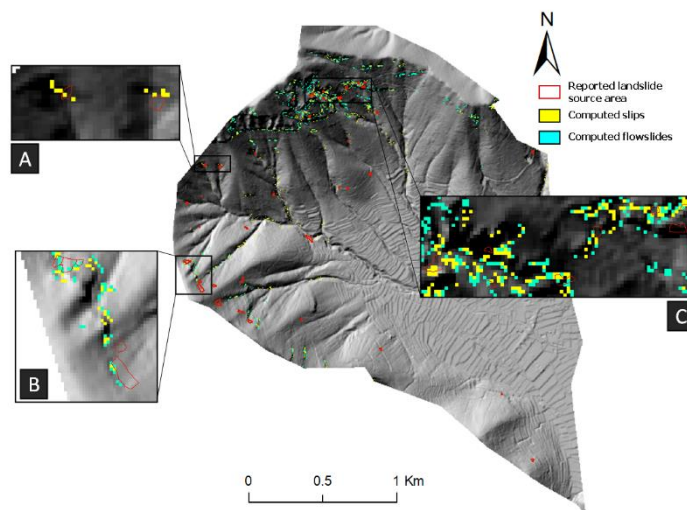


**Figure A.13 Bracigliano failure distribution calculated by Siano stratification profile.**

To test the latter argument, a further analysis was conducted with a layering based on the Siano stratigraphic profile (featuring a single pumice layer of 20 cm thickness). Such simulation leads to an improved spatial performance ( $SI = 10\%$  and  $SI/EI = 12$ ), as well as to a better match between computed and reported source areas (see highlighted areas A, B and C, in Fig. A13).

As for the municipality of Quindici, the model performance is heavily restricted by the relatively steep landscape morphology, across which few instability events were reported. Fig. A14a shows the slope angle of total source area of a near-Gaussian distribution with mean value around  $45^\circ$ .

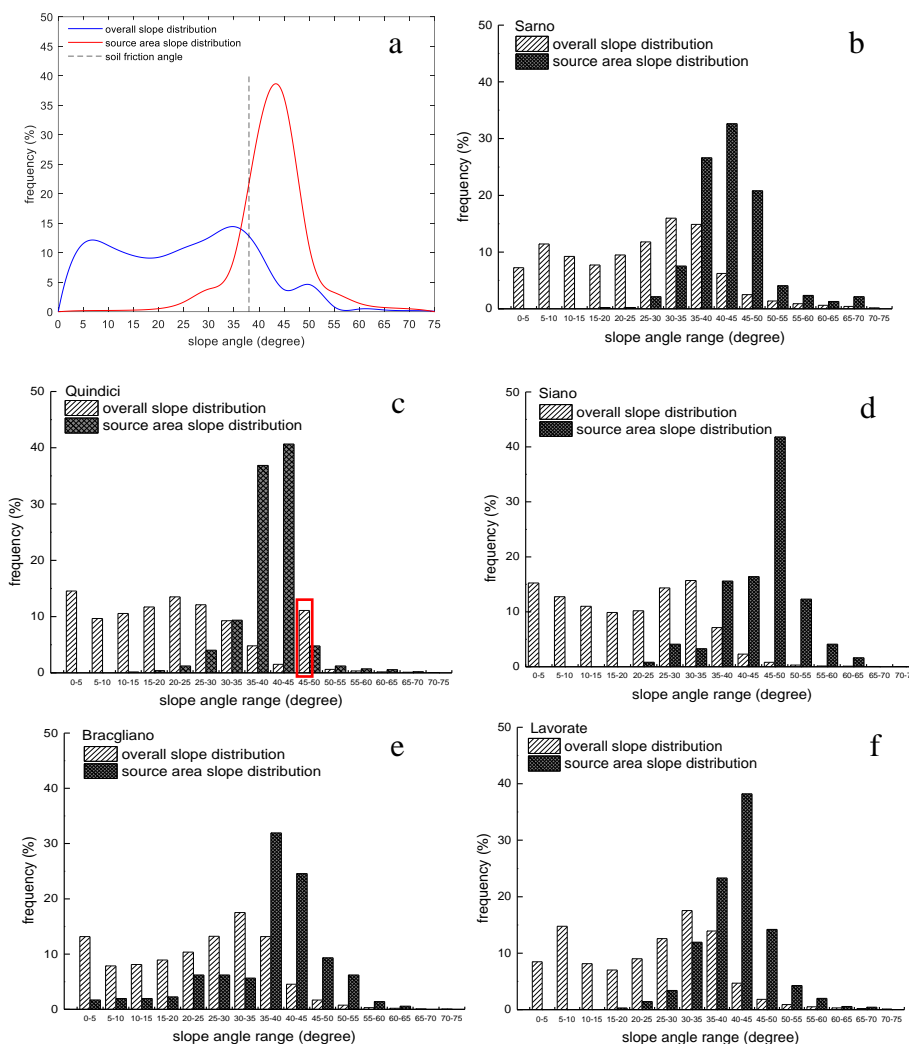


**Figure A.14** Source area and landscape slope angle distribution for each site. a) five studied municipalities, b) Sarno, c) Quindici, d) Siano, e) Braccigliano, f) Lavorate.

In Quindici, more than ten percent of the landscape is steeper than  $45^\circ$  (red polygon in Fig. A14c). However, most landslides took place at angles between  $35^\circ$  and  $45^\circ$ . This constitutes a challenge for spatially distributed triggering analyses. In fact, to capture a large percentage of source areas at this site, the model parameters should have triggering thresholds encompassing a sufficient set

of hillslopes with inclination angles lower than  $45^\circ$ . If such were the case, however, the features of the Quindici landscape mentioned above will inevitably lead to major overprediction.

To provide further context, Fig. A14 compares the distribution of slope angles of all the inspected municipalities. Except Quindici, at all sites the landslide source areas display higher frequencies at steep angles compared with the distribution of inclinations for the rest of the landscape. This feature facilitates the optimization of a spatially distributed model based on topographic data, in that a triggering threshold distinguishing stable and unstable slopes is not likely to lead to major overprediction. This is not the case for Quindici, whose landscape morphology involves a large portion of steep slopes not reflected in the distribution of landslide source areas. This suggests that steep slopes at Quindici benefit from local effects (e.g., vegetation reinforcement, existence of stable outcrops) preserving their stability during the rainstorm. Hence, it is arguable that any improvement of the model performance at that particular site requires the incorporation of effects currently not included in the model, such as the role of vegetation, a more accurate mapping of rock outcrops, water discharge from the bedrock, and usage of local distributed rainfall data currently not differentiated from very steep soil slopes.

### *A.7 Summary*

This appendix presented a regional-scale model to predict multi-model shallow landslide initiation in stratified deposits. Emphasis was given to the distinction between two potential modes of failure, namely frictional slips of limited mobility and liquefaction-induced flowslides leading to runaway failure. The framework is built around a vectorized Finite Element platform able to predict pore

pressure transients in heterogeneous unsaturated soils slopes, while guaranteeing computational efficiency and versatile definition of material properties and initial/boundary conditions.

The model was tested against a series of shallow landslide events induced by heavy rainstorms for which extensive laboratory and field data were available. Comparisons between equivalent models with and without stratigraphic heterogeneity were shown, demonstrating that the incorporation of soil layering leads to an improvement of all the tested metrics of performance, ranging from the predicted proportion of different initiation mechanisms, the spatiotemporal accuracy of the results, and the computed depth of failure.

The model was then tested with reference to four additional municipalities located across the same geological setting, but characterized by widely different stratigraphic profiles. Although the performance of the model varied significantly from one site to another, in all cases the performance was at least comparable to that reported by similar regional-scale models available in the literature, while in other cases it led to a one-order of magnitude increase of the model success. As a result, the modeling platform proposed here can be regarded as a robust tool for landslide susceptibility zonation whenever information about site-specific stratigraphic heterogeneity is available.

## References

- Agliardi, F., Scuderi, M. M., Fusi, N., & Collettini, C. (2020). Slow-to-fast transition of giant creeping rockslides modulated by undrained loading in basal shear zones. *Nature communications*, *11*(1), 1-11.
- Allmendinger, R. W. (1998). Inverse and forward numerical modeling of trishear fault-propagation folds. *Tectonics*, *17*(4), 640-656.
- Alonso, E., Zervos, A., & Pinyol, N. (2016). Thermo-poro-mechanical analysis of landslides: from creeping behaviour to catastrophic failure. *Géotechnique*, *66*(3), 202-219.
- Anderson, D. (1980). *An earthquake induced heat mechanism to explain the loss of strength of large rock and earth slides*. Paper presented at the Engineering for Protection from Natural Disasters, Proceedings of the International Conference, Bangkok, January 7-9.
- Angeli, M.-G., Gasparetto, P., Menotti, R. M., Pasuto, A., & Silvano, S. (1996). A visco-plastic model for slope analysis applied to a mudslide in Cortina d'Ampezzo, Italy. *Quarterly Journal of Engineering Geology and Hydrogeology*, *29*(3), 233-240.
- Aryal, A., Brooks, B. A., Reid, M. E., Bawden, G. W., & Pawlak, G. R. (2012). Displacement fields from point cloud data: Application of particle imaging velocimetry to landslide geodesy. *Journal of Geophysical Research: Earth Surface*, *117*(F1).
- Augustesen, A., Liingaard, M., & Lade, P. V. (2004). Evaluation of time-dependent behavior of soils. *International Journal of Geomechanics*, *4*(3), 137-156.
- Ayalew, L., & Yamagishi, H. J. G. (2005). The application of GIS-based logistic regression for landslide susceptibility mapping in the Kakuda-Yahiko Mountains, Central Japan. *65*(1-2), 15-31.
- Bailey, E. H., Irwin, W. P., & Jones, D. L. (1964). *Franciscan and related rocks, and their significance in the geology of western California*. Retrieved from
- Bandara, S., & Soga, K. (2015). Coupling of soil deformation and pore fluid flow using material point method. *Computers and Geotechnics*, *63*, 199-214.
- Baum, R. L., Coe, J. A., Godt, J. W., Harp, E. L., Reid, M. E., Savage, W. Z., . . . McKenna, J. P. J. L. (2005). Regional landslide-hazard assessment for Seattle, Washington, USA. *2*(4), 266-279.
- Baum, R. L., & Reid, M. E. (1995). Geology, hydrology, and mechanics of a slow-moving. *Clay Shale Slope Instab*, *10*, 79.
- Bellugi, D., Milledge, D. G., Dietrich, W. E., McKean, J. A., Perron, J. T., Sudderth, E. B., & Kazian, B. J. J. o. G. R. E. S. (2015). A spectral clustering search algorithm for predicting shallow landslide size and location. *120*(2), 300-324.
- Bennett, G. L., Roering, J. J., Mackey, B. H., Handwerger, A. L., Schmidt, D. A., & Guillod, B. P. (2016). Historic drought puts the brakes on earthflows in Northern California. *Geophysical Research Letters*, *43*(11), 5725-5731.
- Berti, M., & Simoni, A. (2010). Field evidence of pore pressure diffusion in clayey soils prone to landsliding. *Journal of Geophysical Research: Earth Surface*, *115*(F3).
- Bingham, E. C. (1917). *An investigation of the laws of plastic flow*: US Government Printing Office.
- Bucknam, R. C., Coe, J. A., Chavarría, M. M., Godt, J. W., Tarr, A. C., Bradley, L.-A., . . . Johnson, M. L. (2001). Landslides triggered by Hurricane Mitch in Guatemala—Inventory and discussion. *US Geological Survey Open File Report*, *1*.
- Buscarnera, G., & Di Prisco, C. (2013). Soil stability and flow slides in unsaturated shallow slopes: Can saturation events trigger liquefaction processes? *Géotechnique*, *63*(10), 801-817.
- Buscarnera, G., & Di Prisco, C. J. G. (2013). Soil stability and flow slides in unsaturated shallow slopes: can saturation events trigger liquefaction processes. *63*(10), 801-817.
- Buscarnera, G., & Di Prisco, C. J. G. L. (2011). Stability criteria for unsaturated shallow slopes. *1*(4), 85-90.

- Buscarnera, G., & Whittle, A. J. (2012). Constitutive modelling approach for evaluating the triggering of flow slides. *Canadian Geotechnical Journal*, 49(5), 499-511.
- Buscarnera, G., & Whittle, A. J. (2013). Model prediction of static liquefaction: influence of the initial state on potential instabilities. *Journal of Geotechnical and Geoenvironmental Engineering*, 139(3), 420-432.
- Cardinali, M., Ardizzone, F., Galli, M., Guzzetti, F., & Reichenbach, P. (2000). *Landslides triggered by rapid snow melting: the December 1996–January 1997 event in Central Italy*. Paper presented at the Proceedings 1st Plinius conference on Mediterranean storms.
- Carlioni, G., & Mazzanti, R. (1964). Rilevamento geologico della frana del Vaiont. *Giornale di Geologia*, 32, 105-138.
- Casagrande, A. (1936). Characteristics of cohesionless soils affecting the stability of slopes and earth fills. *J. Boston Society of Civil Engineers*, 23(1), 13-32.
- Cascini, L., Calvello, M., & Grimaldi, G. M. (2010). Groundwater modeling for the analysis of active slow-moving landslides. *Journal of Geotechnical and Geoenvironmental Engineering*, 136(9), 1220-1230.
- Cascini, L., Calvello, M., & Grimaldi, G. M. (2014). Displacement trends of slow-moving landslides: Classification and forecasting. *Journal of mountain science*, 11(3), 592-606.
- Cascini, L., Cuomo, S., & Della Sala, M. J. G. (2011). Spatial and temporal occurrence of rainfall-induced shallow landslides of flow type: A case of Sarno-Quindici, Italy. *126(1-2)*, 148-158.
- Cascini, L., Cuomo, S., & Guida, D. J. E. G. (2008). Typical source areas of May 1998 flow-like mass movements in the Campania region, Southern Italy. *96(3-4)*, 107-125.
- Celia, M. A., Bouloutas, E. T., & Zarba, R. L. J. W. r. r. (1990). A general mass-conservative numerical solution for the unsaturated flow equation. *26(7)*, 1483-1496.
- Chen, Y., & Buscarnera, G. (2021). Numerical simulation of unstable suction transients in unsaturated soils: the role of wetting collapse. *International Journal for Numerical and Analytical Methods in Geomechanics*, 45(11), 1569-1587.
- Chen, Y., & Buscarnera, G. (2021). Numerical simulation of unstable suction transients in unsaturated soils: the role of wetting collapse. *International Journal for Numerical and Analytical Methods in Geomechanics*, 45(11), 1569-1587.
- Chen, Z., Huan, G., & Ma, Y. (2006). *Computational methods for multiphase flows in porous media* (Vol. 2): Siam.
- Ciabatti, M. (1964). *La dinamica della frana del Vajont*: Museo geologico Giovanni Capellini.
- Cohen-Waeber, J., Bürgmann, R., Chaussard, E., Giannico, C., & Ferretti, A. (2018). Spatiotemporal patterns of precipitation-modulated landslide deformation from independent component analysis of InSAR time series. *Geophysical Research Letters*, 45(4), 1878-1887.
- Conte, E., Donato, A., & Troncone, A. (2014). A finite element approach for the analysis of active slow-moving landslides. *Landslides*, 11(4), 723-731.
- Corominas, J., Moya, J., Ledesma, A., Lloret, A., & Gili, J. A. (2005). Prediction of ground displacements and velocities from groundwater level changes at the Vallcebre landslide (Eastern Pyrenees, Spain). *Landslides*, 2(2), 83-96.
- Corominas, J., Moya, J., Lloret, A., Gili, J., Angeli, M., Pasuto, A., & Silvano, S. (2000). Measurement of landslide displacements using a wire extensometer. *Engineering geology*, 55(3), 149-166.
- Crosta, G., Dal Negro, P. J. N. H., & Science, E. S. (2003). Observations and modelling of soil slip-debris flow initiation processes in pyroclastic deposits: the Sarno 1998 event. *3(1/2)*, 53-69.
- Crosta, G., Frattini, P. J. N. H., & Science, E. S. (2003). Distributed modelling of shallow landslides triggered by intense rainfall. *3(1/2)*, 81-93.
- Cuomo, S., & Iervolino, A. J. J. o. M. S. (2016). Investigating the role of stratigraphy in large-area physically-based analysis of December 1999 Cervinara shallow landslides. *13(1)*, 104-115.
- Dai, F., Lee, C., & Ngai, Y. Y. (2002). Landslide risk assessment and management: an overview. *Engineering geology*, 64(1), 65-87.

- Damiano, E., Olivares, L., & Picarelli, L. J. E. G. (2012). Steep-slope monitoring in unsaturated pyroclastic soils. *137*, 1-12.
- Davis, R. O., & Selvadurai, A. P. (2005). *Plasticity and geomechanics*: Cambridge university press.
- Di Crescenzo, G., & Santo, A. J. G. (2005). Debris slides—rapid earth flows in the carbonate massifs of the Campania region (Southern Italy): morphological and morphometric data for evaluating triggering susceptibility. *66*(1-4), 255-276.
- Di Prisco, C., & Flessati, L. (2021). Progressive failure in elastic–viscoplastic media: from theory to practice. *Géotechnique*, *71*(2), 153-169.
- di Prisco, C., & Imposimato, S. (1996). Time dependent mechanical behaviour of loose sands. *Mechanics of Cohesive-frictional Materials: An International Journal on Experiments, Modelling and Computation of Materials and Structures*, *1*(1), 45-73.
- Duncan, J. M. (1996). State of the art: limit equilibrium and finite-element analysis of slopes. *Journal of Geotechnical engineering*, *122*(7), 577-596.
- Duncan, J. M., Wright, S. G., & Brandon, T. L. (2014). *Soil strength and slope stability*: John Wiley & Sons.
- Eberhardt, E., Stead, D., & Coggan, J. (2004). Numerical analysis of initiation and progressive failure in natural rock slopes—the 1991 Randa rockslide. *International Journal of Rock Mechanics and Mining Sciences*, *41*(1), 69-87.
- Ferrari, A., Ledesma, A., González, D., & Corominas, J. (2011). Effects of the foot evolution on the behaviour of slow-moving landslides. *Engineering geology*, *117*(3-4), 217-228.
- Finnegan, N., Perkins, J., Nereson, A., & Handwerger, A. (2021). Unsaturated Flow Processes and the Onset of Seasonal Deformation in Slow-Moving Landslides. *Journal of Geophysical Research: Earth Surface*, *126*(5), e2020JF005758.
- fr/MIDL/, G. M. g. p. u.-m. f. h. w. l. u.-m. (2004). On dense granular flows. *The European Physical Journal E*, *14*, 341-365.
- Frattini, P., Crosta, G. B., Fusi, N., & Dal Negro, P. J. E. G. (2004). Shallow landslides in pyroclastic soils: a distributed modelling approach for hazard assessment. *73*(3-4), 277-295.
- Froude, M. J., & Petley, D. N. (2018). Global fatal landslide occurrence from 2004 to 2016. *Natural Hazards and Earth System Sciences*, *18*(8), 2161-2181.
- Gardner, W. J. S. s. (1958). Some steady-state solutions of the unsaturated moisture flow equation with application to evaporation from a water table. *85*(4), 228-232.
- Guadagno, F., Forte, R., Revellino, P., Fiorillo, F., & Focareta, M. J. G. (2005). Some aspects of the initiation of debris avalanches in the Campania Region: the role of morphological slope discontinuities and the development of failure. *66*(1-4), 237-254.
- Hahm, W. J., Rempe, D. M., Dralle, D. N., Dawson, T. E., Lovill, S. M., Bryk, A. B., . . . Dietrich, W. E. (2019). Lithologically controlled subsurface critical zone thickness and water storage capacity determine regional plant community composition. *Water Resources Research*, *55*(4), 3028-3055.
- Handwerger, A. L., Huang, M.-H., Fielding, E. J., Booth, A. M., & Bürgmann, R. (2019). A shift from drought to extreme rainfall drives a stable landslide to catastrophic failure. *Scientific reports*, *9*(1), 1-12.
- Handwerger, A. L., Roering, J. J., & Schmidt, D. A. (2013). Controls on the seasonal deformation of slow-moving landslides. *Earth and Planetary Science Letters*, *377*, 239-247.
- Handwerger, A. L., Roering, J. J., Schmidt, D. A., & Rempel, A. W. (2015). Kinematics of earthflows in the Northern California Coast Ranges using satellite interferometry. *Geomorphology*, *246*, 321-333.
- Hapke, C. J., & Green, K. R. (2006). Coastal landslide material loss rates associated with severe climatic events. *Geology*, *34*(12), 1077-1080.
- Haque, U., Blum, P., Da Silva, P. F., Andersen, P., Pilz, J., Chalov, S. R., . . . Poyiadji, E. (2016). Fatal landslides in Europe. *Landslides*, *13*(6), 1545-1554.

- Hendron Jr, A., & Patton, F. D. (1985). *The vaiont slide. A geotechnical analysis based on new geologic observations of the failure surface. Volume 1. Main text*. Retrieved from
- Hilley, G. E., Bürgmann, R., Ferretti, A., Novali, F., & Rocca, F. (2004). Dynamics of slow-moving landslides from permanent scatterer analysis. *Science*, 304(5679), 1952-1955.
- Hu, X., & Bürgmann, R. (2020). Rheology of a Debris Slide from the Joint Analysis of UAVSAR and LiDAR Data. *Geophysical Research Letters*, 47(8), e2020GL087452.
- Hungr, O. (2007). Dynamics of rapid landslides. In *Progress in landslide science* (pp. 47-57): Springer.
- Hungr, O., Leroueil, S., & Picarelli, L. J. L. (2014). The Varnes classification of landslide types, an update. *11*(2), 167-194.
- Hürlimann, M., Garcia-Piera, J., & Ledesma, A. (2000). Causes and mobility of large volcanic landslides: application to Tenerife, Canary Islands. *Journal of Volcanology and Geothermal Research*, 103(1-4), 121-134.
- Hutchinson, J. (1986). A sliding-consolidation model for flow slides. *Canadian Geotechnical Journal*, 23(2), 115-126.
- Iverson, R. M. (1985). Unsteady, nonuniform landslide motion: Theory and measurement.
- Iverson, R. M. (2000). Landslide triggering by rain infiltration. *Water Resources Research*, 36(7), 1897-1910.
- Iverson, R. M. (2005). Regulation of landslide motion by dilatancy and pore pressure feedback. *Journal of Geophysical Research: Earth Surface*, 110(F2).
- Iverson, R. M. (2020). Landslide disparities, flume discoveries, and Oso despair. *Perspectives of Earth and Space Scientists*, 1(1), e2019CN000117.
- Iverson, R. M., & Major, J. J. (1987). Rainfall, ground-water flow, and seasonal movement at Minor Creek landslide, northwestern California: Physical interpretation of empirical relations. *Geological Society of America Bulletin*, 99(4), 579-594.
- Jennings, C. (1977a). *GEOLOGIC MAP OF CALIFORNIA 1: 750 000*.
- Jennings, C. (1977b). Geologic map of California: Menlo Park, CA. *US Geological Survey*.
- Keefer, D. K., & Johnson, A. M. (1983). *Earth flows; morphology, mobilization, and movement* (2330-7102). Retrieved from
- Kelsey, H., Coghlan, M., Pitlick, J., & Best, D. (1996). *Geomorphic analysis of streamside landslides in the Redwood Creek basin, northwestern California*. Paper presented at the International Journal of Rock Mechanics and Mining Sciences and Geomechanics Abstracts.
- Lacroix, P., Handwerger, A. L., & Bièvre, G. (2020). Life and death of slow-moving landslides. *Nature Reviews Earth & Environment*, 1-16.
- Lade, P. V. (1993). Initiation of static instability in the submarine Nerlerk berm. *Canadian Geotechnical Journal*, 30(6), 895-904.
- Lade, P. V., Yamamuro, J. A., & Bopp, P. A. (1997). Influence of time effects on instability of granular materials. *Computers and Geotechnics*, 20(3-4), 179-193.
- Leroueil, S. (2001). Natural slopes and cuts: movement and failure mechanisms. *Géotechnique*, 51(3), 197-243.
- Li, H.-b., Xu, Y.-r., Zhou, J.-w., Wang, X.-k., Yamagishi, H., & Dou, J. (2020). Preliminary analyses of a catastrophic landslide occurred on July 23, 2019, in Guizhou Province, China. In: Springer.
- Li, X., Lizárraga, J. J., & Buscarnera, G. (2021). Regional-scale simulation of flowslide triggering in stratified deposits. *Engineering geology*, 292, 106248.
- Li, X., Song, Z., Lizárraga, J. J., & Buscarnera, G. (2019). *Regional-scale modelling of liquefaction-induced shallow landslides in unsaturated slopes*. Paper presented at the 7th International Conference on Debris-Flow Hazards Mitigation: Mechanics, Monitoring, Modeling, and Assessment.
- Liingaard, M., Augustesen, A., & Lade, P. V. (2004). Characterization of models for time-dependent behavior of soils. *International Journal of Geomechanics*, 4(3), 157-177.

- Lizárraga, J., Buscarnera, G., Frattini, P., & Crosta, G. (2017). Spatially distributed modeling of landslide triggering: An approach based on principles of unsaturated soil plasticity. In *Landslides and Engineered Slopes. Experience, Theory and Practice* (pp. 1287-1294): CRC Press.
- Lizárraga, J., & Buscarnera, G. J. G. (2017). Safety factors to detect flowslides and slips in unsaturated shallow slopes. *68*(5), 442-450.
- Lizárraga, J. J., & Buscarnera, G. (2019). Spatially distributed modeling of rainfall-induced landslides in shallow layered slopes. *Landslides*, *16*(2), 253-263.
- Lizárraga, J. J., & Buscarnera, G. J. L. (2018). Spatially distributed modeling of rainfall-induced landslides in shallow layered slopes. *16*(2), 253-263.
- Lu, N., Wayllace, A., & Oh, S. (2013). Infiltration-induced seasonally reactivated instability of a highway embankment near the Eisenhower Tunnel, Colorado, USA. *Engineering geology*, *162*, 22-32.
- Mackey, B., Roering, J., & McKean, J. (2009). Long-term kinematics and sediment flux of an active earthflow, Eel River, California. *Geology*, *37*(9), 803-806.
- Mackey, B. H., & Roering, J. J. (2011). Sediment yield, spatial characteristics, and the long-term evolution of active earthflows determined from airborne LiDAR and historical aerial photographs, Eel River, California. *Bulletin*, *123*(7-8), 1560-1576.
- Malet, J.-P., Maquaire, O., Locat, J., & Remaître, A. (2004). Assessing debris flow hazards associated with slow moving landslides: methodology and numerical analyses. *Landslides*, *1*(1), 83-90.
- Mantovani, F., Pasuto, A., Silvano, S., & Zannoni, A. (2000). Collecting data to define future hazard scenarios of the Tessina landslide. *International Journal of Applied Earth Observation and Geoinformation*, *2*(1), 33-40.
- Marinelli, F., Pisanò, F., Di Prisco, C., & Buscarnera, G. (2018). Model-based interpretation of undrained creep instability in loose sands. *Géotechnique*, *68*(6), 504-517.
- McKenna, J. P., Santi, P. M., Amblard, X., & Negri, J. J. L. (2012). Effects of soil-engineering properties on the failure mode of shallow landslides. *9*(2), 215-228.
- Mihalache, C., & Buscarnera, G. (2016). Diffusive instability of pore pressure transients in deformable unsaturated soils. *Journal of Engineering Mechanics*, *142*(11), 04016091.
- Mitchell, J. K., Campanella, R. G., & Singh, A. (1968). Soil creep as a rate process. *Journal of the Soil Mechanics and Foundations Division*, *94*(1), 231-253.
- Montgomery, D. R., & Dietrich, W. E. J. W. r. r. (1994). A physically based model for the topographic control on shallow landsliding. *30*(4), 1153-1171.
- Nappo, N., Peduto, D., Mavrouli, O., van Westen, C. J., & Gullà, G. (2019). Slow-moving landslides interacting with the road network: Analysis of damage using ancillary data, in situ surveys and multi-source monitoring data. *Engineering geology*, *260*, 105244.
- Nereson, A., Davila Olivera, S., & Finnegan, N. (2018). Field and Remote-Sensing Evidence for Hydro-mechanical Isolation of a Long-Lived Earthflow in Central California. *Geophysical Research Letters*, *45*(18), 9672-9680.
- Oberender, P. W., & Puzrin, A. M. (2016). Observation-guided constitutive modelling for creeping landslides. *Géotechnique*, *66*(3), 232-247.
- Pack, R. T., Tarboton, D. G., & Goodwin, C. N. (1998). *The SINMAP approach to terrain stability mapping*. Paper presented at the 8th congress of the international association of engineering geology, Vancouver, British Columbia, Canada.
- Papa, R. (2007). *Indagine sperimentale di una copertura piroclastica di un versante della Campania*. PhD thesis, University of Naples "Federico II,
- Pastor, M., Martin Stickle, M., Dutto, P., Mira, P., Fernández Merodo, J., Blanc, T., . . . Benítez, A. (2015). A viscoplastic approach to the behaviour of fluidized geomaterials with application to fast landslides. *Continuum Mechanics and Thermodynamics*, *27*(1), 21-47.
- Perzyna, P. (1963). The constitutive equations for rate sensitive plastic materials. *Quarterly of applied mathematics*, *20*(4), 321-332.

- Perzyna, P. (1966). Fundamental problems in viscoplasticity. In *Advances in applied mechanics* (Vol. 9, pp. 243-377): Elsevier.
- Petley, D. (2012). Global patterns of loss of life from landslides. *Geology*, 40(10), 927-930.
- Petley, D., Mantovani, F., Bulmer, M., & Zannoni, A. (2005). The use of surface monitoring data for the interpretation of landslide movement patterns. *Geomorphology*, 66(1-4), 133-147.
- Petley, D. N., Bulmer, M. H., & Murphy, W. (2002). Patterns of movement in rotational and translational landslides. *Geology*, 30(8), 719-722.
- Picarelli, L., Olivares, L., & Avolio, B. J. E. G. (2008). Zoning for flowslide and debris flow in pyroclastic soils of Campania Region based on “infinite slope” analysis. *102*(3-4), 132-141.
- Pirone, M., Papa, R., Nicotera, M. V., & Urciuoli, G. J. L. (2015). In situ monitoring of the groundwater field in an unsaturated pyroclastic slope for slope stability evaluation. *12*(2), 259-276.
- Pisanò, F., & Prisco, C. d. (2016). A stability criterion for elasto-viscoplastic constitutive relationships. *International Journal for Numerical and Analytical Methods in Geomechanics*, 40(1), 141-156.
- Puzrin, A. (2012). *Constitutive modelling in geomechanics: introduction*: Springer Science & Business Media.
- Puzrin, A. M., & Schmid, A. (2011). Progressive failure of a constrained creeping landslide. *Proceedings of the Royal Society A: Mathematical, Physical and Engineering Sciences*, 467(2133), 2444-2461.
- Puzrin, A. M., & Sterba, I. (2006). Inverse long-term stability analysis of a constrained landslide. *Géotechnique*, 56(7), 483-489.
- Richard, L. J. p. (1931). Capillary conduction of liquids through porous mediums. *1*(5), 318-333.
- Rodriguez, C., Bommer, J., & Chandler, R. (1999). Earthquake-induced landslides: 1980–1997. *Soil Dynamics and Earthquake Engineering*, 18(5), 325-346.
- Roering, J. J., Mackey, B. H., Handwerger, A. L., Booth, A. M., Schmidt, D. A., Bennett, G. L., & Cerovski-Darriau, C. (2015). Beyond the angle of repose: A review and synthesis of landslide processes in response to rapid uplift, Eel River, Northern California. *Geomorphology*, 236, 109-131.
- Roscoe, K. H., Schofield, A., & Wroth, a. P. (1958). On the yielding of soils. *Géotechnique*, 8(1), 22-53.
- Rowe, P. W. (1962). The stress-dilatancy relation for static equilibrium of an assembly of particles in contact. *Proceedings of the Royal Society of London. Series A. Mathematical and Physical Sciences*, 269(1339), 500-527.
- Runqiu, H. (2009). Some catastrophic landslides since the twentieth century in the southwest of China. *Landslides*, 6(1), 69-81.
- Scheingross, J. S., Minchew, B. M., Mackey, B. H., Simons, M., Lamb, M. P., & Hensley, S. (2013). Fault-zone controls on the spatial distribution of slow-moving landslides. *Bulletin*, 125(3-4), 473-489.
- Schulz, W. H., Smith, J. B., Wang, G., Jiang, Y., & Roering, J. J. (2018). Clayey landslide initiation and acceleration strongly modulated by soil swelling. *Geophysical Research Letters*, 45(4), 1888-1896.
- Schuster, R. L., Salcedo, D. A., & Valenzuela, L. (2002). Overview of catastrophic landslides of South America in the twentieth century. *Reviews in Engineering Geology*, 15, 1-34.
- Selli, R., & Trevisan, L. (1964). Caratteri e Interpretazione della Frana del Valont *Annali Mus Geolog Bologna*, 32. In: Fas.
- Sheng, D., Sloan, S. W., Gens, A., & Smith, D. W. (2003). Finite element formulation and algorithms for unsaturated soils. Part I: Theory. *International Journal for Numerical and Analytical Methods in Geomechanics*, 27(9), 745-765.
- Shi, Z., Hambleton, J. P., & Buscarnera, G. (2019). Bounding surface elasto-viscoplasticity: A general constitutive framework for rate-dependent geomaterials. *Journal of Engineering Mechanics*, 145(3), 04019002.

- Siman-Tov, S., & Brodsky, E. E. (2021). Distinguishing between rheophysical regimes of fluid-saturated granular-flows using dilatancy and acoustic emission measurements. *Granular Matter*, 23(2), 1-11.
- Sloan, S. W., & Abbo, A. J. (1999). Biot consolidation analysis with automatic time stepping and error control Part 1: theory and implementation. *International Journal for Numerical and Analytical Methods in Geomechanics*, 23(6), 467-492.
- Soga, K., Alonso, E., Yerro, A., Kumar, K., & Bandara, S. (2016). Trends in large-deformation analysis of landslide mass movements with particular emphasis on the material point method. *Géotechnique*, 66(3), 248-273.
- Song, Z., Li, X., Lizárraga, J. J., Zhao, L., & Buscarnera, G. (2020). Spatially distributed landslide triggering analyses accounting for coupled infiltration and volume change. *Landslides*, 17(12), 2811-2824.
- Sorbino, G. (2005). *Numerical modelling of soil suction measurements in pyroclastic soils*. Paper presented at the Int. Symp. "Advanced experimental unsaturated soil mechanics". Taylor and Francis Group, London.
- Sorbino, G., Sica, C., & Cascini, L. J. N. h. (2010). Susceptibility analysis of shallow landslides source areas using physically based models. 53(2), 313-332.
- Stark, T. D., Baghdady, A. K., Hungr, O., & Aaron, J. (2017). Case study: Oso, Washington, landslide of March 22, 2014—Material properties and failure mechanism. *Journal of Geotechnical and Geoenvironmental Engineering*, 143(5), 05017001.
- Tan, Q.-M. (2011). *Dimensional analysis: with case studies in mechanics*: Springer Science & Business Media.
- Taylor, W. L., & Pollard, D. D. (2000). Estimation of in situ permeability of deformation bands in porous sandstone, Valley of Fire, Nevada. *Water Resources Research*, 36(9), 2595-2606.
- Terzaghi, K. (1925). Principles of soil mechanics. *Engineering News-Record*, 95(19-27), 19-32.
- Tika, T. E., Vaughan, P., & Lemos, L. (1996). Fast shearing of pre-existing shear zones in soil. *Géotechnique*, 46(2), 197-233.
- Tschuchnigg, F., Schweiger, H., Sloan, S. W., Lyamin, A. V., & Raissakis, I. (2015). Comparison of finite-element limit analysis and strength reduction techniques. *Géotechnique*, 65(4), 249-257.
- Van Asch, T. W., Van Beek, L., & Bogaard, T. (2007). Problems in predicting the mobility of slow-moving landslides. *Engineering geology*, 91(1), 46-55.
- Van Dam, J., & Feddes, R. J. J. o. H. (2000). Numerical simulation of infiltration, evaporation and shallow groundwater levels with the Richards equation. 233(1-4), 72-85.
- Van Genuchten, M. T. J. S. s. s. o. A. j. (1980). A closed-form equation for predicting the hydraulic conductivity of unsaturated soils 1. 44(5), 892-898.
- Van Westen, C., Van Asch, T. W., Soeters, R. J. B. o. E. g., & Environment, t. (2006). Landslide hazard and risk zonation—why is it still so difficult? , 65(2), 167-184.
- Vardoulakis, I. (2002). Dynamic thermo-poro-mechanical analysis of catastrophic landslides. *Géotechnique*, 52(3), 157-171.
- Veveakis, E., Vardoulakis, I., & Di Toro, G. (2007). Thermoporomechanics of creeping landslides: The 1963 Vaiont slide, northern Italy. *Journal of Geophysical Research: Earth Surface*, 112(F3).
- Voight, B. (1978). *Rockslides and avalanches*: Elsevier Scientific Pub. Co.
- Voight, B., & Faust, C. (1982). Frictional heat and strength loss in some rapid landslides. *Géotechnique*, 32(1), 43-54.
- Warrick, J. A., Ritchie, A. C., Schmidt, K. M., Reid, M. E., & Logan, J. (2019). Characterizing the catastrophic 2017 Mud Creek landslide, California, using repeat structure-from-motion (SfM) photogrammetry. *Landslides*, 16(6), 1201-1219.
- Wartman, J., Montgomery, D. R., Anderson, S. A., Keaton, J. R., Benoît, J., dela Chapelle, J., & Gilbert, R. (2016). The 22 March 2014 Oso landslide, Washington, USA. *Geomorphology*, 253, 275-288.
- Wood, D. M. (1990). *Soil behaviour and critical state soil mechanics*: Cambridge university press.

- Wood, D. M. (2004). *Geotechnical Modelling (Applied geotechnics; v. 1)*: Taylor & Francis Group/Books.
- Wu, W., & Sidle, R. C. J. W. r. r. (1995). A distributed slope stability model for steep forested basins. *31*(8), 2097-2110.
- Yeh, G., & Ward, D. (1980). *FEMWATER: A finite-element model of water flow through saturated-unsaturated porous media*. Retrieved from
- Zambelli, C., Di Prisco, C., & Imposimato, S. (2004). A cyclic elasto-viscoplastic constitutive model: theoretical discussion and validation. *Cyclic Behaviour of Soils and Liquefaction Phenomena*, 99-106.
- Zienkiewicz, O. C., Chan, A., Pastor, M., Schrefler, B., & Shiomi, T. (1999). *Computational geomechanics*: Citeseer.